Forschungszentrum Karlsruhe
in der Helmholtz-Gemeinschaft

Wissenschaftliche Berichte
FZKA 7343

Electronic Transport and Noise in Quantum Dot Systems

J. Aghassi

Institut für Nanotechnologie

September 2007

Forschungszentrum Karlsruhe
in der Helmholtz-Gemeinschaft
Wissenschaftliche Berichte
FZKA 7343

Electronic Transport and Noise in Quantum Dot Systems

Jasmin Aghassi
Institut für Nanotechnologie

Von der Fakultät für Physik
der Universität Karlsruhe (TH) genehmigte Dissertation

Forschungszentrum Karlsruhe GmbH, Karlsruhe
2007

Forschungszentrum Karlsruhe GmbH
Postfach 3640, 76021 Karlsruhe

Mitglied der Hermann von Helmholtz-Gemeinschaft
Deutscher Forschungszentren (HGF)

ISSN 0947-8620

urn:nbn:de:0005-073431

Electronic Transport and Noise in Quantum Dot Systems

Elektronischer Transport und Stromrauschen in Quantenpunktsystemen

Zur Erlangung des akademischen Grades eines

DOKTORS DER NATURWISSENSCHAFTEN

von der Fakultät für Physik der

Universität Karlsruhe (TH)

genehmigte

DISSERTATION

von

Dipl.-Phys. Jasmin Aghassi

aus

Mainz

Tag der mündlichen Prüfung:	06. Juli 2007
Referent:	Prof. Dr. Gerd Schön
Korreferent:	Prof. Dr. Jürgen König

Abstract

In this thesis we describe the current and shot noise properties of quantum dot systems. Their transport characteristics reveal information about interesting quantum mechanical effects such as the energy quantization and electronic correlations due to Coulomb interactions of electrons. Based on a diagrammatic real time approach we developed a numerical method to describe the current and shot noise. The method includes all relevant quantities such as the electron spin, the Coulomb interaction as well as the delocalized nature of the electronic wavefunctions in coupled quantum dots. Our approach is based on a perturbative expansion in terms of the coupling constant to the leads and thus allows to describe sequential tunneling as well as co-tunneling transport in local as well as non-local multilevel systems. For a system of a double quantum dot we analyzed in detail the influence of asymmetries on the electronic transport properties and found strong correlations. In contrast, larger systems such as three and more coupled quantum dots display a strong noise enhancement even in fully symmetric situations due to their complex delocalized wavefunctions. Within the Coulomb blockade transport is governed by co-tunneling processes. In particular we investigated the regime of co-tunneling assisted sequential tunneling and described characteristic features in the differential conductance as well as the noise properties.

Deutsche Zusammenfassung

Die vorliegende Arbeit befasst sich mit der Beschreibung des elektronischen Stromes und des Schrotrauschens in Quantenpunkten. Deren charakteristische Transporteigenschaften geben Aufschluss über interessante quantenmechanische Effekte wie die Quantisierung der elektronischen Energieniveaus sowie Korrelationseffekte, die z.B. durch die Coulomb Wechselwirkung der Elektronen hervorgerufen werden. Basierend auf einer Realzeit-Störungstheorie wurde eine numerische Methode zur Berechnung des Stromes und des Schrotrauschens implementiert, die es erlaubt, relevante Grössen wie den Spin der Elektronen, ihre gegenseitige Coulomb Wechselwirkung sowie die delokalisierte elektronische Wellenfunktion in gekoppelten Quantenpunkten zu berücksichtigen. Unsere Methode beruht auf einer störungstheoretischen Entwicklung in Ordnungen der Kopplungskonstanten zu den elektronischen Zuleitungen. Sie erlaubt erstmals die vollständige Beschreibung eines elektronischen Systems mit mehreren lokalen sowie nicht lokalen Niveaus unter Berücksichtigung sowohl sequentieller Tunnelprozesse als auch Kotunnel-Prozesse. Es wurde detailliert der Einfluss von Asymmetrien auf das Strom- und Rauschverhalten in Doppelquantenpunkten untersucht und gezeigt, unter welchen Bedingungen starke Korrelationen im elektronischen Transport auftreten. Hingegen zeigen grössere Systeme, wie drei oder mehrere gekoppelte Quantenpunkte aufgrund ihrer komplexen elektronischen Wellenfunktion ein stark erhöhtes Rauschen auch in symmetrischen Konfigurationen. Innerhalb des Coulomb Blockade Regimes wurde insbesondere das Kotunneln-induzierte sequentielle Tunneln im Leitwert als auch im Rauschen in Abhängigkeit einer Gatespannung charakterisiert.

Deutsche Zusammenfassung

Die vorliegende Arbeit befasst sich mit der Beschreibung des elektronischen Stromes und des Schrotrauschens in nanoskaligen Systemen wie zum Beispiel Quantenpunkten. Die charakteristischen Transporteigenschaften der Quantenpunkte geben Aufschluss über interessante quantenmechanische Effekte wie die Quantisierung der elektronischen Energieniveaus sowie Korrelationseffekte, die durch elementare Wechselwirkungsprozesse (Coulomb Wechselwirkung) der Elektronen hervorgerufen werden.
Basierend auf einer Realzeit-Störungstheorie wurde eine numerische Methode zur Berechnung des Stromes und des Schrotrauschens implementiert, die es erlaubt, alle relevanten Grössen in Quantenpunktsystemen, also den Spin der Elektronen, ihre gegenseitige Coulomb Wechselwirkung sowie die delokalisierte elektronische Wellenfunktion in gekoppelten Quantenpunkten zu berücksichtigen. Die numerische Methode beruht auf einer störungstheoretischen Entwicklung in Ordnungen der Kopplungskonstanten Γ zu den elektronischen Zuleitungen der Quantenpunktsysteme. Sie erlaubt erstmals die vollständige Beschreibung eines komplizierten nanoskaligen, elektronischen Systems mit mehreren lokalen sowie nicht lokalen Niveaus unter Berücksichtigung sowohl sequentieller Tunnelprozesse in erster Ordnung in Γ als auch Kotunnelprozesse in zweiter Ordnung in Γ.
Als erstes System werden zwei kohärent gekoppelte Quantenpunkte betrachtet. Das diskrete Energiespektrum des Doppelquantenpunktes wird durch Diagonalisierung berechnet und es ergeben sich delokalisierte elektronische Zustände wie z.B. der sogenannte Bonding- und Antibonding-Zustand, bei denen ein Elektron auf beiden gekoppelten Quantenpunkten verteilt ist. Bei angelegter Spannung wird der Strom (I), das Schrotrauschen (S) sowie insbesondere das Verhältnis der beiden, der Fano-Faktor ($F = S/2eI$), untersucht. Für einen symmetrischen Doppelquantenpunkt steigt eine typische Strom-Spannungskurve (I-V) stufenweise an, wobei die Stufenpositionen das Spektrum der Quantenpunktstruktur widerspiegeln. Das Schrotrauschen ist relativ zu unkorreliertem Transport wegen des Pauli-Prinzips unterdrückt. Besteht eine Asymmetrie des Doppelquantenpunktes, beispielsweise durch ungleiche Kopplungen an die elektronischen Zuleitungen oder durch nicht resonante Quantenpunktniveaus, resultiert dieses in asymmetrischen Strom-Spannungskurven und einem asymmetrischen Rauschverhalten für jeweils positive und negative Spannungen. Bei starker Asymmetrie in beiden Fällen zeigt das System einen negativen differentiellen Leitwert sowie erhöhtes Rauschen. Es wird beschrieben, dass dieses Verhalten auf Korrelationseffekte der Elektronen zurückzuführen ist, welche durch die ausgedehnte Wellenfunktion in Kombination mit der Coulomb Wechselwirkung in diesem System besonders stark hervortreten. Im Vergleich dazu zeigt das häufig untersuchte, "lokale" Anderson Modell im Falle einer reinen rechts/links asymmetrischen Kopplung dieses Verhalten nicht.
Im Gegensatz zu dem oben diskutierten Doppelquantenpunkt kann auch ein völlig sym-

metrisches System, bestehend aus drei in Reihe gekoppelten Quantenpunkten, starke Korrelationen im elektronischen Transport aufweisen, die sich in Form eines extrem erhöhten Schrotrauschens zeigen. Bei einem solchen System ist der mittlere Quantenpunkt nicht direkt mit den Zuleitungen gekoppelt. Die komplexe Struktur der elektronische Wellenfunktionen, die insbesondere von der Stärke der Coulomb-Wechselwirkung im Vergleich zum elektronischen Hüpfen zwischen den Quantenpunkten abhängt, hat entscheidenden Einfluss auf die beobachteten Transporteigenschaften. Beispielsweise wird durch eine starke Coulomb-Wechselwirkung zwischen benachbarten Quantenpunkten die Triplet-Wellenfunktion dahingehend beeinflusst, dass sich zwei Elektronen hauptsächlich auf den beiden äusseren Quantenpunkten aufhalten. Dadurch wird das sequentielle Tunneln zu bestimmten elektronischen Zuständen wie dem Quadruplet (drei Elektronen) unterdrückt. Es wird gezeigt, dass eine Konkurrenz zwischen den oben beschriebenen Prozessen und anderen am Transport teilnehmenden, nicht unterdrückten Prozessen zu dem erwähnten stark erhöhten Schrotrauschen führt, allein aufgrund der intrinsischen elektronischen Struktur. Das erhöhte Schrotrauschen ist insbesondere für Experimente relevant, in denen die Messung des oft schwachen Schrotrauschsignals vor dem Hintergrund des 1/f-Rauschens schwierig ist.

Die entwickelte numerische Methode erlaubt desweiteren eine Untersuchung von Kotunnelprozessen in Quantenpunktsystemen, die vor allem die Transporteigenschaften in Bereichen wie der Coulomb-Blockade entscheidend beeinflussen, in denen sequentielles Tunneln unterdrückt ist. Eine Analyse des Anderson Modells im Coulomb Blockade Regime zeigt, dass intrinsische Energieskalen wie die inelastische Kotunnel-Anregung und die sequentielle Tunnelbarriere aus charackteristischem Verhalten des Schrotrauschen bzw. Fano-Faktors bestimmt werden können.

Ein weiterer Transportprozess, der eine wichtige Rolle innerhalb der Coulomb-Blockade spielt, ist das Kotunneln-induzierte sequentielle Tunneln (KIST), welches in einem Quantenpunkt mit zwei oder mehreren Niveaus auftritt. Dieser Transportprozess zeigt sich im differentiellen Leitwert als eine zweite Stufe, die nach der ersten inelastischen Kotunnel-Stufe auftritt. Während die inelastische Kotunnel-Anregung von der Gatespannung unabhängig ist, variiert die Kotunnel-induzierte Anregung mit ihr. In dieser Arbeit konnte erstmals auch im Schrotrauschen bzw. im Fano Faktor eine von der Gatespannung abhängige charakteristische Energieskala der KIST-Prozesse in Form eines Dreiecks innerhalb der üblichen Coulomb-Diamanten gesehen werden. Der Fano-Faktor reflektiert den KIST-Transportbereich mit noch grösserer Sensitivität als der differentielle Leitwert.

Zusammenfassend wurde in dieser Arbeit eine numerische Methode entwickelt, die den elektronischen Transport sowie die Rauscheigenschaften von nanoskaligen Systemen wie Quantenpunktsystem beschreibt. Es wurden neuartige physikalische Prozesse gefunden und erklärt, die zu einem besseren Verständnis experimenteller Transportmessungen beitragen sowie von Bedeutung für mögliche technologischen Anwendungen sein können.

Contents

Chapter 1

Introduction

Recent years have witnessed an enormous progress in fabrication techniques for electronic devices working on the nanometer scale. With the reduction of feature sizes of electrical components the motion of free carriers becomes more and more confined. The strong confinement of charge carriers will eventually lead to quantum mechanical effects of which a thorough understanding is mandatory in the course of miniaturization. A prominent example of a quantum mechanical effect is the conductance quantization in quantum point contacts [1].

Owing to their smallness, nanoscale systems such as quantum dots, nanowires, single molecules and short carbon nanotubes exhibit interesting transport characteristics [2, 3, 4, 5, 6, 7, 8, 9] which are based on their discrete energy structure and correlations in the electronic transport process [10]. Additionally, interaction effects of electrons start to play an important role which lead to well known phenomena such as the Coulomb blockade [11] or the Kondo effect [12, 13, 14] at very low temperatures.

In the present work we will study the non-equilibrium transport through quantum dot systems. We will focus on characteristic fingerprints of their electronic spectrum as well as on correlation effects that are reflected in the transport properties.

Quantum dots are small, nanosize islands that are either structurally or electrostatically isolated from the outside world. In analogy to real atoms quantum dots contain a small number of electrons (e.g. 1-100) that are bound by a confining potential and have discrete energies [2]. When studied in electronic transport experiments single quantum dots exhibit atomic-like spectra with a shell structure and show a manifestation of Hund's first rule [15]. Similarly, several strongly coupled quantum dots allow electrons to be delocalized over the entire dot system, resembling a molecular state. In this case the inter-dot coupling has to be strong and coherent whereas the coupling of the interfacial dots to the leads is usually much weaker. The described similarities to real atoms and molecules have led to the terms "artificial atoms" and "artificial molecules" for single and coupled quantum dots, respectively. These systems constitute excellent candidates for studying electronic transport in molecular nanostructures on mesoscopic length scales. Tunable tunneling barriers, a known fixed charge number on the dots as well as additional gate electrodes to control the dots electrostatic potential are just some of their advantages.

The Coulomb blockade is an important concept in describing single electron tunneling effects in nanoscale systems which are coupled weakly to large reservoir leads. It refers to a situation in which electronic transport is suppressed due to the Coulomb repulsion between electrons below a certain bias threshold. In order to observe such behavior, the charging energy which is essentially the energy needed to add an electron to the nanoscale system, has to be large compared to the temperature. Experiments on semiconductor quantum dot systems with their tiny capacitances ($C \approx 10^{-15}\,\mathrm{F}$) are therefore performed at low temperatures in the range of $10^{-3}K - 1K$. Molecular systems having still smaller capacitances ($C \approx 10^{-18}\,\mathrm{F}$) can display charging effects up to room temperature [16] which makes them extremely interesting from a technological point of view.

The interplay of charging effects as well as quantum confinement gives rise to a wide range of interesting physics [2, 17, 18]. Research groups worldwide study current-voltage curves (I-V's) and the differential conductance ($\partial \mathrm{I}/\partial \mathrm{V}$) in electronic transport measurements searching for characteristic fingerprints of the nanoscale systems. Typical I-V's of quantum dots and molecules show Coulomb blockade behavior followed by a non-linear stepwise increase of the current-voltage characteristics [19, 20]. The step positions are defined by the discrete excitation spectrum and thus reflect the electronic properties of the quantum system. Asymmetric I-V's as well as regions of negative differential conductance ($\partial \mathrm{I}/\partial \mathrm{V} < 0$) have been observed but are often difficult to relate to intrinsic properties of the molecule or quantum dot. One possible source of asymmetric I-V's are asymmetric contacts leading to coupling parameters of different strengths. Since the current contains information only about a combination of the coupling parameters, it can be difficult to determine them separately. Also the number of the electronic states participating in transport as well as the relative strength of the Coulomb interaction with respect to other intrinsic energy scales of the nanostructure are not revealed in a current measurement alone.

One way to gain more information is to study the shot noise. The shot noise is a general property of electrical conductors and is related to the correlations of current fluctuations in time. In nanoscale systems where the current is carried only by few electrons, statistical fluctuations in time can become very strong. They are due to the discreteness of charge which is quantized in terms of the elementary charge e. In contrast to the current which contains information about the transmission properties of the system, the shot noise reflects the dynamical properties of the transport process. It is known from theory [21, 22, 23] as well as from experiments [24, 25] that the shot noise is much more sensitive to the electron-electron interactions than the average current. Furthermore it reveals details of the nanostructures low energy spectrum, in particular when studied in the Coulomb blockade regime. The coupling parameters of the quantum dot's electronic states provide another energy scale that the shot noise is very sensitive to. In fact, analytical expressions relating the plateau values of the shot noise directly to the couplings to the left and right lead have been presented earlier [26, 27, 28] and hence allow the extraction of coupling parameters from experimental data. We will elaborate more on the aspect of asymmetries in chapter 4 in which asymmetric couplings and non-resonant quantum dot levels for the case of an double quantum dot, i.e. an artificial diatomic molecule, are discussed.

In mesoscopic systems it has become customary to use a dimensionless quantity, called the Fano factor, instead of the shot noise. The Fano factor F is defined by the shot noise S divided by $2e$ times the average current I, i.e. $F = S/2eI$. The denominator is referred to as the Schottky or Poissonian noise value since it was originally discovered by Schottky in vacuum tubes in which electron transport events obeyed a Poissonian distribution function. In this case and in all other cases where electron transport is due to uncorrelated, independent events the Fano factor turns out to be equal to unity, $F = 1$, which is referred to as a Poissonian Fano factor. In fermionic systems the Fano factor is mainly suppressed with respect to the Poissonian value due the Pauli principle, leading to sub-Poissonian values $F < 1$. On the other hand in certain asymmetric situations or as a consequence of strong interaction effects the Fano factor can become even super-Poissonian, $F > 1$, which we will discuss in some detail in chapter 4 and 5.

So far a weak coupling situation of the nanoscale system to the reservoir leads has been considered. In this picture the electronic charge is transferred one by one which is referred to as sequential tunneling. In theory these processes can be accounted for within a first order perturbative expansion in the coupling strength Γ. In the Coulomb blockade regime where sequential transport is exponentially suppressed second order processes which appear within the perturbative expansion in the coupling Γ start to be important. These processes are termed co-tunneling processes since they describe the tunneling of two electrons at a time via an intermediate, virtual state of the dot system. Electron co-tunneling leaves characteristic fingerprints both in the current and in the shot noise. It has been observed in a number of experiments [5, 6, 29] at low bias in the Coulomb blockade regime.

The aim of this thesis is to study non-equilibrium electron transport through the quantum dot systems mentioned above. For that purpose a diagrammatic technique that allows for a perturbative expansion of the current and shot noise is applied and extended within a computational approach to describe complex multilevel quantum dot systems. We account for the most relevant parameters such as the spin of electrons, their Coulomb interactions and the delocalized nature of the electronic wavefunctions.

Sequential as well as co-tunneling effects in transport will be discussed and related to experimental findings where possible.

About this thesis

This thesis is organized as follows. We start with an introductory chapter focusing on basic concepts of electronic transport in nanoscale systems. Specifically we consider quantum dot systems and discuss them in the context of their atomic- and molecular-like spectra. We introduce the concept of Coulomb blockade which is a crucial effect in tunneling transport in the presence of electronic interactions. In addition to the current the shot noise is an important quantity which contains information about electronic transport properties. We also provide an overview of classical noise sources as well as a description of shot noise for mesoscopic conductors. We give a brief summary of recent experimental findings on current and conductance as well as shot noise measurements that relate to our theoretical results.

In the third chapter we resume some aspects of the real time transport theory developed in references [30, 31, 32] as relevant to our problem. In particular the current and shot noise are formulated within a diagrammatic approach up to second order in the coupling constant following the work of [33]. As a major result of this thesis we sketch the computational implementation of a general second order transport description for the current as well as the shot noise for multilevel electronic systems. The crucial ingredients in this approach are the second order transition rates which we explicitly show how to calculate. Mathematical details involved in the calculation are presented in appendix C. Furthermore several schemes to solve the resulting equations are identified and their validity and usefulness are evaluated in various transport regimes.

The forth chapter concentrates on sequential transport in single quantum dots and coupled quantum dot systems. As an introduction to basic features of the electronic transport through quantum dots systems we first discuss a single two level quantum dot including relaxation of the quantum dot states due to photon emission processes. Interesting effects such as negative differential conductance (NDC) and super-Poissonian noise are identified and their origin explained. In order to study the influence of delocalized electronic wavefunctions on the current and shot noise we focus on a double quantum dot system (DQD) with strong inter-dot coupling [34]. The electronic wavefunctions now split into bonding and anti-bonding states where one electron is shared between the two dots. Motivated by recent experimental setups we investigate the effect of asymmetries such as asymmetric level coupling and detuned energy levels on the current and shot noise and discuss how the the nature of the electronic wavefunction in combination with Coulomb interactions give rise to features like NDC and super-Poissonian noise [34].

In contrast to the DQD longer chains of coupled quantum dots, where the middle dots are not directly coupled to the leads may show strong correlations in form of super Poissonian noise even in symmetric situations [23]. We discuss a coherent triple quantum dot in the presence of strong nearest neighbor Coulomb interactions. The influence of the interactions on the nature of the electronic wavefunctions, specifically the triplet and quadruplet states, is investigated and found to be responsible for the strong noise enhancement above the sequential tunneling threshold.

In chapter 5 we focus on co-tunneling processes that become important when sequential tunneling is suppressed. Whereas previous work mainly concentrated on the single level Anderson model, we describe elastic and inelastic co-tunneling in a two level quantum and analyze the dependence of the co-tunneling step features with varying temperature and coupling constants Γ. In this system another interesting transport regime, namely co-tunneling assisted sequential tunneling, shows up. We investigate in detail the gate voltage dependence of the associated energy scale and present how a triangle structure arises in the differential conductance as well as the Fano factor inside the typical Coulomb diamonds.

Chapter 6 constitutes our conclusions on electronic transport in the discussed quantum dot systems. A brief outlook is presented in the end. The appendices A, B and C contain detailed information on the diagrammatic rules, the first order transition rates and the second order transition rates, respectively. They mostly contain mathematical definitions and solutions which are of interest if one desires to use our theoretical approach or wishes to explore the details.

Chapter 2

Basic concepts of electronic transport in nanoscale systems

In the present chapter we describe the electronic properties of nanoscale systems, in particular quantum dots which exhibit similar transport features like atoms or molecules. Furthermore we discuss the most prominent features of single-electron transport such as the Coulomb blockade. Special emphasis is put on the discussion of the shot noise, the dynamical current-current fluctuations, and the Fano factor as they have proved to be very useful tools to study electronic correlations in mesoscopic systems. The last section of this chapter focuses on recent experimental work which provides a background for our subsequent theoretical considerations.

We will start by characterizing different types of quantum dots such as vertical and lateral setups. Specifically we discuss these systems in the context of their atomic- and molecular-like spectra as revealed from transport experiments [15, 35]. Single quantum dots display features of a shell structure which is characteristic for atoms. Arrays of coupled quantum dots allow for delocalized electrons over the whole dot structure. A double quantum dot with strong inter-dot coupling thus resembles a diatomic molecule. The described similarities to real atoms and molecules have led to the terms *artificial atoms* or *artificial molecules* for single and coupled quantum dots respectively. Quantum dot experiments with their defined control over system parameters therefore provide excellent systems to study atomic and molecular transport properties on mesoscopic length scales.

2.1 Quantum dots: Artificial atoms and molecules

Quantum dots are nanosize “islands” on which electrons are confined in the three spatial dimensions and isolated either structurally or electrostatically from the outside world [2]. Due to their small dimensions they have small capacitances and can display a discrete energy spectrum. Typically quantum dots consist of many atoms ranging from hundreds to millions but only a small number (< 100) of electrons that are relevant in the electronic transport can be free. There exist two types of quantum dots, namely metallic and semiconducting quantum dots. The latter show energy quantization already at structure sizes around 100 nm while metallic dots having a much higher density of states usually have a quasi continuous spectrum [36]. We will focus on semiconducting quantum dots which can more easily be contacted with macroscopic electrodes and thus be studied in electrical transport measurements.

Two fabrication techniques dominating the variety of experimental realizations of quantum dots can be distinguished: *Lateral* and *vertical* quantum dot structures. Fig. 2.1 depicts a typical lateral quantum dot setup taken from [19]. A two dimensional electron gas (2DEG) is formed at the interface of the different semiconductor materials GaAs/AlGaAs whereas the motion in the direction perpendicular to the surface plane is confined. By means of negative voltages which are applied to the top "finger" gate electrodes the 2DEG is depleted in the area underneath the gates and tunneling barriers can be formed between the gate pairs F-1, F-2 and F-3. Thus the device can be used to form a single quantum dot as well as a double quantum dot. Additionally other gate electrodes (e.g. gate I, II in Fig. 2.1) can be used to vary the electrostatic potential of the individual dots. The tunability of the tunneling barriers provides a great advantage of the lateral quantum dot structures. However, in most experimental setups the wanted effect of an additional gate electrode provokes the negative side effect, that the tunneling barriers are also influenced and thus can not be kept constant.

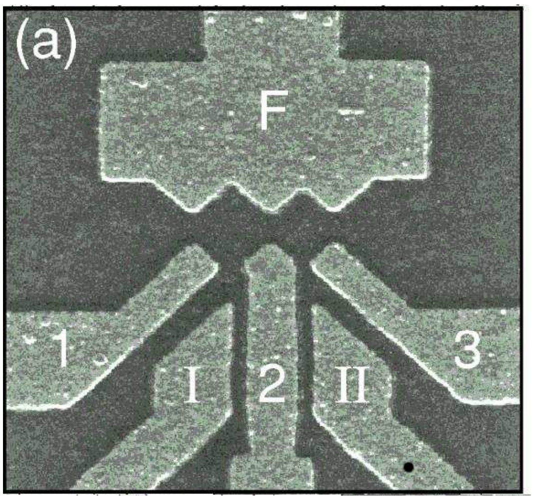

Figure 2.1: *Scanning electron microscopy (SEM) picture of a lateral quantum dot structure defined by six metallic gates on top of a GaAs/AlGaAs heterostructure. The tunneling barriers are formed underneath the gate electrodes when a electrostatic potential is applied to them [19].*

In a typical transport measurement the coupling of the right and left contact region is usually weak (of the order of 10 μeV) which leads to single electron tunneling through the structure. Since the charging energy (see following section 2.2) in these systems is of the order 10-100 meV transport experiments must be performed at low temperatures (0.1-1K).

Vertical quantum dots are formed of layered semiconducting heterostructures. Here the current flows vertically with respect to the 2DEG plane inside the heterostructure. The tunneling barriers are due to large bandgap material (indicated by AlAs layers in the schematic sketch depicted in Fig. 2.2) and are usually very high (> 100 meV). The lateral confinement is provided by pillars that are etched out of the layered heterostructure and have an extremely small diameter [15]. The contacts at the emitter and collector electrodes can be easily defined. However it is much more difficult to allow for an additional gate electrode that is usually structured by metallic coating of parts of the pillar. On the other hand the tunneling barriers are very constant in strength and thus less sensitive to external fluctuations [2].

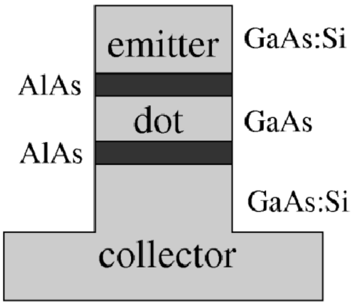

Figure 2.2: *A vertical quantum dot structure made up of a zero dimensional region sandwiched between semiconducting heterostructure layers taken from [37].*

Having discussed the experimental realizations of quantum dots we want to address the issue why under certain conditions quantum dot systems can be regarded as molecular nanostructures. As in real atoms small semiconductor quantum dots have a completely discretized zero dimensional energy spectrum with a total charge that is restricted to an integer number. In analogy to the Coulomb potential of a nucleus electrons are bound in a quantum dot by the confining potential of the structure. Therefore they are often referred to as *artificial atoms*. First transport experiments [15] on semiconductor vertical quantum dots have shown evidence for a shell structure together with a manifestation of Hund's first rule. However, it is worth mentioning some differences between these artificial atoms and their real counterparts. While real atoms and molecules have a $1/r$-potential the confining in quantum dots is much weaker and has a power law $\sim r^{\alpha}$ behavior, where α denotes an integer number. Thus the resulting spectra are very different. Quantum dots have a size that is approximately three orders of magnitude larger than real atoms. Thus they can be manipulated much more easily than real atoms. For instance, the confining potential can be manipulated by means of a gate electrode that is electrostatically coupled to the dot structure. Furthermore the quantum dot states can be probed by a transport measurement using the attached source and drain electrodes whereas in real atoms, experiments mostly rely on the use of optical techniques.

In contrast to single atoms more molecules consist of a number of atoms where the electrons are able to jump from one constituent atom to another thereby lowering the total energy of the system. As a consequence molecules have a spatially delocalized electronic wavefunction. To realize a molecular state in a quantum dot system several single quantum dots need to be strongly coupled together in a coherent way. The outer couplings of the interfacial dots to the reservoir electrodes are usually much weaker and couple incoherently. The setup displayed in Fig. 2.1 allows for an experimental realization of a molecular state in a double quantum dot (DQD) structure. One can realize for instance a bonding (anti-bonding) state in which one electron is shared between the two dots. If the inter-dot tunnel coupling is large the situation resembles a covalently bonded *artificial molecule.*

There is a huge general interest to study these systems since they provide a perfect playground for experimentalists to observe atomic or molecular transport properties on mesoscopic length scales. From an technological point of view quantum dot systems have promising applications as optical memory elements, lasers, photodetectors etc. [2]. In particular double quantum dot structures are seen as potential candidates for a core element of quantum computers, the q-bit [38, 39].

2.2 Tunneling transport and Coulomb blockade

Essentially the ability to observe single-electron tunneling effects relies on the *Coulomb blockade* effect. Let us consider a small island that is tunnel-coupled to two electrodes. The tunnel junctions are well described in a capacitative picture by C_L and C_R. Due to the electrostatic Coulomb interactions between electrons the classical charging energy E_{ch} has to be overcome in order to populate the island with an additional electron. We write

$$E_{ch} = E_C(N - n_G)^2 \tag{2.1}$$

where N denotes the excess charge on the island and $n_G = \frac{1}{e}C_G V_G$ is the number of external charges due to the applied gate voltage. The energy scale E_C is given by

$$E_C = \frac{e^2}{2C_\Sigma}. \tag{2.2}$$

Here C_Σ is the effective total capacitance of the entire island structure. Eq. 2.1 describes a parabola for different values of N. The external charge n_G can be varied continously. At low voltages and low temperature, i.e. $E_C >> max\{k_BT, eV_{bias}\}$, the number of island charges is fixed and corresponds to the charge of the ground state. At half integer values of n_G the energy of two successive charge sectors, for instance $q = Ne$ and $q = (N+1)e$ become degenerate which leads to a peak in the current (and the conductance $G = \partial I/\partial V$). As a result the current periodically oscillates as a function of the gate voltage (excess charge n_G) which is known under the term *Coulomb oscillations* [17]. In between the current is suppressed signalizing the Coulomb blockade.
This classical picture of the charging energy often holds also for quantum mechanical systems. In small quantum dot systems quantization leads to a total energy of

$$E_N(n_G) = E_{ch}(N, n_G) + \sum_{l}^{N_{orb}} \varepsilon_l n_l, \qquad n_l \in 0,1 \quad \sum_l n_l = N \tag{2.3}$$

with N_{orb} quantized quantum dot levels of energy ε_l (where we have neglected the spin degrees of freedom for simplicity). The energy needed to populate the island with an extra electron is now given by the charging energy E_C plus the level spacing $\Delta\varepsilon_l = \varepsilon_{l+1} + \varepsilon_l$ of the quantum dot. For our later discussion we will choose the level spacing to be large compared to other energy scales meaning that the inclusion of one or at mostly a few orbital quantum dot levels is a sensible assumption. Note that for a very small level spacing (e.g. in the limit $\Delta\varepsilon_l \to 0$) a continuous spectrum is obtained which describes a metallic island.
However, this classical picture has its limitations. So far we have assumed a weak coupling of the quantum dot system to the leads, corresponding to opaque tunnel barriers. In this picture electrons are transferred one by one through the system which is referred to as sequential tunneling or a first order processes. Sequential tunneling can be accounted for within a first order perturbative expansion in the coupling constant Γ (Golden rule). Fig. 2.3 shows a sequential tunneling process. For a larger coupling

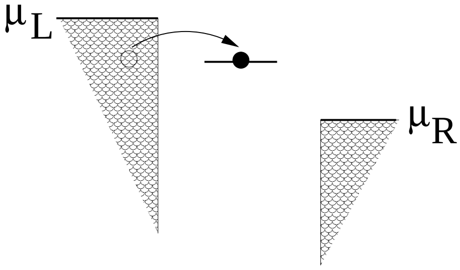

Figure 2.3: *First order or sequential tunneling process through a single quantum dot level at non-zero bias defined by the difference of the chemical potentials* μ_L, μ_R.

to the leads, corresponding to more transparent tunnel barriers, higher order tunneling processes such as the simultaneous tunneling of two electrons at a time become possible. The latter is referred to as *co-tunneling* which will be discussed in detail in chapter 5.

2.3 Shot noise and Fano factor

Noise is a general property of electrical conductors. It is defined by the electrical current-current correlations in time and may be of multiple origin. Usually experimentalists would like to get rid of the noise in order to obtain a clear signal. However during the last decade the great potential of the study of noise, specifically the quantum shot noise in mesoscopic systems has been realized since the shot noise properties of a system are fundamentally connected with the statistical properties of transport. This interest has led to a fast emerging subfield of mesoscopic physics [40, 41, 42, 43, 44, 45, 46, 47, 48, 49].
In this chapter we will summarize some basic properties of noise (following [42]) together with an analysis of the different possible sources and its corresponding qualitative behavior. We will focus on the most interesting contribution of the noise, namely the non-equilibrium shot noise in mesoscopic systems. In addition we introduce the Fano factor as a dimensionless parameter characterizing the strength of the shot noise with respect to the Schottky (uncorrelated or Poisson) limit. Experimental results on shot noise measurements in strongly correlated quantum systems can be found in section 2.4.

2.3.1 Basic properties and sources of noise

As mentioned above noise can be of several origins. We start with the description of two classical sources of noise [50], such as the Lorentzian and 1/f-noise. Lorentzian noise is due to stochastic processes with a single time constant τ and present in many electrical conductors. As a consequence the number of charge carriers (electrons) is fluctuating in a random fashion around discrete values. Therefore Lorentzian noise is often called random telegraph noise (RTN). The noise spectral density can be written as

$$S(\omega) \sim \frac{\tau}{1+\omega^2\tau^2}. \tag{2.4}$$

There are several examples for these type of fluctuations. On of them is the generation-recombination noise which is often found in semiconductors with defects. Due to electron-hole pair creation and annihilation the charge number fluctuates and Lorentzian noise is produced [51].

At low frequencies there is a dominant noise source termed 1/f-noise. The name originates from a noise spectral power density of the form

$$S(\omega) \sim \frac{1}{\omega^{\alpha}}, \tag{2.5}$$

where the exponent α is a number approximately of the order of unity. As has been mentioned before fluctuations that are due to a single time constant τ produce a Lorentzian shape of the noise power. However, if there are several time constants the superposition of many such events can lead to a long and slow time correlation which can in turn result in a $1/\omega$ behavior ([51] and references therein). This type of noise has been observed in a variety of systems meaning that the microscopic origins must be very different. From an experimental point of view one is able to avoid 1/f-noise by moving to high frequencies. At some threshold the 1/f-noise finally vanishes and white, frequency independent shot noise can be measured. The threshold frequencies differ for various systems. Since typically the 1/f fluctuators are temperature activated the frequency threshold value very much depends on the temperature of the system. For noise measurements in quantum dot setups usually temperatures of few mK are used which leads to frequency independent shot noise from frequencies $\omega \sim 10 - 100\text{kHz}$ onwards [52]. Single molecule experiments are often performed at much higher temperatures. Thus to measure the shot noise level one has to move to very high frequencies such as for example GHz [5] which makes shot noise measurements extremely difficult.
Next we want to discuss the classical shot noise which is due to the discreteness of the electric charge. Shot noise was first discovered by Schottky et al. [53] in vacuum tubes. In these systems the current originates from thermal emission of electrons in the cathode. Hence no electron correlation effects are present and transport events are entirely random. Thus, the current can be understood as a sequence of delta peaks in time where each peak corresponds to an electron pulse. The finite frequency noise is defined as the Fourier transform of the current autocorrelation function and is given by the expression

$$S(\omega) = \int_{-\infty}^{\infty} dt e^{i\omega t} \left\langle \delta I(t)\delta I(0) + \delta I(0)\delta I(t) \right\rangle, \tag{2.6}$$

where $\delta I(t) = I(t) - \langle \hat{I} \rangle$ and $\langle \hat{I} \rangle$ is the time averaged expectation value of the current operator $\hat{I}$. In the zero frequency limit ($\omega \rightarrow 0$) which is often satisfied in experiments, $S(\omega) \approx S(0)$. Hence in the following discussion we will always refer to the zero frequency shot noise.
In the case of uncorrelated, independent transport events eq. 2.6 yields

$$S_P = 2e\langle I \rangle, \tag{2.7}$$

where the characteristic shot noise value S_P is referred to as the Schottky or Poissonian noise. The name Poissonian relates to the fact that uncorrelated electron transport as it is found in the case of the vacuum tubes obeys a Poisson distribution function. Eq. 2.7 implies that if the electric charge was not quantized also the shot noise would vanish. Experiments with superconductors where the charge is carried in cooper pairs ($q = 2e$) show Poissonian shot noise values of $S_P = 4e\langle I\rangle$. This suggests that the shot noise can be used to determine the effective charge of the carrier entities [42].

Another source of noise is the thermal noise which is also called Nyquist-Johnson-noise. At non-zero temperatures thermal noise is unavoidable. Thus typically the two types of noise can not be separated in an experiment. In contrast to the pure non-equilibrium shot noise thermal noise appears without any applied bias voltage. It derives from the fluctuations of the occupation number of the system's states. In thermodynamic equilibrium the occupation number n is given by the Fermi distribution function, i.e. $\langle n\rangle = f$. The probability for a state to be occupied is also given by f whereas the probability for an empty state is $(1-f)$. This leads to $\langle(n-\langle n\rangle)^2\rangle = f(1-f)$ at finite temperatures and vanishes for $T = 0$. The occupation number fluctuations give rise to equilibrium current fluctuations in an external circuit. Thermal noise is always *white*, i.e. frequency independent.

Before we will move on to our discussion of shot noise in mesoscopic systems let us introduce the dimensionless quantity

$$F = \frac{S}{2eI} \tag{2.8}$$

which is called the Fano factor. The Fano factor is defined by the shot noise divided by the Schottky noise value. In the absence of electron correlations its value is around unity corresponding to Poissonian noise $S = S_P$. Deviations from this value are called super- and sub-Poissonian ($F > 1$ and $F < 1$ respectively) and can appear in mesoscopic systems with strong correlations which is discussed in the following chapter.

2.3.2 Shot noise in mesoscopic systems

The above discussion of noise is based on an entirely classical statistical description. When discussing shot noise in mesoscopic systems one has to treat the problem quantum mechanically [42, 54, 55, 56]. In the following we will sketch briefly the Landauer-Buettiker approach [42] and state the results for the current and noise in an equilibrium and non-equilibrium situation. The two contributions of the shot noise, the thermal noise in equilibrium and pure non-equilibrium shot noise are easily identified in this approach. Strictly speaking the presented Landauer-Buettiker results apply to non-interacting systems. However, for the systems we want to treat electron correlation effects will be important. For that reason we additionally discuss shot noise properties in correlated mesoscopic systems.

Let us start in a ballistic transport picture in which by definition no correlations are present. The mesoscopic structure or *scattering* region is attached to two reservoir

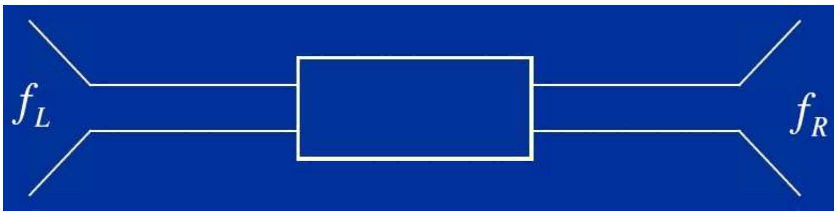

Figure 2.4: *Sketch of a scattering region (e.g. a mesoscopic conductor) attached to two electron reservoir leads. The lead electrons are assumed to be in thermal equilibrium and thus their distribution function is given by the Fermi distribution* f_L, f_R.

leads which are in thermal equilibrium and can thus be described by Fermi functions f_L, f_R (see Fig. 2.4). We assume that the scattering matrix which contains information about the transmission and reflection properties of the mesoscopic conductor is already known from a quantum mechanical calculation. Applying the Landauer-Buettiker formalism the average symmetrized current $I = (\langle I_\mathrm{R}\rangle - \langle I_\mathrm{L}\rangle)/2$ can be obtained by the expression

$$I = \frac{e}{2\pi\hbar}\sum_n \int dE\; T_n(E)[f_\mathrm{L}(E) - f_\mathrm{R}(E)]. \tag{2.9}$$

Here $f_\mathrm{r}(E) = [e^{(E-\mu_\mathrm{r})/k_\mathrm{b}T} + 1]^{-1}$ denotes the Fermi functions for the leads $r = \mathrm{L}, \mathrm{R}$ and $T_n(E)$ are the eigenvalues of a transmission matrix which are interpreted as the transmission probabilities of an eigenchannel n. In the zero temperature limit and for small bias the derivative of Eq. 2.9 with respect to bias voltage yields the Landauer equation (for many channels n)

$$G = \frac{e^2}{2\pi\hbar}\sum_n T_n(E). \tag{2.10}$$

for the conductance of the system. Eq. 2.10 shows that the conductance can be expressed in terms of transmission probabilities only.

In the case of the shot noise this is not possible anymore since in general it is the product of transmission and reflection properties. Within the scattering approach the shot noise is given by

$$\begin{aligned} S = \frac{e^2}{\pi\hbar}\sum_n \int dE\, \{T_n(E)\,[f_\mathrm{L}(E)\,(1 - f_\mathrm{L}(E)) + f_\mathrm{R}(E)\,(1 - f_\mathrm{R}(E))] \\ + T_n(E)(1 - T_n(E))\,[f_\mathrm{L}(E) - f_\mathrm{R}(E)]^2\} \end{aligned} \tag{2.11}$$

In an equilibrium situation the second part containing $f_L - f_R$ vanishes and we are left with the thermal noise

$$S = 4k_BTG. \tag{2.12}$$

with the definition of the conductance G from Eq. 2.10. The above equation Eq. 2.12 is a manifestation of the fluctuation-dissipation theorem which states that equilibrium fluctuations are proportional to the dissipation of the system (e.g. the conductance or resistance).

In the opposite limit, where $T = 0$ and a finite bias $V_b = \mu_l - \mu_R$ leading to $f_L \neq f_R$ is applied, pure non-equilibrium shot noise (also called *partition noise*) is obtained and can be written in the eigenchannel basis as

$$S = eV_b \frac{e^2}{\pi\hbar} \sum_n T_n(1 - T_n). \tag{2.13}$$

Combining Eq. 2.9 and Eq. 2.13 yields for the Fano factor

$$F = \frac{\sum_n T_n(1 - T_n)}{\sum_n T_n}, \tag{2.14}$$

which is always smaller than or equal to unity. If the scattering region was perfectly conducting (corresponding to either $\sum_n T_n = 1$ or $T_{n_0} = 1$ and $T_{n \neq n_0} = 0$) the shot noise as well as the Fano factor would vanish. On the other hand for nearly zero transmission ($T_n << 1$) the shot noise (Eq. 2.13) becomes $S = eV_b \frac{e^2}{\pi\hbar} \sum_n T_n = S_P$. With the current given by $I = V_b G$ (for the expression of G see Eq. 2.10) this leads to a Fano factor equal to unity.

Summarizing the above one finds the thermal noise dominating at low bias $eV_b << k_B T$ whereas the non-equilibrium shot noise dominates at higher bias $eV_b >> k_B T$. In [57] the crossover from thermal noise to shot noise was investigated in an STM tunneling

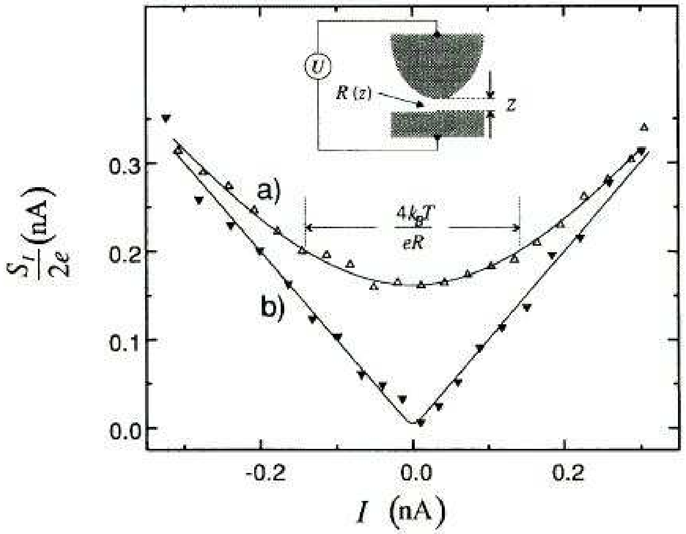

Figure 2.5: *STM tunneling experiment showing the crossover from thermal to non-equilibrium shot noise (picture taken from [57]). The cases a) and b) correspond to samples with lower and higher resistance, respectively.*

experiment. Fig. 2.5 shows the shot noise normalized by $2e$ as a function of the current. The inset depicts the experimental setup with the STM tip and a single tunneling barrier to the sample. At low bias corresponding to low current the Fano factor can be approximated by the expression $F = \coth(\frac{eV_b}{2k_BT})$ implying a divergent Fano factor at very low bias [58].

In fermionic systems in which electronic interactions are present the Fano factor is usually reduced to values smaller than unity (sub-Poissonian). One of the first experiments probing this was done by Reznikov et al. [47] showing that the shot noise in a point contact is suppressed with respect to the non-interacting value. More recent experiments on quantum dots [25, 51, 52, 59] similarly show sub-Poissonian Fano factors in the transport regime above the Coulomb blockade. Inside the Coulomb blockade regime, where transport is exponentially suppressed the Fano factor is equal to the Poissonian value of one.

Generally in local quantum dot systems such as single or multilevel quantum dots the Fano factor is typically sub-Poissonian above the sequential tunneling threshold. This can be explained to be due to anti-bunching effects of electrons because of the Pauli principle. If the level couplings are asymmetric (e.g. in the presence of magnetically polarized electrodes or a left/right asymmetry in the contacts) the Fano factor can become super-Poissonian [27, 34, 60]. Recently it was shown that enhanced noise can also be found inside the Coulomb blockade region even in symmetric systems [34, 61]. The effect relies on the thermal occupation of excited quantum dot states at low bias. On the other hand, for 'non-local' systems, such as serially coupled quantum dots super-Poissonian noise can develop even in fully symmetric situations and above the sequential tunneling threshold [23] due to the complex internal level structure of the dot system. We will discuss this system in some detail later in chapter 4.

2.4 Experiments: Transport measurements in quantum dot systems and molecules

In this section we will review and comment on recent transport measurements in quantum dot and single molecule systems that relate to our theoretical work. We will start with the discussion of current and conductance measurements in single and coupled quantum dots in the sequential as well as the co-tunneling regime. These measurements allow to extract information about the quantum dot spectrum as well as underlying asymmetries. However, more recent experimental activities include the analysis of shot noise since additional insight into the quantum transport properties can be gained and thus allow for a more detailed characterization of the nanostructure (see also chapters 2.3 and 4).

In the case of single molecules [62, 63, 64, 65, 66] one of the greatest scientific challenges is to provide for the molecule-electrode contact in a reproducible way. Current and conductance measurements on these systems show Coulomb blockade effects as well as elastic and inelastic co-tunneling signatures [3]. Also phonon vibrations are frequently observed. Only very few shot noise measurements are reported for molecular systems [67]. We will discuss in detail a shot noise measurement [5] of a short carbon nanotube in the Coulomb blockade regime that fits well to our theoretical results presented later in chapter 5.

2.4.1 Quantum dots

Due to their small dimensions quantum dots show Coulomb blockade behavior and have a discrete energy spectrum. Transport measurements on lateral semiconductor quantum dots [68, 69] in experimental setups similar to the ones depicted in Fig. 2.1 reveal non-linear current-voltage characteristics. Tuning the tunneling barriers by means of the corresponding “finger electrodes” the lateral QDs can be weakly coupled to the left and right reservoirs. To achieve transport a bias is applied (usually symmetrically) between the two electrodes. At low bias sequential transport is suppressed by the Coulomb blockade whereas with increasing bias the current rises in steps. Each step position is defined by the dot’s energy excitation spectrum. The setup from Fig. 2.1 further allows to study two coupled quantum dots that may form molecular states which are delocalized over the entire double dot structure. Depending on the inter-dot coupling strength the two dots can form “ionic-like” states for weak inter-dot coupling as well as “covalent-like” states in the case of strong inter-dot coupling. The latter resembles very much a typical molecular state. In the experiments discussed in [19] the current-voltage characteristics (I-V) were investigated for the case of weak inter-dot coupling. Again Coulomb blockade was observed but additional features such as negative differential conductance (NDC) and peaks in the current were found. In chapter 4 we present our theoretical results on transport through a DQD with strong inter-dot coupling. Similar to the experiment mentioned above we find features such as Coulomb blockade and NDC. Current peaks are absent since they are due to resonant effects appearing in the ionic-like systems but not in the strongly coupled, covalent type of DQD states.

There is a huge variety of systems including vertical as well as self assembled quantum dot structures that contain a weak dot-electrode coupling and thus all display similar transport features as described above. If the coupling to the electrodes is increased, for instance up to the value of the temperature, higher order tunneling processes start to play a role. Co-tunneling is a second order contribution and has been studied in many experimental as well as theoretical works [6, 22, 29, 58, 69, 70]. We want to discuss two experiments as a background for our theoretical results presented in chapter 5.

The first is a transport measurement in a single small semiconductor quantum dot with known total charge at very low temperatures ($\sim 15mK$). The setup allows for an additional gate which manipulates the electrostatic potential of the dot. Coulomb blockade behavior shows up in form of the Coulomb "diamonds" in a grey scale plot of the conductance versus the applied bias and gate voltage (see Fig. 2.6). The left inset displays the Coulomb diamond of the two electron ground state ($N = 2$). Due to the strong dot-electrode coupling co-tunneling processes in which two electrons tunnel simultaneously play a significant role in the Coulomb blockade (inside the Coulomb diamond). Elastic co-tunneling processes occur via intermediate virtual states at arbitrary bias. Hence they do not introduce an energy scale inside the Coulomb diamond. In contrast inelastic co-tunneling is only possible in a finite bias situation. Here one electron tunnels into a high energy state while another one occupying a lower energy state tunnels out of the dot. Thus the process requires some energy which is defined by the spectrum and is called the inelastic co-tunneling energy ε_{co}. In the above experiment inelastic co-tunneling can be observed in the region defined by the vertical, gate voltage independent line and the Coulomb diamond edge. Depending on the the dots low energy spectrum an inelastic co-tunneling process can directly be followed by a sequential tunneling process. The combined process thus is applicable at the same bias as the pure inelastic co-tunneling. The right inset depicts an inelastic co-tunneling process which leaves the dot in an excited state and can thus be followed by a sequential tunneling process.

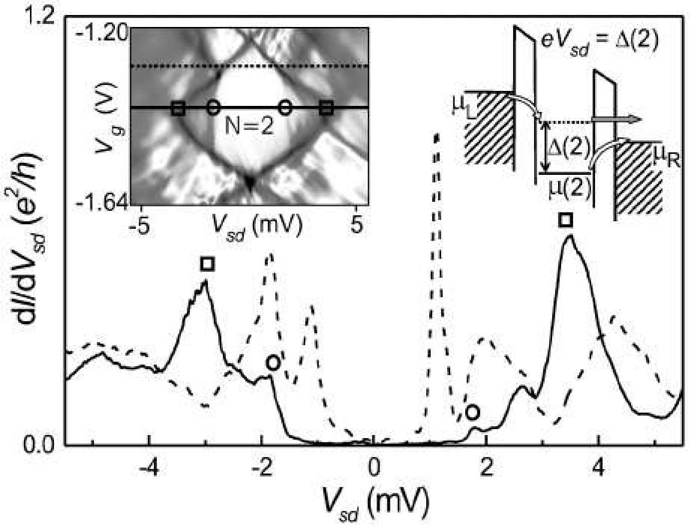

Figure 2.6: *Differential conductance vs. applied bias for two different fixed gate voltages. The solid line corresponds to a lower gate voltage as the dashed line as indicated in the left inset. The left inset shows measured Coulomb diamonds where the diamond edges mark the onset of sequential tunneling and the vertical gate voltage independent lines correspond to the onset of inelastic co-tunneling. The picture was taken from [29].*

A similar experiment in this regime was performed in [6]. Here the current and conductance through a lateral quantum dot structure at non-zero magnetic field (lifting the spin degeneracies) were studied. Similar transport features as in the Franceschi experiment were observed (see Fig. 2.6). However, additionally diagonal lines inside the Coulomb blockade that join excitation lines outside the diamond structure were found. This was interpreted as sequential tunneling out of an excited state that had been occupied by a proceeding inelastic co-tunneling process. As a consequence the same excited state plays a role in sequentially dominated transport outside the Coulomb diamond. The region between the diagonal lines and the Coulomb diamond edge is referred to as the co-tunneling assisted sequential tunneling regime. It has been discussed as the limiting factor for the operation of single electron devices that rely on the Coulomb blockade effect. We investigate this regime in detail in chapter 5 and additionally include a shot noise analysis to characterize the involved tunneling processes in more detail.

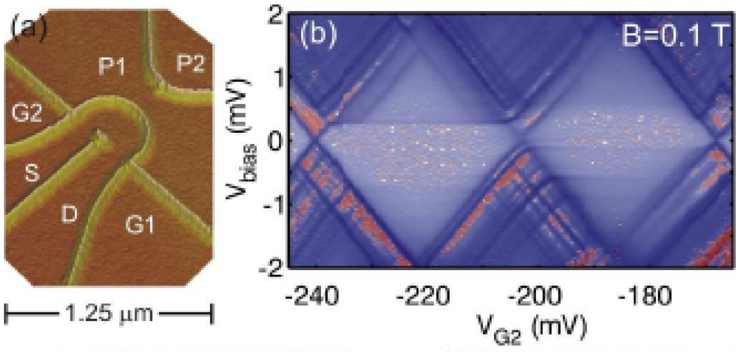

Figure 2.7: *Right: Differential conductance versus applied bias for two different magnetic field B taken from [6]. Co-tunneling is observed in form of the horizontal gate voltage independent lines. Diagonal lines inside the diamond correspond to the co-tunneling assisted sequential tunneling regime. The excited state involved in the process later gives a contribution in the sequentially dominated transport regime outside the Coulomb diamond. Consequently the diagonal lines inside the Coulomb blockade match or join the lines resulting from transport through excited states. Left: AFM picture of the experimental setup of the quantum dot structure. The electrode reservoirs are denoted by S (source) and D (drain), the lateral gates G1, G2 are used to tune the tunneling barriers and the other gates P1, P2 to manipulate the electrostatic potential and thereby the number of electrons of the dot.*

Although shot noise measurements in single quantum dots or other nanostructures are still rare, some experimental results are available in literature. The interest in shot noise is mainly attributed to its known sensitivity to the correlations of the system as well as to the coupling between the leads and the studied nanostructure. We want to discuss an experiment [25] in which the sub-Poissonian noise in self assembled InAs quantum dots was measured. The grown dot structures form several vertical quantum dots of different size in parallel. However only few dots really participate in the transport measurement. The largest dot with the lowest level energy enters first into the bias window. The current and Fano factor (here denoted by α) vs. bias voltage can be seen in Fig. 2.8. For low bias the current is exponentially suppressed by the Coulomb blockade. When the first excitation energy is matched by the applied bias the current rises in form of a step. The next step that follows afterwards corresponds to another individual quantum dot and not to a higher lying excitation energy of the first dot. This is a peculiarity of the above experiment since many dots are being measured. The step feature is followed by a plateau which linearly decreases due to bias dependent tunnel couplings. The Fano factor α is Poissonian in the Coulomb blockade regime

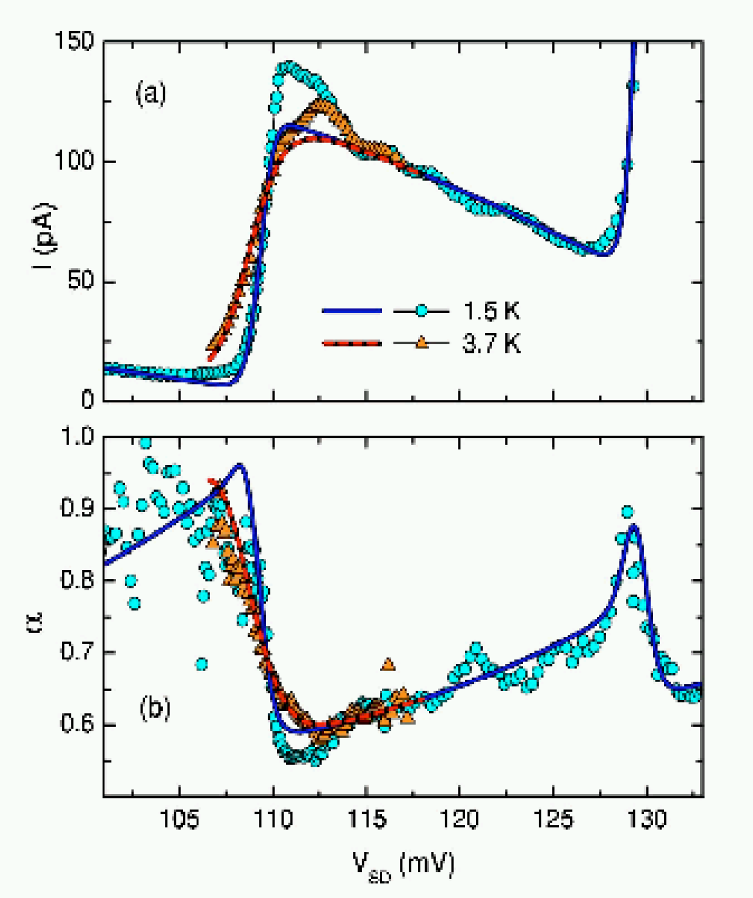

Figure 2.8: *Current I and Fano factor α for a self assembled vertical quantum dot. Different colors correspond to different temperatures. Measured data points are denoted by triangles as well as circles. The Fano factor shows typical Poissonian values in the Coulomb blockade and is reduced to sub-Poissonian values in the sequential transport regime. The figure is taken from [25].*

signalizing uncorrelated electron transport. When the dot ground state level enters the applied bias window, sequential transport sets in. Due to the Pauli principle and the Coulomb repulsion of electrons the tunneling events are anti-bunched leading to a reduced Fano factor of values between one half and unity.

2.4.2 Molecules

In the following we describe transport measurements in *real* molecules which has been studied in many works [3, 71, 72]. Single molecule setups are extremely sensitive to their environment. In particular the coupling of macroscopic electrodes to the single molecules is a scientific challenge. Therefore usually a large number of measurements is performed and then statistically analyzed. A commonly used experimental technique to fabricate nanoscopic electrodes is the mechanically controlled breakjunction technique [7, 16, 72, 73, 74, 75] in which a metallic wire (usually gold) on a flexible substrate is bent by pushing a rod. During this process the wire breaks and a nano sized gap is formed between two electrodes. The coupling of the molecules to the electrodes is provided for instance by thiol end groups or other elements depending on the type of molecule that is contacted and the desired coupling strength. In [4] a single molecular diode, made of a π-conjugated combination of phenyl-ethynyl rings was designed showing unambiguously an asymmetric current-voltage curve. Similar to quantum dot experiments step features in the current as well as peaks in the differential conductance were found as a result of the discrete energy spectrum of the molecule.

Other interesting features such as negative differential conductance (NDC) were found in [76] and in single molecule magnets (SMMs) [77]. The NDC effect is explained to be a result of the spin blockade of the current which is completely suppressed in this regime. A theoretical model using a sequential transport picture similar to ours (as presented in chapter 4) but with additional terms in the Hamiltonian accounting for the magnetic properties of the molecule was applied and found to explain well the observed features.

In order to achieve a more profound understanding of the coupling situation in single molecule experiments the shot noise may serve to be a useful tool. As mentioned before, the shot noise is very sensitive to asymmetries of the couplings to the left and right electrode as well as to interaction effects between electrons on the small molecule. However shot noise measurements for single molecules are extremely difficult. Up to the present day only very few shot noise measurements on molecules are reported [67]. This may partly be due to the fact that in addition to the challenging experimental setup one has to measure at very high frequencies ($\sim$ GHz) to observe shot noise. In [5] the shot noise in a carbon nanotube quantum dot in the co-tunneling regime has been measured. A small gap semiconducting nanotube was placed between two electrodes

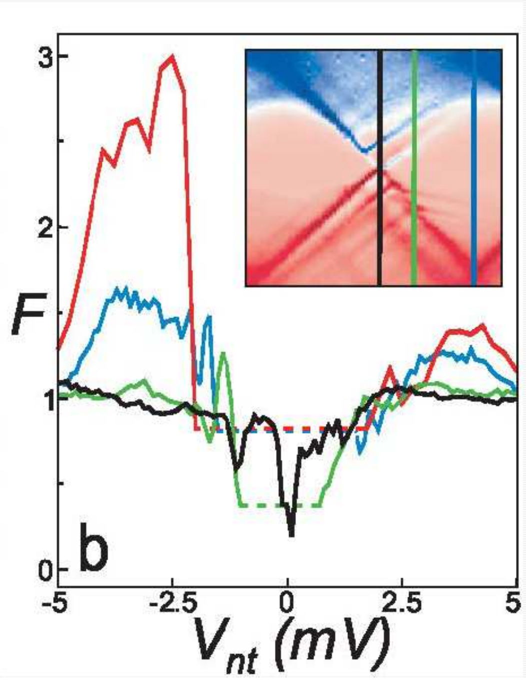

Figure 2.9: *Fano factor versus applied bias voltage at different gate voltages. The curves show asymmetric behavior with respect to bias and a super-Poissonian Fano factor at the inelastic co-tunneling energy scale (approximately around* $2meV$*). Inset: Coulomb diamonds of the Fano factor vs. bias (vertical axis) and gate voltage (horizontal axis). The color scale is defined from blue corresponding to the Poissonian value of* $F = 1$ *to red for* $F = 2$*. The figure was taken from the work of Onac et al. [5].*

with a backgate below the isolating substrate. Tunneling barriers were formed at the contacts. At low temperatures the nanotube exhibited Coulomb diamonds implying that a quantum dot was formed. The shot noise was measured via a complex on-chip detector consisting of a superconductor-insulator-superconductor (SIS) junction. Fig. 2.9 depicts the Coulomb diamonds of the Fano factor as well as the traces at various fixed gate voltages. Considering the traces of the Fano factor at three fixed gate voltages one finds that the Fano factor is Poissonian in the Coulomb blockade around zero bias. In the case of the black trace which corresponds to a gate voltage near the degeneracy point of the Coulomb diamond the Fano factor stays Poissonian also above the sequential tunneling threshold (outside the diamond). All other traces show a super-Poissonian Fano factor with values around $F = 2$ at a characteristic energy scale of $\varepsilon \sim 2$meV which is identified to be the inelastic co-tunneling energy scale. The observed experimental data has been predicted earlier on a theoretical basis by [22]. In chapter 5 we will discuss in detail the physical processes leading to the experimentally observed noise enhancement above.

Chapter 3

Real time transport theory

To describe electronic transport through mesoscopic systems one has a wide choice of different theories and formalisms [30, 32, 78, 79, 80, 81, 82, 83, 84]. What determines the advantages or disadvantages of a certain theory over another is their applicability to the desired nanoscale structure in a specific transport regime. In the field of molecular electronics and quantum dot systems the demand to be able to account for electron interaction effects on the central system as well as to include the impact of the reservoir electrodes on the transport properties narrows this choice. The class of experiments mentioned earlier in chapter 2.4 all show characteristic non-equilibrium transport behavior that is governed mainly by the following parameters: the coupling strength Γ of the nanoscale island to the reservoir electrodes, Coulomb interaction effects between electrons represented by a general parameter U and the temperature T. In general the non-equilibrium transport properties of a mesoscopic system are of course influenced not only by the parameters mentioned above but in manyfold ways. For instance the geometry of the nanoscale island and/or the contacts, the environment, mechanical and optical disturbances may have a strong impact. Such effects are disregarded in the following theoretical discussion but could be additionally included, if needed.

The diagrammatic real time transport theory developed by Schoeller and König et. al. [30, 32] is a powerful tool to describe non-equilibrium transport phenomena in the nanoscale systems we are interested in. The basic idea of this approach is to integrate out all reservoirs degrees of freedom and finally formulate an exact kinetic equation for the reduced density matrix of the quantum dot or molecular system. The objects governing the time evolution of the reduced density matrix contain a series of irreducible diagrams that can be calculated by applying diagrammatic rules (see appendix A) and are identified as transition rates or self-energies. The current and shot noise or even higher correlators are formulated in terms of these transition rates and can thus be obtained by a systematic perturbative expansion in the tunnel coupling Γ. Formulas for the current and shot noise have been derived in [33] and others [58, 85, 86, 87].

In this chapter a compact description of the real time transport theory together with diagrammatic expressions for the current, shot noise and the transition rates is given. It will be shown explicitly how contributions up to second order in the coupling strength Γ (so called co-tunneling contributions) have to be calculated. One of the main results of this thesis is the formulation of a generalized numerical approach that is applicable to real systems such as the ones discussed in chapter 2. Previous work [22, 26, 27] mainly concentrated on simple models such as the single level Anderson model which is reviewed in chapter 5 as an introduction to co-tunneling transport.

3.1 General Hamiltonian

Before we will start to derive the diagrammatic expressions for current and shot noise it is useful to introduce a general Hamiltonian that is able to model our mesoscopic system coupled to metallic leads. We write $H = H_\mathrm{r}+H_\mathrm{D}+H_\mathrm{T} = H_0+H_\mathrm{T}$ as a standard Hamiltonian that consists of three parts corresponding to the reservoirs (r), the dot system (D) and the tunneling (T) between the central system and the reservoirs. The unperturbed isolated system H_0 accounts for non-interacting electrons in the left and right lead (r=R,L) and interacting electrons on the central dot system. We write

$$H_0 = H_r + H_D \qquad \text{with} \tag{3.1}$$

$$H_r = \sum_{k\sigma} \varepsilon_{k\sigma r} a^\dagger_{k\sigma r} a_{k\sigma r} \qquad \mathrm{r} = \mathrm{R}, \mathrm{L} \tag{3.2}$$

and

$$H_\mathrm{D} = \left(\sum_{ij\sigma} \varepsilon_{ij\sigma} c^\dagger_{i\sigma} c_{j\sigma} + \sum_{ijkl\sigma\sigma'} V_{ijkl} c^\dagger_{i\sigma} c^\dagger_{j\sigma'} c_{k\sigma'} c_{l\sigma} \right) . \tag{3.3}$$

Here $a^\dagger_{k\sigma r}$, $(a_{k\sigma r})$ and $c^\dagger_{i\sigma}$, $(c_{i\sigma})$ denote the Fermi creation and annihilation operators that act on states of non-interacting electrons in the reservoirs and interacting electrons on the central dot system, respectively. The energy of the electrons in the reservoirs is given by $\varepsilon_{k\sigma r}$ where k and σ correspond to the electron's wave vector and spin. The electron's energy on the dot system $\varepsilon_{ij\sigma}$ depends on the spin and orbital indices $i, j = 1, .., N$, where N denotes the total number of dot levels. Interaction effects are modeled by the term $V_{ijkl}(i, j, k, l = 1, .., N)$ that describes a general two particle interaction. The above Hamiltonian can be applied to local systems such as single multilevel quantum dots as well as non-local systems such as double quantum dots (DQDs) and delocalized molecular systems. When discussing our results for different systems in chapter 4 and 5 we will specify our parameter choice and the central dot

Hamiltonian, respectively. Now tunneling from one reservoir $r = R, L$ into or out of the central dot system is modeled by

$$H_{\mathrm{T},r} = \sum_{ik\sigma} \left(t_{i\sigma}^{kr} a_{k\sigma r}^{\dagger} c_{i\sigma} + h.c. \right) \tag{3.4}$$

with $H_{\mathrm{T}} = \sum_{r=R,L} H_{\mathrm{T},r}$ and $t_{i\sigma}^{kr}$ being the tunneling matrix elements. These parameters describe the coupling of the dot system to the electronic environment and hence lead to a finite lifetime τ of the dot states that defines an intrinsic level broadening $\Gamma = \hbar/\tau$. The coupling strength to the reservoirs is related to these tunneling amplitudes via

$$\Gamma_r^{i\sigma}(\omega) = \frac{2\pi}{\hbar} \sum_k |t_{i\sigma}^{kr}|^2 \delta(\omega - \varepsilon_{kr}), \tag{3.5}$$

where $\sum_k \delta(\omega - \varepsilon_{kr}) = \rho_e(\omega)$ is the density of states in the reservoirs. In the following we will assume ρ_e to be constant as well as $|t_{i\sigma}^{kr}|^2 = |t_{i\sigma}^{r}|^2$, meaning that the tunneling amplitudes are chosen to be independent of k. This leaves us with an energy independent coupling parameter $\Gamma_r^{i\sigma} = 2\pi |t_{i\sigma}^{r}|^2 \rho_e$ that allows for a left/right asymmetric, level and spin dependent tunnel coupling. In section 3.3 of this chapter we will perform a systematic perturbative expansion in this coupling parameter Γ.

The above model serves to describe transport through a central mesoscopic system and can in principle be applied to a system with arbitrary complex electronic structure. However, especially for molecular systems that are often measured at high temperatures (for instance at room temperature) vibrations and relaxation effects of phonons and photons might become important. We therefore add the Hamiltonian

$$H_{\mathrm{B}} = \sum_q \omega_q d_q^{\dagger} d_q \tag{3.6}$$

with $d_q^{\dagger}, d_q$ being the Bose operators creating (annihilating) a boson with wave vector q. The interaction of the boson bath with the dot structure is modeled by

$$H_{\mathrm{B-D}} = \sum_{q\sigma ij} g_q^{ij} (d_q^{\dagger} + d_q) c_{i\sigma}^{\dagger} c_{j\sigma} \tag{3.7}$$

where g_q^{ij} is the coupling constant. Charge relaxation due to bosons takes place for $i \neq j$ whereas “boson-assisted tunneling ” occurs for $i = j$. In analogy to the fermionic coupling strength Γ we define a bosonic coupling strength

$$\alpha_{ij}(\omega) = \frac{2\pi}{\hbar} \sum_q |g_q^{i,j}|^2 \delta(\omega - \omega_q). \tag{3.8}$$

Again we assume the amplitudes $g_q^{i,j}$ to be independent of q which leads to $\alpha_{ij}(\omega) = 2\pi |g^{ij}|^2 \rho_{\mathrm{b}}(\omega)$ where $\rho_b(w) \sim \omega^3$ is the density of states of the bosonic bath. The exponent accounts for a three dimensional photon field.

When including coupling to a bosonic bath the perturbative term of our Hamiltonian H_T (Eq. 3.4) becomes $\tilde{H}_T = H_T + H_{B-D}$ and the unperturbed part $\tilde{H}_0 = H_0 + H_B$.

3.2 Keldysh contour and diagrammatic approach

To study the electronic transport through our system we apply the non-equilibrium transport theory based on a diagrammatic technique [30, 31]. Non-equilibrium is taken into account by describing the electrons in the reservoirs by Fermi distribution functions with a corresponding chemical potential $\mu_{r=R,L}$. Tunneling is switched on adiabatically at an initial time t_0 which means that for $t \leq t_0$ the tunneling part of the Hamiltonian $H_T(t)$ vanishes. As a consequence the initial density matrix ρ_0 factorizes into parts and thus can be written in the form

$$\rho_0 = \rho_0^{\mathrm{D}} \rho_0^{\mathrm{L}} \rho_0^{\mathrm{R}} \qquad \text{or} \qquad \rho_0 = \rho_0^{\mathrm{D}} \rho_0^{\mathrm{L}} \rho_0^{\mathrm{R}} \rho_0^{\mathrm{B}}. \tag{3.9}$$

The latter expression applies if coupling to a bosonic bath is additionally included. The equilibrium density matrix of the reservoirs reads

$$\rho_0^r = \frac{1}{Z_0^r} e^{-\beta(H_r - \mu_r N_r)}, \tag{3.10}$$

and for the boson bath

$$\rho_0^B = \frac{1}{Z_0^B} e^{-\beta H_B}, \tag{3.11}$$

where $\beta = \frac{1}{k_B T}$ is the inverse temperature and $N_r = \sum_{k\sigma} a^\dagger_{k\sigma r} a_{k\sigma r}$ the number operator in the leads. The normalization factors Z_0^r and Z_0^B are determined by $\mathrm{tr}\rho_0^r = 1$ and $\mathrm{tr}\rho_0^B = 1$ respectively, where the traces are taken over the reservoir and bath degrees of freedom. What remains is the part of the dot electrons in a non-equilibrium situation. Let $\{|\chi\rangle\}$ be an eigenvector basis set which labels the many body dot states and includes all correlations within the central dot system. We may assume the dots initial density matrix to be diagonal in this basis, i.e.

$$\rho_0^D = \sum_\chi p_\chi^{\mathrm{init}} |\chi\rangle\langle\chi|, \qquad \text{where} \sum_\chi p_\chi^{\mathrm{init}} = 1. \tag{3.12}$$

In the stationary limit when the system has forgotten its initial distribution all physical quantities become independent of the choice of the probabilities p_χ^{init}. Since we want to calculate the average current and shot noise we need to know how a quantum statistical expectation value of an arbitrary operator A at time t needs to be calculated. For this procedure it is convenient to express the operator A in the interaction picture with respect to H_0. This implies

$$A(t)_H = \tilde{T}\exp\left(-i \int_t^{t_0} dt' H_{\mathrm{T}}(t')_I\right) A(t)_I T\exp\left(-i \int_{t_0}^{t} dt' H_{\mathrm{T}}(t')_I\right), \tag{3.13}$$

where the indices H (I) refer to the Heisenberg (interaction) picture respectively. The operators T and $\tilde{T}$ denote time and anti-time ordering. Instead of the time integrals we can write Eq. 3.13 as contour integrals $\int_K dt'$ over the so called Keldysh contour (see Fig. 3.1) in which the time t' runs forward from t_0 to t (where $A(t)$ acts) and then backwards in time from t to t_0. The expectation value of the operator $A(t)$ is hence given by

$$\langle A(t)\rangle = \mathrm{tr}\left[\rho_0 T_K \mathrm{exp}\left(-i\int\limits_K dt' H_{\mathrm{T}}(t')_I\right) A(t)_I\right], \tag{3.14}$$

where T_K is the Keldysh time ordering operator that orders a succession of time dependent operators $\langle T_K A_1(t_1)_I A_2(t_2)_I ... A_n(t_n)_I\rangle$ on the Keldysh contour accordingly. Expanding the exponential of Eq. 3.14 with respect to the tunneling Hamiltonian H_T we arrive at

$$\begin{aligned} &\left\langle T_K \mathbf{\Pi}_{i=1}^m A_i(t_i)_I \right\rangle = \\ &tr\left[\rho_0 \sum_{m=0}^{\infty}(-i)^m \int\limits_K dt_1 \int\limits_K^{t_1>t_2>...>t_m} dt_2 ... \int\limits_K dt_m \; T_K\{[H_T(t_1)_I H_T(t_2)_I ... H_T(t_m)_I]\mathbf{\Pi}_{i=1}^m A_i(t_i)\}\right]. \end{aligned} \tag{3.15}$$

Note that the time operator T_K also acts on the operators $A_i(t_i)_I$ and puts them at the correct place between the tunneling Hamiltonians. Operators H_T and A_i are diagrammatically represented by internal (H_T) or external (A_i) vertices as we will see later on in chapter 3.4. Rewriting Eq. 3.14 yields

$$\langle A(t)\rangle = \sum_{\chi} p_{\chi}^{\mathrm{init}} \langle \chi|\Pi A(t)_I|\chi\rangle, \tag{3.16}$$

where

$$\mathbf{\Pi} = \mathrm{tr_L tr_R tr_B}\left[\rho_0^L \rho_0^R \rho_0^B T_K \mathrm{exp}\left(-i\int\limits_K dt' H_{\mathrm{T}}(t')_I\right)\right] \tag{3.17}$$

can be interpreted as the reduced dot system's density propagator describing the time evolution of the system via coupling to the reservoirs without external vertices. More general the non-equilibrium time evolution of the dot density matrix from an initial state χ_1 at t_0 forward to a state χ_1' at time t and then backward from χ_2' to χ_2 is given by the propagator

$$\begin{aligned} &\Pi_{\chi_2,\chi_2'}^{\chi_1,\chi_1'} = \langle\chi_2|\left[\Pi(|\chi_2'\rangle\langle\chi_1'|)(t)_I\right]|\chi_1\rangle = \\ &\mathrm{tr_L tr_R tr_B}\left[\langle\chi_2|\tilde{T}\mathrm{exp}\left(-i\int\limits_t^{t_0} dt' H_{\mathrm{T}}(t')_I\right)|\chi_2'\rangle\langle\chi_1'|T\mathrm{exp}\left(-i\int\limits_{t_0}^{t} dt' H_{\mathrm{T}}(t')_I\right)|\chi_1\rangle\right]. \end{aligned} \tag{3.18}$$

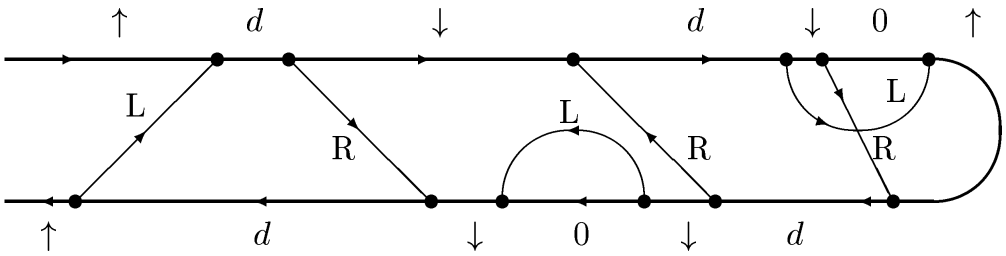

Figure 3.1: *An example for the time evolution of the reduced density matrix. The upper and lower line represent the forward and backward time propagation along the Keldysh contour, respectively. Tunneling lines correspond to the reservoirs* L, R *connecting pairs of vertices. The resulting changes between the dot states are indicated corresponding to a single level Anderson model.*

This equation is visualized in Fig. 3.1. The upper and lower lines describe forward and backward time evolution along the Keldysh contour where tunneling vertices (H_T) change the many-body dot states. Since the Hamiltonian H_0 is bilinear in the lead electron operators Wick's theorem holds for these degrees of freedom and the corresponding operators (e.g. field operators from H_T) can be contracted in pairs. The contractions are given by equilibrium distribution functions and are diagrammatically represented by tunneling lines corresponding to reservoirs $r = R, L$. For electrons in the central quantum dot system Wick's theorem does not hold since the Coulomb interaction is expressed by a quadric term of dot electron operators. Any product of those operators has to be treated explicitly.

3.3 Master equation and stationary probabilities

For the following discussion we will assume the reduced density matrix to be diagonal, i.e. $\chi_1 = \chi_2 = \chi$ and $\chi'_1 = \chi'_2 = \chi'$, which leads to the notation $\Pi_{\chi'\chi} = \Pi^{\chi',\chi}_{\chi',\chi}$. This provides a restriction to the general situation which is however of only minor importance for the systems we will discuss later in chapters IV and V. There are approaches by others that include off-diagonal density matrix elements when appropriate [88, 89]. For instance in a non-local two level system non-diagonal matrix elements are negligible if the inter-dot coupling or hopping parameters are much larger than the tunnel amplitudes to the reservoirs ($t_{ij} >> t^r_i$ with $r = R, L$).

The full propagation $\Pi_{\chi'\chi}(t', t)$ can be decomposed in a sequence of irreducible blocks (diagrams) $W_{\chi'\chi}(t', t)$ containing one ore more tunneling lines. They are associated with transitions from a state χ at time t to χ' at t' and are therefore referred to as transition rates. Parts without tunneling lines correspond to a free propagation and are written as $\mathbf{\Pi}^{(0)} = \mathbf{1}$. This leads to the Dyson equation for the full propagator

$$\mathbf{\Pi}(t',t) = \mathbf{1} + \int_{t}^{t'} dt_2 \int_{t}^{t_2} dt_1\, \mathbf{W}(t_2,t_1)\mathbf{\Pi}(t_1,t) \tag{3.19}$$

where bold face notation indicates matrix representation related to the many body eigenstate basis $\{|\chi\rangle\}$. Note that time ordering in Eq. 3.19 is the other way round compared to the pictorial diagrammatic representation since in matrix representation we read from right to left. In Fig. 3.2 a general transition rate as a perturbative expansion in the reservoir coupling strength Γ is depicted. A block W with one tunneling line describes a first order, sequential tunneling process, a block with two tunneling lines describes a second order, co-tunneling process. In general we can write $\mathbf{W} = \sum_{k=1}^{\infty} \mathbf{W}^{(k)}$ where k denotes the order of the perturbative expansion in Γ. We will specify later in section 3.5.3 and appendix B how to calculate the rates $\mathbf{W}^{(\mathbf{1})}$, $\mathbf{W}^{(\mathbf{2})}$ up to second order in Γ.

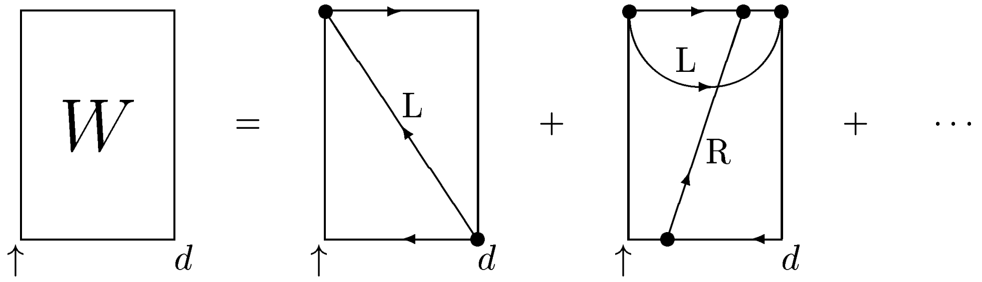

Figure 3.2: *An example of an irreducible self-energy diagram with one, two, etc. tunneling lines, connecting the dot with reservoirs* $r = \mathrm{L,R}$. *The number of tunneling lines gives the order of* Γ *of the perturbative expansion.*

Rewriting the Dyson Equation Eq. 3.19 in its matrix components yields

$$\Pi_{\chi'\chi}(t',t) = 1 + \sum_{\chi''} \int_{t'}^{t} dt_2 \int_{t'}^{t_2} dt_1\, \Pi_{\chi'\chi''}(t',t_1) W_{\chi''\chi}(t_1,t_2). \tag{3.20}$$

Multiplying this equation with the probability $p_{\chi'}(t')$ to be in the state χ' at time t', summing over the states χ' and differentiating with respect to t we obtain

$$\frac{d}{dt} p_{\chi}(t) = \sum_{\chi'} \int_{t_0}^{t} dt' p_{\chi'} W_{\chi'\chi}(t',t), \tag{3.21}$$

where we have used the identity $p_{\chi}(t) = \sum_{\chi'} p_{\chi'}(t')\Pi_{\chi'\chi}(t',t)$ and set $t' = t_0$.

As we apply a finite but static bias the propagator must become stationary in the long-time limit, i.e. for time differences $t'-t$ larger than the relaxation time of the system. We can thus write

$$\lim_{t_0\to -\infty}\mathbf{\Pi}(t'-t_0)=\mathbf{p}^{\mathrm{st}}\otimes\mathbf{e}^T, \tag{3.22}$$

where $\mathbf{e}^T=(1,..,1)$, and $\mathbf{p}^{\mathrm{st}}$ is the vector of the stationary probabilities of the dot, independent of t'. Also the transition rates $W_{\chi'\chi}(t',t)$ in Eq. 3.21 depend only on the time difference $t'-t$, i.e. $W_{\chi'\chi}(t'-t)$. To study the time evolution of the stationary probabilities p^{st} we set Eq. 3.21 to zero and use the fact that an arbitrary initial state $\mathbf{p}^{\mathrm{init}}=\lim_{t_0\to-\infty}\mathbf{p}(t_0)$ will develop always into the same stationary state $\lim_{t_0\to-\infty}\mathbf{\Pi}(0,t_0)\mathbf{p}(t_0)=\mathbf{p}^{\mathrm{st}}$. Performing a Laplace transformation on the time dependent transition rates in the form of $\mathbf{W}(z)=\hbar\int_{-\infty}^{0}dt\,e^{zt}\mathbf{W}(0,t)$ with the definition $\mathbf{W}=\mathbf{W}(z)|_{z=0^+}$ and using the sum rule $\mathbf{e}^T\mathbf{W}=\mathbf{0}$ (see diagrammatic rules in appendix A) we find the stationary master equation

$$\mathbf{W}\mathbf{p}^{\mathrm{st}}=\mathbf{0} \tag{3.23}$$

However $\mathbf{W}$ has a zero eigenvalue and can thus not be inverted. Using the normalization condition $\mathbf{e}^T\mathbf{p}^{\mathrm{st}}=1$ we obtain the stationary probabilities $\mathbf{p}^{\mathrm{st}}$ by solving

$$\tilde{\mathbf{W}}\mathbf{p}^{\mathrm{st}}=\mathbf{v}, \tag{3.24}$$

where $\tilde{\mathbf{W}}$ is identical to $\mathbf{W}$ but with one row χ_0 being replaced by $(\Gamma,..,\Gamma)$ and $\mathbf{v}$ defined by $v_\chi=\Gamma\delta_{\chi\chi_0}$.

For a well-defined perturbative expansion in powers k of the coupling strength Γ we write $\mathbf{W}=\sum_{k=1}^{\infty}\mathbf{W}^{(k)}$, $\tilde{\mathbf{W}}=\sum_{k=1}^{\infty}\tilde{\mathbf{W}}^{(k)}$, and $\mathbf{p}^{\mathrm{st}}=\sum_{k=0}^{\infty}\mathbf{p}^{\mathrm{st}(k)}$. The stationary master equation (Eq. 3.23) has to be fulfilled in every order k of our perturbation theory which leads to

$$\mathbf{p}^{\mathrm{st}(0)}=(\tilde{\mathbf{W}}^{(1)})^{-1}\mathbf{v}, \tag{3.25}$$

for the zeroth-order stationary probabilities and to

$$\mathbf{p}^{\mathrm{st}(k)}=-\left(\tilde{\mathbf{W}}^{(1)}\right)^{-1}\sum_{m=0}^{k-1}\tilde{\mathbf{W}}^{(k-m+1)}\mathbf{p}^{\mathrm{st}(m)}\,, \tag{3.26}$$

for the higher order $k=1,2,\ldots$ terms. The irreducible diagrams $\mathbf{W}^{(k)}$ can be directly calculated using the diagrammatic rules (see appendix A,B and chapter 3.5.).

3.4 Diagrammatic expressions

3.4.1 Current

We are interested in the current flowing through the left and right barrier ($r = L, R$) of our system. The current is an operator defined by the change of particle (electron) number

$$\hat{I}_r(t) = -e\frac{d}{dt}N_r(t), \tag{3.27}$$

where $N_r(t)$ denotes the time dependent number operator of the electrons in the lead r. In the Heisenberg picture the Heisenberg equation governs the time evolution. Thus we write $\frac{d}{dt}N_r(t)_H = i[H, N_r](t)_H = i[H_T, N_r](t)_H$, which leads to

$$\hat{I}_r(t) = -i(e/\hbar)\sum_{ik\sigma}\left(t^{kr}_{i\sigma}(a^\dagger_{k\sigma r}c_{i\sigma})(t) - h.c.\right). \tag{3.28}$$

This current operator presents a possible choice for an external vertex A as described in the previous chapters 3.2 and 3.3.. It is convenient to choose a symmetrized notation of the current operator, namely $\hat{I} = (\hat{I}_{\mathrm{R}} - \hat{I}_{\mathrm{L}})/2$ which is useful for a compact description of the shot noise. Because of the continuity equation, $\hat{I} = \hat{I}_{\mathrm{R}} = -\hat{I}_{\mathrm{L}}$.

To calculate the expectation value of the current we follow the procedure described in section 3.2. The current operator Eq. 3.28 has a very similar structure compared to the tunneling operator H_T in Eq. 3.4. For a diagrammatic representation of the current we therefore introduce a diagram $\mathbf{W}^I(t,t')$ in which one internal tunneling vertex due to $\hat{H}_{T,R}$ or $\hat{H}_{T,L}$ at any time between t' and t is replaced by an external one ($\hat{I}\frac{\hbar}{e}$). This leads to overall pre-factors and signs which we specify in appendix B. The current expectation value can hence be written as

$$I(t) = \lim_{t_0\to-\infty}\left[\frac{e}{2\hbar}\int_{t_0}^{t} dt'\mathbf{e}^T\hbar\mathbf{W}^I(t,t')\mathbf{\Pi}(t',t_0)\mathbf{p}(t_0)\right] \tag{3.29}$$

For $t_0 \to -\infty$ the propagator in Eq. 3.29 leads to time-independent stationary states such that the only remaining time dependent objects are the transition rates $\mathbf{W}^I(t,t')$, which can be Laplace transformed. We thus obtain

$$I = \frac{e}{2\hbar}\mathbf{e}^T\mathbf{W}^I\mathbf{p}^{\mathrm{st}} \tag{3.30}$$

where we have set $t = 0$ without loss of generality and used the normalization condition $\mathbf{e}^T\mathbf{p}^{\mathrm{init}} = 1$. Expanding the current up to infinite order $k = 1, 2, ...$ in the coupling strength Γ we obtain

$$I^{(k)} = \frac{e}{2\hbar}\mathbf{e}^T\sum_{m=0}^{k-1}\mathbf{W}^{I(k-m)}\mathbf{p}^{\mathrm{st}(m)} \tag{3.31}$$

where the total current is given by $I = \sum_{k=1}^{\infty} I^{(k)}$. Note that the stationary probabilities are calculated out of the irreducible diagrams $\mathbf{W}^k$ via the master equation Eq. 3.23 and thus depend on the transition rates.

3.4.2 Zero frequency shot noise

The shot noise is defined as the Fourier transform function of the current. In the zero frequency limit we write

$$S = \int_{-\infty}^{\infty} dt \langle \delta \hat{I}(t) \delta \hat{I}(0) + \delta \hat{I}(0) \delta \hat{I}(t) \rangle, \tag{3.32}$$

with $\delta \hat{I}(t) = \hat{I}(t) - \langle \hat{I} \rangle$. It involves expectation values of two current operators at different times. They can either appear in one single irreducible diagram denoted by $\mathbf{W}^{II}$ or in two different diagrams of type $\mathbf{W}^I$. In analogy to $\mathbf{W}^I$ the diagram $\mathbf{W}^{II}(0, t')$ is defined by replacing two internal vertices by external ones. The two external vertices can sit at any time between t' and 0.

Using the result of [33] we write the total shot noise in energy representation as

$$S = \frac{e^2}{\hbar} \mathbf{e}^T \left[\mathbf{W}^{II} + \mathbf{W}^I (\mathbf{P} \mathbf{W}^I + \mathbf{p}^{\mathrm{st}} \otimes \mathbf{e}^T \partial \mathbf{W}^I) \right] \mathbf{p}^{\mathrm{st}}. \tag{3.33}$$

Here the object $\mathbf{P}$ is defined by the expression

$$\mathbf{P}(t''', t_0) = \int_{t_0}^{t'''} dt'' \frac{1}{\hbar} [\mathbf{\Pi}(t''', t'') - \mathbf{\Pi}(t''', t_0)] \tag{3.34}$$

and is recognized as a Laplace transform in the limit $t_0 \to -\infty$ and $t''' = 0$. The object $\partial \mathbf{W}^I$ is related to the derivative of the Laplace transform $\mathbf{W}^I(z) = \hbar \int_{-\infty}^{0} dt e^{zt} \mathbf{W}^I(0, t)$ with $\partial \mathbf{W}^I = (\frac{\partial \mathbf{W}^I(z)}{\partial z}|_{z=0^+})$. $\mathbf{P}$ can be called the “decaying” propagator since the stationary part of the propagator is subtracted. Except for the object $\mathbf{P}$ all other terms can be calculated out of the transition rates $\mathbf{W}$ which are obtained diagrammatically (see section 3.5). Using the Dyson-Equation (Eq. 3.19) for the propagator $\mathbf{\Pi}(0, t_0)$ and after some manipulation [33] the object $\mathbf{P}$ can be determined from the equation

$$\mathbf{p}^{\mathrm{st}} \otimes \mathbf{e}^T = \mathbf{1} + \mathbf{W} \mathbf{P} + \partial \mathbf{W} \mathbf{p}^{\mathrm{st}} \otimes \mathbf{e}^T \qquad \text{with } \mathbf{e}^T \mathbf{P} = \mathbf{0}. \tag{3.35}$$

For completeness we want to mention that the above equations for the shot noise (Eq. 3.33) and the object $\mathbf{P}$ (Eq. 3.35) require the transition rates to decay fast enough such that $\lim_{t \to -\infty} (t^2 \mathbf{W}(0, t)) = \mathbf{0}$.

3.5 A computational approach

The aim to describe non-equilibrium transport through a molecular nanostructure in principle requires three main tasks:

- The diagonalization of the Hamiltonian H_D Eq. 3.3 in order to obtain the eigen energy spectrum of the central system,
- a choice of the perturbative order k up to which transport is considered (e.g. sequential or co-tunneling transport depending on the coupling situation) together with an appropriate perturbation scheme that is valid in the considered transport regime,
- the calculation of the transition rates (irreducible diagrams) $\mathbf{W}^{(k)}$ up to the k^{th}-order
- solving Eq. 3.25, Eq. 3.26 first to obtain the stationary probabilities p^{st}, inserting results into Eq. 3.35 to obtain the propagator P and finally evaluate Eq. 3.30, Eq. 3.33.

This chapter comprises the ingredients mentioned above. We will start by characterizing the molecular or quantum dot system in isolation from the leads in order to determine its energy spectrum. The current and shot noise are evaluated explicitly up to second order in the coupling strength Γ together with an analysis of the relevant perturbative scheme for the stationary probabilities and the "decaying" propagator. Finally as our main result we present a systematic approach to determine first and second order transition rates for an arbitrary complex electronic structure of the central system.

3.5.1 Diagonalization of the Hamiltonian

The molecule or quantum dot in isolation constitutes a finite quantum system with discrete energy levels. The molecular states are either occupied or unoccupied and have a mean distance or level spacing of $\Delta\varepsilon$. The HOMO is defined as the highest occupied molecular orbital meaning that all lower lying molecular orbitals (MO) are filled with electrons. The unoccupied levels start with the lowest unoccupied MO (LUMO) which defines a characteristic gap to the HOMO. In the case of a quantum dot or a chain of coupled quantum dots basically two energy scales are relevant. First the “sequential energy gap” that is defined by the energy difference between the ground state and the first excited state in the adjacent charge sector and second the “inelastic co-tunneling” energy defined by the energy distance between the first excited state and the ground state in the same charge sector. In some cases the latter can be related to the HOMO-LUMO gap described above. Now referring to our dot Hamiltonian Eq. 3.3

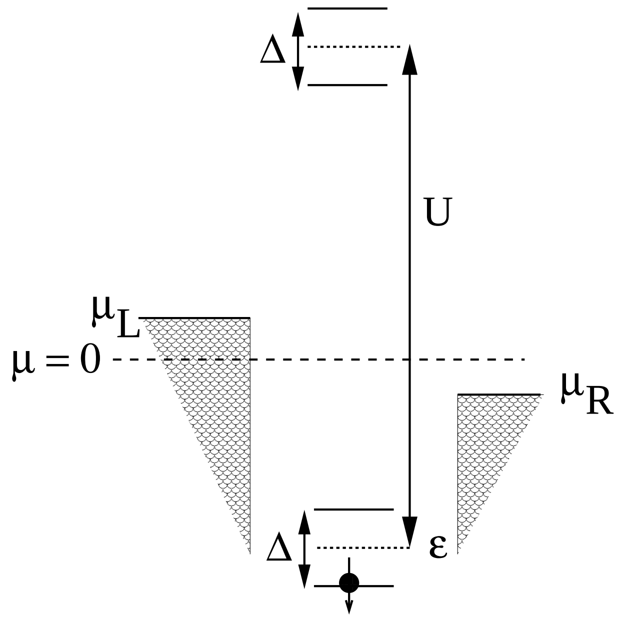

Figure 3.3: *Sketch of the energy spectrum of a single level Anderson model with spin splitting* Δ*. For the upper, doubly occupied states the energy cost due to the Coulomb repulsion* U *has to be paid.*

in the second quantization we write a general many body state in its occupation number representation as $c^\dagger_{i,\sigma}c^\dagger_{j,\sigma'}...|0\rangle$, where $|0\rangle$ is the empty state. The total Hamilton matrix including electron interaction terms U and hopping t between non-local orbitals can be diagonalized in the subspace of a fixed total charge number using standard linear algebra (lapack) routines. Note that in the case of degeneracies we additionally have to diagonalize in the spin subspace to obtain eigenstates of total spin. In Fig. 3.3 we depict the obtained energy spectrum after diagonalization of a single level Anderson model with a finite spin splitting. For a double quantum dot with two single levels the resulting eigenstates and eigenvalues can be found for instance in [90].

3.5.2 Perturbation schemes

As a starting point for our perturbative expansion in the tunnel coupling Γ we use the general expressions Eq. 3.30 for the current and Eq. 3.33 for the zero frequency shot noise. All irreducible diagrams $\mathbf{W}, \mathbf{W^I}, \mathbf{W^{II}}$ and $\partial\mathbf{W}, \partial\mathbf{W}^I$ are expanded in a power series $\mathbf{W} = \sum_{k=1}^{\infty}\mathbf{W}^{(k)}$ etc., where (k) indicates the order in Γ and corresponds to the number of tunneling lines in the diagram. As a consequence all transition rate diagrams start in first order in Γ since they contain at least one tunneling line. In the

case of the stationary probabilities, $\mathbf{p}^{st}$ from Eq. 3.23, the expansion series has to start in zeroth order in Γ. Analogously the propagator, $\mathbf{P}$ from Eq. 3.35, starts in $\Gamma^{(-1)}$. Thus we are left with the following set of equations that govern the non-equilibrium transport properties of our system up to second order in Γ:
The expression for the current in first order reads

$$I^{(1)} = \frac{e}{2\hbar}\mathbf{e}^T\mathbf{W}^{I(1)}\mathbf{p}^{\mathrm{st}(0)}, \tag{3.36}$$

and in second order

$$I^{(2)} = \frac{e}{2\hbar}\mathbf{e}^T(\mathbf{W}^{I(2)}\mathbf{p}^{\mathrm{st}(0)} + \mathbf{W}^{I(1)}\mathbf{p}^{\mathrm{st}(1)}). \tag{3.37}$$

The shot noise is given by

$$S^{(1)} = \frac{e^2}{\hbar}\mathbf{e}^T\left(\mathbf{W}^{II(1)} + \mathbf{W}^{I(1)}\mathbf{P}^{(-1)}\mathbf{W}^{I(1)}\right)\mathbf{p}^{\mathrm{st}(0)} \tag{3.38}$$

and

$$\begin{aligned} S^{(2)} = \frac{e^2}{\hbar}\mathbf{e}^T(&\mathbf{W}^{II(2)}\mathbf{p}^{\mathrm{st}(0)} + \mathbf{W}^{II(1)}\mathbf{p}^{\mathrm{st}(1)} \\ &+\mathbf{W}^{I(2)}\mathbf{P}^{(-1)}\mathbf{W}^{I(1)}\mathbf{p}^{\mathrm{st}(0)} \\ &+\mathbf{W}^{I(1)}\mathbf{P}^{(-1)}\mathbf{W}^{I(2)}\mathbf{p}^{\mathrm{st}(0)} \\ &+\mathbf{W}^{I(1)}\mathbf{P}^{(0)}\mathbf{W}^{I(1)}\mathbf{p}^{\mathrm{st}(0)} \\ &+\mathbf{W}^{I(1)}\mathbf{P}^{(-1)}\mathbf{W}^{I(1)}\mathbf{p}^{\mathrm{st}(1)} \\ &+\mathbf{W}^{I(1)}(\mathbf{p}^{\mathrm{st}(0)} \otimes \mathbf{e}^T)\partial\mathbf{W}^{I(1)}\mathbf{p}^{\mathrm{st}(0)}), \end{aligned} \tag{3.39}$$

respectively. From the master equation Eq. 3.23 we obtain in lowest order in Γ

$$\mathbf{W}^{(1)}\mathbf{p}^{st(0)} = 0, \tag{3.40}$$

from which we determine $p^{st(0)}$. Next to lowest order we have

$$\mathbf{W}^{(2)}\mathbf{p}^{st(0)} + \mathbf{W}^{(1)}\mathbf{p}^{st(1)} = 0, \tag{3.41}$$

which is solved for $p^{st(1)}$. The normalization condition yields $\mathbf{e}^T\mathbf{p}^{st(0)} = 1$ and $\mathbf{e}^T\mathbf{p}^{st(1)} = 0$. Similarly we write for the "decaying" propagator $\mathbf{P}$

$$\mathbf{W}^{(1)}\mathbf{P}^{(-1)} = (\mathbf{p}^{\mathrm{st}(0)} \otimes \mathbf{e}^T) - \mathbf{1}, \tag{3.42}$$

$$\mathbf{W}^{(2)}\mathbf{P}^{(-1)} + \mathbf{W}^{(1)}\mathbf{P}^{(0)} = (\mathbf{p}^{\mathrm{st}(1)} - \partial\mathbf{W}^{(1)}\mathbf{p}^{\mathrm{st}(0)}) \otimes \mathbf{e}^T, \tag{3.43}$$

with $\mathbf{e}^T\mathbf{P}^{(-1)} = \mathbf{0}$ and $\mathbf{e}^T\mathbf{P}^{(0)} = \mathbf{0}$ which follows from the definition of $\mathbf{P}$ and the Dyson equation Eq. 3.19.

As has been mentioned before $\mathbf{W}$ cannot be inverted and thus we need to replace $\mathbf{W}^{(1)}$ by $\tilde{\mathbf{W}}^{(1)}$ (which has been defined earlier in Eq. 3.24) into the above set of equations (Eq. 3.40)-(Eq. 3.43). In the case of the stationary probabilities this leads to Eq. 3.25 in lowest order and to

$$\mathbf{p}^{st(1)} = (\tilde{\mathbf{W}}^{(1)})^{-1} \left[\tilde{\mathbf{W}}^{(2)}\mathbf{p}^{st(0)}\right] \tag{3.44}$$

in the next to lowest order in Γ. Here $\tilde{\mathbf{W}}^{(2)}$ is identical to the second order rates $\mathbf{W}^{(2)}$ but with one row χ_0 being replaced by (0,..,0). For the object $\mathbf{P}$ this implies

$$\mathbf{P}^{(-1)} = (\tilde{\mathbf{W}}^{(1)})^{-1} \left[\mathbf{p}^{st(0)} \otimes \mathbf{e}^T - \mathbf{1}\right] \tag{3.45}$$

$$\mathbf{P}^{(0)} = (\tilde{\mathbf{W}}^{(1)})^{-1} \left[\tilde{\mathbf{1}}(\mathbf{p}^{\mathrm{st}(1)} \otimes \mathbf{e}^T - \partial\mathbf{W}^{(1)}\mathbf{p}^{\mathrm{st}(0)} \otimes \mathbf{e}^T) - \tilde{\mathbf{W}}^{(2)}\mathbf{P}^{(-1)}\right] \tag{3.46}$$

correspondingly.

In fact one has to be careful when solving the set of equations (Eq. 3.40 - Eq. 3.43). As long as sequential transport processes are non-negligible the above scheme holds and can be safely used without running into computational problems. We will refer to this scheme in the following as the **standard scheme**. In the deep Coulomb blockade when sequential transport is exponentially suppressed the standard scheme is not applicable anymore and a different perturbation scheme has to be used. In [91, 92] a *deep Coulomb scheme* is described that works particularly well in the deep Coulomb blockade but does not hold when sequential processes become applicable. However, it is most desirable to have a perturbative scheme which is able to describe transport from the Coulomb blockade up to sequential transport through excited states in the large bias regime. This is achieved by means of the **crossover scheme** which smoothly interpolates between the *standard scheme* and *deep Coulomb scheme*. In this regime the first order exponentially suppressed transition rates are of the same order of magnitude as the co-tunneling rates. As a consequence a “order by order” expansion of current and shot noise in powers of Γ is not useful anymore. Instead we sum up the first and second order transition rates to give the matrices $W^{(tot)} = W^{(1)} + W^{(2)}$, $W^{I(tot)} = W^{I(1)} + W^{I(2)}$ and $W^{II(tot)} = W^{II(1)} + W^{II(2)}$. Similarly we define the sum of the probabilities $p^{st(tot)} = p^{\mathrm{st}(0)} + p^{\mathrm{st}(1)}$ and the object $P^{(\mathrm{tot})} = P^{(-1)} + P^{(0)}$. Inserting these combined first and second order terms into equations (Eq. 3.23), (Eq. 3.35), (Eq. 3.30) and (Eq. 3.33) then constitutes the crossover regime. Note that in the discussion of co-tunneling transport in chapter 5 we will mainly use the crossover scheme since it is the only scheme (of the three mentioned above) that allows to resolve both the inelastic co-tunneling energy as well as the co-tunneling assisted sequential energy scale at the same time.

3.5.3 Transition rates

In the following a detailed description of our implementation scheme for the second order diagrams is given. As stated in the previous chapter the computation of the transition rates $\mathbf{W}^{(2)}, \mathbf{W}^{I(2)}$ and $\mathbf{W}^{II(2)}$ is the most complicated and tedious part when calculating co-tunneling transport. All other quantities are obtained from them. The computation of the first order transition rates is much easier and has been the subject of many earlier works. They can be obtained by a golden rule approach as well as within the diagrammatic technique. We use the diagrammatic formulation developed in [26] and refer the reader to appendix B, in which the expressions for the first order transition rates $\mathbf{W}^{(1)}$, current rates $\mathbf{W}^{I(1)}$ and shot noise rates $\mathbf{W}^{II(1)}$ are given.

Second order rates

In total there are 128 diagrams including the direction of the tunneling lines and the two reservoirs labels $r = R, L$. However, to calculate all second order diagrams in a compact way we only consider all possible topologically different diagrams. By "topologically different" we mean (disregarding the direction of the tunneling lines and the reservoirs indices for the moment) all diagrams that can not be transformed into each other by moving the vertices on their time branch. We obtain 32 topologically different diagrams resulting from $2k = 4$ (internal) vertices. Using the so called "mirror rule" [37, 93], this number can be further reduced to 16 diagrams which are displayed in Figs. 3.4 and 3.5.

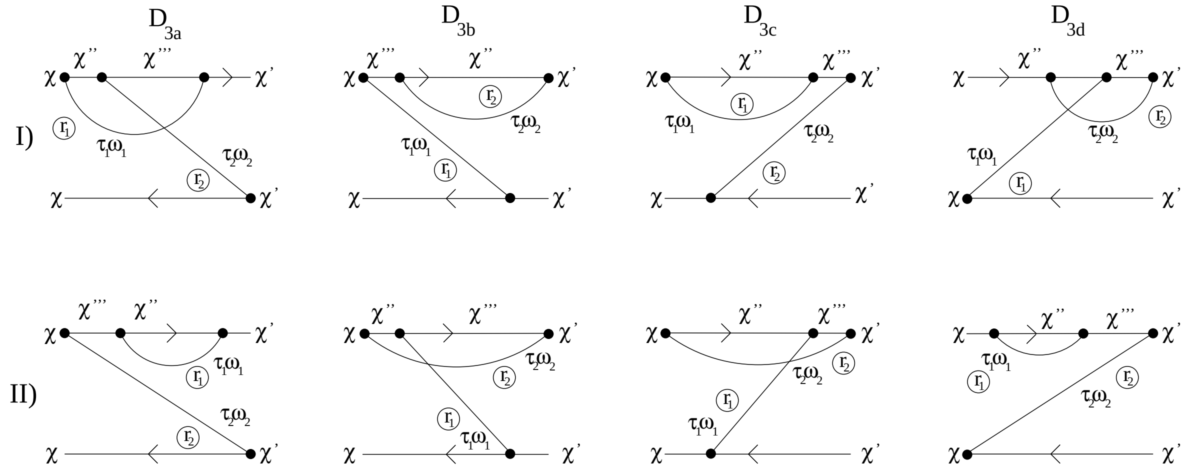

Figure 3.4: *Eight different diagrams with three vertices on the upper time branch and one vertex on the lower time branch. The rightmost vertex is always connected to the reservoir r_2 with a corresponding sign $\tau_2 = +(-)$ and energy ω_2. The diagrams are calculated using the rules specified in appendix A.*

Now collecting all diagrammatic contributions we can write the second order transition rates matrix $W^{(2)}$ in its matrix components

$$W^{(2)}_{\tilde{\chi}\chi} = -i \sum_{\chi',\chi'',\chi'''} \sum_{\{j_i,l_i,\sigma_i,r_i\}} \left[\delta_{\tilde{\chi}\chi'} \mathrm{D}^{\chi\chi'}_{3X} + \delta_{\tilde{\chi}\chi} \mathrm{D}^{\chi\chi}_{4X,2bI,2cII} + \delta_{\tilde{\chi}\chi''} \mathrm{D}^{\chi\chi''}_{2aI} + \delta_{\tilde{\chi}\chi'''} \mathrm{D}^{\chi\chi'''}_{2aII,2bII,2cI}\right], \tag{3.47}$$

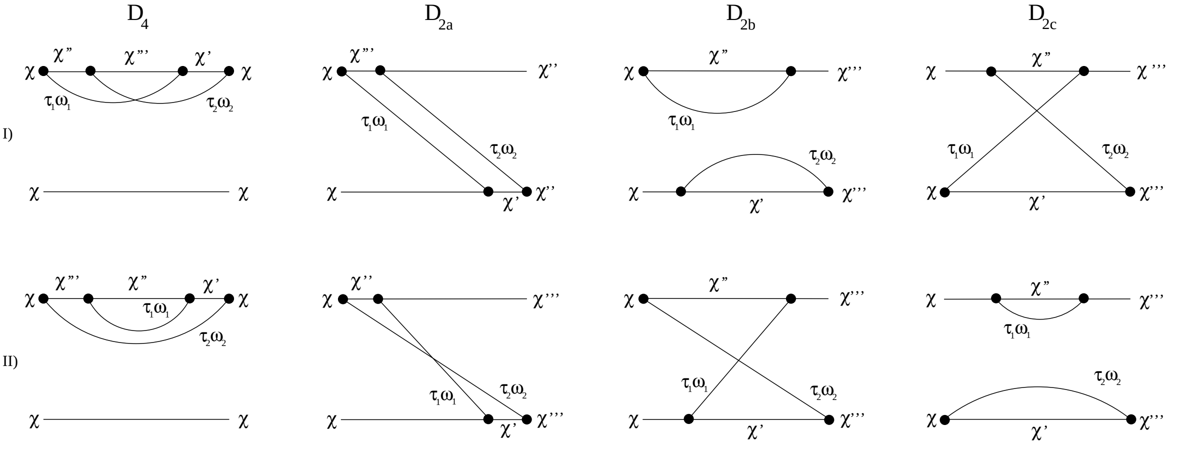

Figure 3.5: *Two diagrams* D$_4$ *with four vertices on the upper time branch and no vertices on the lower time branch. Six diagrams with D_{2X} with two vertices on the upper and lower time branch. These diagrams can be obtained from the eight diagrams in Fig. 3.4 with an additional relative sign.*

where $i = 1, 2$ and $\{j_i\} = \{+, -\}$ corresponds to creation (annihilation) operators respectively and $\{l_i\}$=$\{$(1,..,N)$\}$ to the orbital (local or non-local) levels with N being the total number of orbitals, $\{\sigma_i\} = \{\text{up}, \text{down}\}$ denotes the spin of an electron and $\{r_i\} = \{R, L\}$ the reservoirs. The states labeled by χ, χ',.. etc. are the eigenstates of the central dot system. Note that the index I, II has nothing to do with external (current) vertices but is just a label for different diagrams. The index X comprises all diagrams of the corresponding type, for instance $D_{4X} = D_{4I} + D_{4II}$. Hence the first term of Eq. 3.47 consists of eight diagrams, the second of four, the third is only one diagram and the forth term comprises three diagrams. The factor $(-i)$ originates from the fact that the diagrammatic rules which we use have been formulated for the self energies Σ in [37] and relate to the transition rates via $\Sigma_{\chi'\chi} = i\mathbf{W}_{\chi\chi'}$.

The class of diagrams D$_{3\text{X}}$ depicted in Fig. 3.4 is calculated by using the diagrammatic rules in energy space as defined in appendix A. All diagrams D$_{4\text{X}}$ and D$_{2\text{X}}$ in Fig. 3.5 can be obtained from the D$_{3\text{X}}$ diagrams since moving the rightmost vertex to the upper or lower time branch respectively yields again a diagram of type D$_{3\text{X}}$ but with an overall minus sign. Each of the diagrams in Fig. 3.4 can be written in the form

$$D_X = S \cdot \tilde{D}_{I,II} \cdot ME, \tag{3.48}$$

where S is an overall sign that comprises all prefactors assigned according to the diagrammatic rules and the function $\tilde{D}_{I,II}$ corresponds to a double integral of the type

$$2i\text{Im} \int_{-\infty}^{\infty} \int_{-\infty}^{\infty} d\omega_1 d\omega_2 \frac{\gamma^{p_1}_{r_1,l_1,\sigma_1}(\omega_1)\gamma^{p_2}_{r_2,l_2,\sigma_2}(\omega_2)}{(\tau_1\omega_1 + \Delta_1 + i\eta)(\tau_1\omega_1 + \tau_2\omega_2 + \Delta_{12} + i\eta)(\tau_2\omega_2 + \Delta_2 + i\eta)}, \tag{3.49}$$

where $\Delta_1, \Delta_{12}, \Delta_2$ denote energies that are composed of the eigenenergies ε_χ of the dot system, γ is related to the Fermi function as defined in appendices A and B and η denotes a convergence factor which is taken in the limit $\eta = 0^+$ in the end. A mathematical solution of Eq. 3.49 is given in appendix C. The term with the matrix element (ME) accounts for a series of 4 vertices at which an electron is either created ($j = +$) or annihilated ($j = -$).

Let us consider the diagram D_{3aI} as a specific example. The matrix element has the form

$$ME = \langle\chi|c^{-j_2}_{l_2,\sigma_2,r_2}|\chi'\rangle\langle\chi'|c^{-j_1}_{l_1,\sigma_1,r_1}|\chi'''\rangle\langle\chi'''|c^{j_2}_{l_2,\sigma_2,r_2}|\chi''\rangle\langle\chi''|c^{j_1}_{l_1,\sigma_1,r_1}|\chi\rangle$$

and can be obtained within a numerical computation using an operator algebra. The prefactor S from Eq. 3.48 is determined by the diagrammatic rules (rule 5, appendix A) which yields in this case a minus sign for the vertex on the backward propagator and another minus sign due to one crossing of tunneling lines. Thus we arrive at a total prefactor of $S = 1$. Furthermore we have to evaluate the double integral in Eq. 3.49, $D_{I,II}(\Delta_1, \Delta_{12}, \Delta_2, \tau_1, \tau_2, p_1, p_2, r_1, r_2)$, which is dependent on the energies Δ_i, the signs $\tau_i = \pm 1, p_i = \pm 1$ arising due to the creation/annihilation operators (c^j with $j = \pm 1$) in the matrix element ME and the reservoir indices r_i. The energies assigned according to rule 2, appendix A are $\Delta_1 = \varepsilon_\chi - \varepsilon''_\chi$, $\Delta_{12} = \varepsilon_\chi - \varepsilon'''_\chi$, $\Delta_2 = \varepsilon_\chi - \varepsilon'_\chi$, respectively and the signs read $\tau_i = p_i = j_i$. These are all the ingredients we need in order to calculate the diagram $D^{\chi,\chi'}_{3aI}(\chi'', \chi''')$ for specific inner states χ'',χ'''. It gives a contribution to the transition rate $W^{(2)}_{\chi'\chi}$. Table 3.1 summarizes the expressions for the other diagrams of Fig. 3.4 below.

As mentioned earlier in this section, the diagrams depicted in Fig. 3.5 can be obtained from the D_{3X} diagrams of Fig. 3.4. Hence we can write

$$\begin{aligned}
D^{\chi\chi}_{4I}(\chi'', \chi''', \chi') &= -D^{\chi\chi'}_{3aI}(\chi'', \chi''') & D^{\chi\chi'''}_{2bI}(\chi'', \chi', \chi''') &= -D^{\chi\chi'}_{3cI}(\chi'', \chi''') \\
D^{\chi\chi}_{4II}(\chi''', \chi'', \chi') &= -D^{\chi\chi'}_{3aII}(\chi'', \chi''') & D^{\chi\chi'''}_{2bII}(\chi'', \chi') &= -D^{\chi\chi'}_{3cII}(\chi'', \chi''') \\
D^{\chi\chi''}_{2aI}(\chi', \chi''') &= -D^{\chi\chi'}_{3bI}(\chi'', \chi''') & D^{\chi\chi'''}_{2cI}(\chi'', \chi') &= -D^{\chi\chi'}_{3dI}(\chi'', \chi''') \\
D^{\chi\chi'''}_{2aII}(\chi'', \chi') &= -D^{\chi\chi'}_{3bII}(\chi'', \chi''') & D^{\chi\chi'''}_{2cII}(\chi'', \chi', \chi''') &= -D^{\chi\chi'}_{3dII}(\chi'', \chi''').
\end{aligned}$$

The expressions are summed over all inner states χ', χ'', χ''', respectively. As a last task, we need to economically implement the sums over the eigenstates and internal parameters $(j_1, j_2, l_1, l_2, \sigma_1, \sigma_2, r_1, r_2)$. Instead of defining them in straight forward loops that run over all possibilities which would mean an extremely high computational effort for large systems (such as molecules), we only consider physically possible combinations. This implies for the eigenstates that their charge number is fixed within a single factor of the matrix element. To illustrate this consider the matrix element $\langle\chi|c^{-j_2}_{l_2,\sigma_2,r_2}|\chi'\rangle$.

If the total charge of the eigenstate $|\chi\rangle$ is fixed to N then it follows that $\chi' \in N+1$ or $\chi' \in N$, respectively. Otherwise the total matrix element is zero and thus the corresponding diagram contribution. Following the above procedure we finally obtain all second order rates $\mathbf{W}^{(2)}$ from which we can determine the co-tunneling contributions to the probabilities $p^{st(1)}$ and to the propagator $P^{(0)}$. For the current and noise we still have to calculate the current and shot noise rates $\mathbf{W}^{I(2)}$ and $\mathbf{W}^{II(2)}$. As stated in the additional diagrammatic rules for external vertices (see appendix A) we have to multiply each diagram of Fig. 3.4 with a total prefactor F consisting of factors $\frac{1}{2}$ and signs. The rates $\mathbf{W}^{I(2)}$, $\mathbf{W}^{II(2)}$ together with the total prefactors F are defined in appendix C.3 respectively. We still have to calcultate the derivative rates $\partial\mathbf{W}^{(1)}$ and $\partial\mathbf{W}^{I(1)}$. The first is needed to obtain the propagator P (Eq. 3.46) whereas the latter shows up in the shot noise expression (Eq. 3.33) in second order. Both derivative rates have a very similar mathematical structure as the second order transition rates. In appendix C.2 we have given their explicit expressions.

We have formulated a computational approach that is able to construct all diagrams up to a second order perturbation theory in the coupling Γ. The eigenstates denoted by $\{|\chi\rangle\}$ apply to a general electronic spectrum that has to be calculated in advance.

D_{3X}	S	$\tilde{D}_I(\Delta_1, \Delta_{12}, \Delta_2, \tau_1, \tau_2, p_1, p_2)$ $\tilde{D}_{II}(\Delta_2', \Delta_{12}, \Delta_2, \tau_1, \tau_2, p_1, p_2)$	Matrix-elements (ME)
$D_{3aI}^{\chi,\chi'}(\chi'', \chi''')$	1	$\tilde{D}_I((\varepsilon_\chi - \varepsilon_{\chi''}), (\varepsilon_\chi - \varepsilon_{\chi'''}), (\varepsilon_\chi - \varepsilon_{\chi'}), j_1, j_2, j_1, j_2, r_1, r_2)$	$\langle\chi\|c_{l_2,\sigma_2,r_2}^{-j_2}\|\chi'\rangle\langle\chi'\|c_{l_1,\sigma_1,r_1}^{-j_1}\|\chi'''\rangle\langle\chi'''\|c_{l_2,\sigma_2,r_2}^{j_2}\|\chi''\rangle\langle\chi''\|c_{l_1,\sigma_1,r_1}^{j_1}\|\chi\rangle$
$D_{3aII}^{\chi,\chi'}(\chi'', \chi''')$	-1	$\tilde{D}_{II}((\varepsilon_\chi - \varepsilon_{\chi'}), (\varepsilon_\chi - \varepsilon_{\chi''}), (\varepsilon_\chi - \varepsilon_{\chi'}), j_1, j_2, j_1, j_2, r_1, r_2)$	$\langle\chi\|c_{l_2,\sigma_2,r_2}^{-j_2}\|\chi'\rangle\langle\chi'\|c_{l_1,\sigma_1,r_1}^{-j_1}\|\chi''\rangle\langle\chi''\|c_{l_1,\sigma_1,r_1}^{j_1}\|\chi'''\rangle\langle\chi'''\|c_{l_2,\sigma_2,r_2}^{j_2}\|\chi\rangle$
$D_{3bI}^{\chi,\chi'}(\chi'', \chi''')$	-1	$\tilde{D}_I((\varepsilon_\chi - \varepsilon_{\chi'}), (\varepsilon_\chi - \varepsilon_{\chi''}), (\varepsilon_{\chi'} - \varepsilon_{\chi''}), j_1, j_2, j_1, j_2, r_1, r_2)$	$\langle\chi\|c_{l_1,\sigma_1,r_1}^{-j_1}\|\chi'\rangle\langle\chi'\|c_{l_2,\sigma_2,r_2}^{-j_2}\|\chi''\rangle\langle\chi''\|c_{l_2,\sigma_2,r_2}^{j_2}\|\chi'''\rangle\langle\chi'''\|c_{l_1,\sigma_1,r_1}^{j_1}\|\chi\rangle$
$D_{3bII}^{\chi,\chi'}(\chi'', \chi''')$	1	$\tilde{D}_{II}((\varepsilon_\chi - \varepsilon_{\chi''}), (\varepsilon_\chi - \varepsilon_{\chi'''}), (\varepsilon_{\chi'} - \varepsilon_{\chi'''}), j_1, j_2, j_1, j_2, r_1, r_2)$	$\langle\chi\|c_{l_1,\sigma_1,r_1}^{-j_1}\|\chi'\rangle\langle\chi'\|c_{l_2,\sigma_2,r_2}^{-j_2}\|\chi'''\rangle\langle\chi'''\|c_{l_1,\sigma_1,r_1}^{j_1}\|\chi''\rangle\langle\chi''\|c_{l_2,\sigma_2,r_2}^{j_2}\|\chi\rangle$
$D_{3cI}^{\chi,\chi'}(\chi'', \chi''')$	-1	$\tilde{D}_I((\varepsilon_\chi - \varepsilon_{\chi''}), (\varepsilon_{\chi'} - \varepsilon_{\chi''}), (\varepsilon_{\chi'} - \varepsilon_\chi), j_1, j_2, j_1, -j_2, r_1, r_2)$	$\langle\chi\|c_{l_2,\sigma_2,r_2}^{j_2}\|\chi'\rangle\langle\chi'\|c_{l_2,\sigma_2,r_2}^{-j_2}\|\chi'''\rangle\langle\chi'''\|c_{l_1,\sigma_1,r_1}^{-j_1}\|\chi''\rangle\langle\chi''\|c_{l_1,\sigma_1,r_1}^{j_1}\|\chi\rangle$
$D_{3cII}^{\chi,\chi'}(\chi'', \chi''')$	1	$\tilde{D}_{II}((\varepsilon_\chi - \varepsilon_{\chi''}), (\varepsilon_{\chi'} - \varepsilon_{\chi''}), (\varepsilon_{\chi'} - \varepsilon_{\chi'''}), j_1, j_2, -j_1, j_2, r_1, r_2)$	$\langle\chi\|c_{l_1,\sigma_1,r_1}^{j_1}\|\chi'\rangle\langle\chi'\|c_{l_2,\sigma_2,r_2}^{-j_2}\|\chi'''\rangle\langle\chi'''\|c_{l_1,\sigma_1,r_1}^{-j_1}\|\chi''\rangle\langle\chi''\|c_{l_2,\sigma_2,r_2}^{j_2}\|\chi\rangle$
$D_{3dI}^{\chi,\chi'}(\chi'', \chi''')$	1	$\tilde{D}_I((\varepsilon_{\chi'} - \varepsilon_\chi), (\varepsilon_{\chi'} - \varepsilon_{\chi''}), (\varepsilon_{\chi'} - \varepsilon_{\chi'''}), j_1, j_2, -j_1, j_2, r_1, r_2)$	$\langle\chi\|c_{l_1,\sigma_1,r_1}^{j_1}\|\chi'\rangle\langle\chi'\|c_{l_2,\sigma_2,r_2}^{-j_2}\|\chi'''\rangle\langle\chi'''\|c_{l_1,\sigma_1,r_1}^{-j_1}\|\chi''\rangle\langle\chi''\|c_{l_2,\sigma_2,r_2}^{j_2}\|\chi\rangle$
$D_{3dII}^{\chi,\chi'}(\chi'', \chi''')$	-1	$\tilde{D}_{II}((\varepsilon_{\chi'} - \varepsilon_\chi), (\varepsilon_{\chi'} - \varepsilon_{\chi''}), (\varepsilon_{\chi'} - \varepsilon_\chi), j_1, j_2, j_1, -j_2, r_1, r_2)$	$\langle\chi\|c_{l_2,\sigma_2,r_2}^{j_2}\|\chi'\rangle\langle\chi'\|c_{l_2,\sigma_2,r_2}^{-j_2}\|\chi'''\rangle\langle\chi'''\|c_{l_1,\sigma_1,r_1}^{-j_1}\|\chi''\rangle\langle\chi''\|c_{l_1,\sigma_1,r_1}^{j_1}\|\chi\rangle$

Table 3.1: *All eight diagrams D_{3X} depicted in Fig. 3.4 are calculated according to Eq. 3.48. The function $\tilde{D}_{I,II}$ corresponds to a double integral and is evaluated in appendix C. The factor S accounts for signs arising due to the diagrammatic rules (see appendix A).*

Chapter 4

Sequential transport in single and coupled quantum dots

The aim of this chapter is to discuss the main physical insights that can be obtained by studying quantum dot or molecular systems in a weak coupling regime. In this regime the temperature broadening of the Fermi levels in the reservoirs is much bigger than the finite lifetime broadening of the quantum dot states. Tunneling to and from the reservoirs takes place in sequential processes in which the electronic charge is transfered one by one. While early studies of electron transport through mesoscopic systems concentrated on the current [17, 19], more recent activities, both experimental [5, 46, 49, 51] and theoretical [22, 23, 26, 28, 34, 60, 94, 95, 96], include the analysis of shot noise. The latter provides additional insight into the quantum transport properties [42] and thus allows a more detailed characterization of the quantum transport device.
For 'local' systems, such as single or multilevel quantum dots the shot noise power S is typically sub-Poissonian above the sequential tunneling threshold. This implies that the Fano factor is less than unity. If the level couplings Γ_i are asymmetric, e.g. in the presence of magnetically polarized electrodes or spatial asymmetries, the noise can become super-Poissonian. In this case the Fano factor takes values larger than unity [27, 60]. Very recently it was found that enhanced noise can also be found in symmetric systems inside the Coulomb blockade region where the current is much suppressed [34, 61, 94]. We will discuss this effect in some detail in chapter 4.2 for the case of a double quantum dot. Larger systems such as serially coupled quantum dots or molecules can display super-Poissonian noise even in fully symmetric situations and above the sequential tunneling threshold [23]. This phenomenon is related to correlation effects which we discuss in some detail in chapter 4.3. 'Non-local' systems in general exhibit a pronounced and sensitive dependence of their transport characteristics on internal parameters and couplings due to their complex internal level structure. However, before we will focus on these more sophisticated models we will start our

discussion with a single two level quantum dot including photon relaxation as a basic model system.

4.1 Single quantum dot

In the following a comprehensive summary of the transport characteristics of a single two level quantum dot in the sequential tunneling regime is given. It is supposed to serve as an introduction to the main physical processes and transport features which have already been described from an experimental point of view in chapter 2.4. Our results in the following reproduce the ones from Ref. [92].

4.1.1 Model and Hamiltonian

We have already introduced a general Hamiltonian ($H = H_r + H_D + H_T$) in chapter 3.1. Since the structure of the tunneling Hamiltonian H_T and the reservoir term H_r is not altered throughout the discussion in this thesis we will only specify the dot Hamiltonian in each model. Our model is described by the central dot Hamiltonian of the form

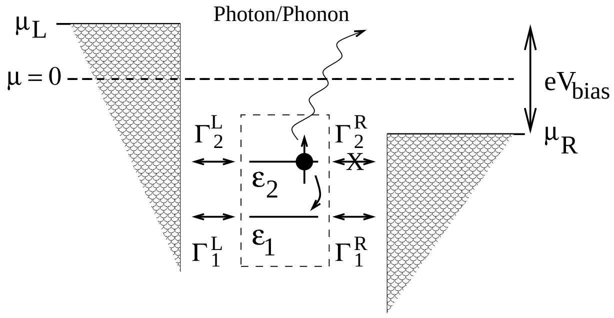

Figure 4.1: *Sketch of the coupling parameters and relaxation processes in a finite bias situation.*

$$H_{\mathrm{D}} = \sum_{i\sigma} \varepsilon_{i\sigma} c^{\dagger}_{i\sigma} c_{i\sigma} + U \sum_{i} n_{i\uparrow} n_{i\downarrow} + E_C \left(\sum_{i\sigma} n_{i\sigma} \right)^2 \tag{4.1}$$

where $i = 1, 2$. We include a charging energy E_C which accounts for the classical energy cost to add an extra charge on a confined system with many electrons. Photon relaxation processes are included in the sense that electrons on the dot can change the level by emitting or absorbing a photon for $i \neq j$ with the Hamiltonian

$$H_{\mathrm{ph}} = H_B + H_{B-D} = \sum_{q} \omega_q d^{\dagger}_q d_q + \sum_{q\sigma ij} g_{ph} (d^{\dagger}_q + d_q) c^{\dagger}_{i\sigma} c_{j\sigma}, \tag{4.2}$$

where we consider the coupling amplitudes to be independent of i, j and q, i.e. $g_q^{ij} = g_{ph}$. This leads to a total bosonic coupling constant $\alpha_{\mathrm{ph}}(\omega) = 2\pi g_{\mathrm{ph}}^2 \rho_{\mathrm{b}}(\omega)$. For the density of states of the photon bath we choose a power law behavior $\rho_{\mathrm{b}}(\omega) \propto \omega^3$, corresponding to photons with 3 spatial degrees of freedom. We take the electronic coupling strength $\Gamma_r^{i\sigma}$ to be independent of the spin and write Γ_i^r. Furthermore for symmetric tunneling couplings we choose $\Gamma_1^{\mathrm{L}} = \Gamma_1^{\mathrm{R}} = \Gamma_2^{\mathrm{L}} = \Gamma_2^{\mathrm{R}} = \Gamma$. Since the coupling parameter Γ in the sequential tunneling picture has to be small compared to all other energy parameters including the temperature, we set $k_{\mathrm{B}}T = 10\Gamma$ in this section. Furthermore we choose the temperature of the photonic bath to be the same as the one of the electronic reservoirs ($T_b = T$). As a set of energy parameters we use $\varepsilon_1 = -0.5, \varepsilon_2 = 0.5, U = 1.5$ and $E_C = 1$ (all in units of meV) which are typical energy scales in quantum dot experiments.

4.1.2 Transport characteristics

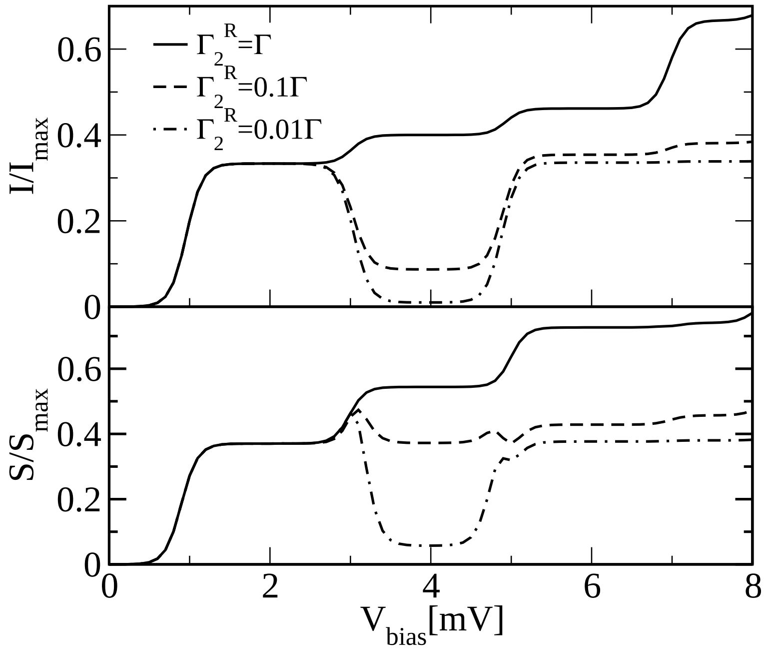

Figure 4.2: *Current and shot noise versus voltage for symmetric and unsymmetric couplings. Parameters are discussed in the text. Current and noise are normalized by* $I_{max} = (e/2\hbar)\Gamma$ *and* $S_{max} = (e^2/2\hbar)\Gamma$ *respectively.*

Diagonalizing our dot Hamiltonian we obtain sixteen eigenstates of the isolated quantum dot. The parameters given above correspond to a zero charged ground state and a first excited state which is reached at a bias $\varepsilon_1 + E_c$. The bias is dropped symmetrically across the dot-electrode junction. In the absence of photon relaxation and in a completely symmetric coupling situation the current and shot noise rise in a step wise manner (see solid line in Fig. 4.2). Each step corresponds to a new transport channel that is being opened at sufficient bias. The distance between two successive steps is thus given by the energy separation of two eigenstates from neighboring charge sectors (N and $N+1$ or $N-1$). Therefore the step positions are directly linked to the excitation spectrum of the quantum dot or molecule. The steps are broadened by temperature where the full width at half maximum (FWHM) is approximately $\approx 5.44 k_B T$. The steps are followed by plateaus corresponding to a fixed number of transport channels that contribute to the current. Fig. 4.2 shows the current and noise for various asymmetry ratios of the coupling constants Γ_i.

In our case the coupling to right electrode of the second orbital level Γ_2^R is suppressed

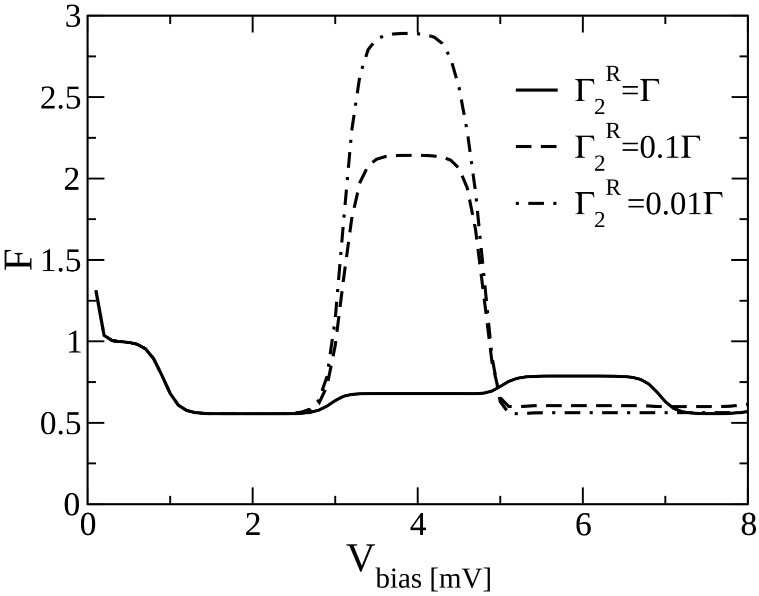

Figure 4.3: *Fano factor (S/2eI) versus voltage for symmetric and unsymmetric couplings. F becomes super Poissonian ($F > 1$) for strongly asymmetric coupling.*

with respect to the others. For a strong asymmetry we observe a decrease of the current and noise at the second plateau. This implies that the conductance ($\frac{\partial I}{\partial V}$) becomes negative. Negative differential conductance (NDC) indicates, that transport channels are being blocked, in this case due to asymmetric coupling to the leads.

The Fano factor in the corresponding transport regime is depicted in Fig. 4.3. At low bias the noise is mainly due to thermal noise and the Fano factor follows the well known hyperbolic cotangent behavior (Ref. [42]). With increasing bias the Fano factor shows a Poissonian plateau (F=1) in the Coulomb blockade. This regime is characterized by few, uncorrelated tunneling events (described by Poisson statistics) since sequential transport is exponentially suppressed. However at the sequential tunneling threshold, when transitions from the ground state to the first excited state become possible, the first current step appears and the Fano factor usually drops to values between 1 and 0.5 which is called sub-Poissonian. Subsequent plateaus in the Fano factor correspond to the occupation of exited states of the dot which in the case of symmetric coupling all open new transport channels and thus increase the current. In contrast in an asymmetric coupling situation the second current plateau which involves the occupation of the bad coupled second level leads to a decrease in the current. The drop in the current (NDC) is accompanied by a super-Poissonian Fano factor (see Fig. 4.3) indicating the co-existence of fast tunneling events interrupted by comparable long blocking periods due to the bad coupling of the second level to the right reservoir.

4.1.3 Relaxation processes

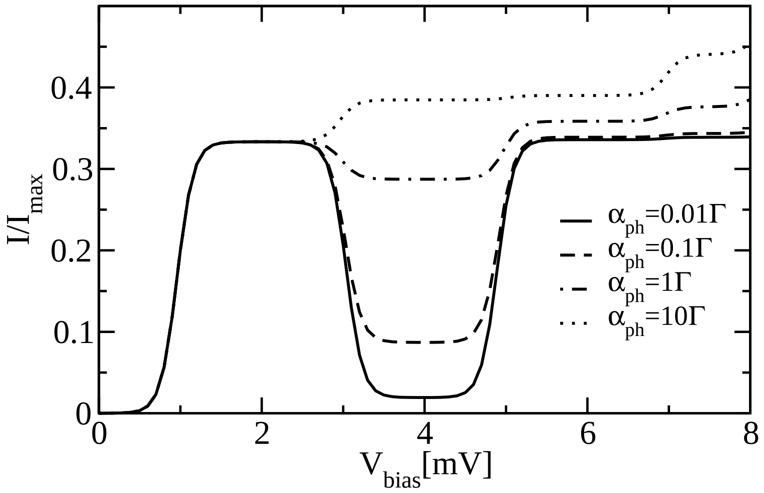

Figure 4.4: *Current versus voltage for an asymmetric coupling of* $\Gamma_2^R = 0.01\Gamma$. *The second plateau is lifted the stronger the relaxation rate (the higher the bosonic coupling constant* α*) until finally the NDC effect vanishes.*

Next we want to consider the effect of photon relaxation. Relaxation processes provide an additional contribution to our first order transition rates $W^{(1)}$ (see chapter 3 and appendix B) and thus influence the probabilities of the dot eigenstates. In Fig. 4.4 we show the current at fixed asymmetry $\Gamma_2^R = 0.01\Gamma$ for various bosonic coupling strengths α_{ph} to the bath. The NDC effect clearly vanishes in the case of strong relaxation. The reason is obvious. An electron that has formerly been stuck on the upper badly coupled level can now relax to the lower level and then tunnel out easily. The behavior of the Fano factor is accordingly (see Fig. 4.5). The super-Poissonian values are reduced such that for strong relaxation the Fano factor appears nearly flat at sub-Poissonian values ($F < 1$). The probability to occupy the upper badly coupled level is gradually reduced with higher coupling α to the bosonic bath. Hence the transport becomes more homogeneous and thus the noise (Fano factor) is reduced.

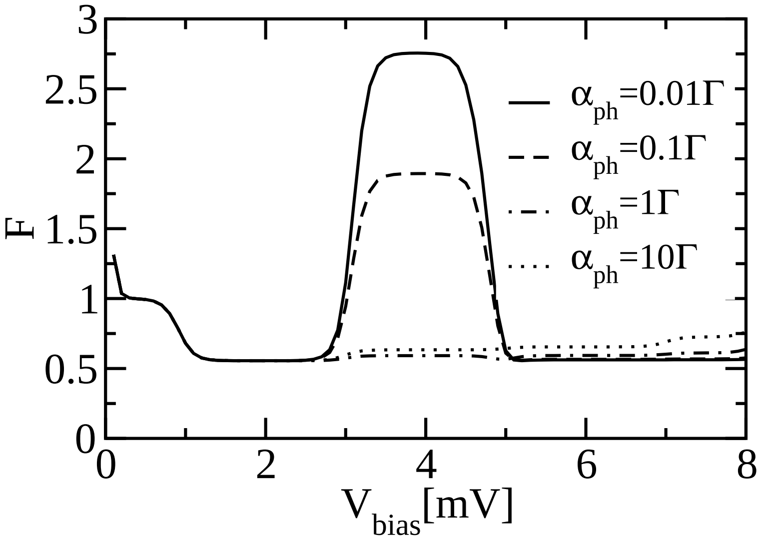

Figure 4.5: *Fano factor versus voltage for an asymmetric coupling of* $\Gamma_2^R = 0.01\Gamma$. *Super Poissonian noise (Fano factor) disappears and becomes sub-Poissonian for large relaxation rates (higher coupling constant* α*).*

4.2 Double quantum dot

As described in the previous chapter local systems such as single (multilevel) quantum dots already provide a decent basis to study the transport physics of molecular nanostructures. However, a major difference between a localized quantum dot structure and a real molecule is that the electronic wavefunction of the molecule is usually spatially delocalized. The delocalization of electrons can have strong effects on the transport characteristics and thus should be included in our analysis. A perfect candidate to study the effect of a spatially extended structure is a double quantum dot, in which the inter-dot coupling is much stronger than the coupling to the reservoir leads. For this reason they are often referred to as "artificial molecules" as introduced in chapter 2.

In the following chapter we will study sequential transport in a system of two strongly coupled quantum dots. Specifically, we consider a double quantum dot (DQD) in series in which the left dot is coupled weakly to left electrode and similarly the right dot to the right electrode, while the two dots are coupled strongly via electron tunneling, and they also interact electrostatically via the Coulomb interaction. We will address in particular two distinct issues:

(i) Transport in the Coulomb blockade regime:

In this regime we study the shot noise of the symmetrically coupled DQD in the Coulomb blockade regime, generalizing the work of Ref. [61]. Co-tunneling processes are assumed to be weak, hence transport is due only to thermally activated processes.

We find that in the Coulomb blockade regime the relation between two energy scales, the sequential tunneling energy ε_{seq} and the difference of the first excitation energy and the ground state (which is also the inelastic co-tunneling energy) ε_{co} determines the noise characteristics. This part of our analysis is valid generally for weakly coupled system in the Coulomb blockade regime, for any value of the gate voltage, as it depends only on the internal electronic structure of the interacting dot system.

(ii) Transport above the sequential tunneling threshold:
For the weakly coupled DQD super-Poissonian noise can only appear if the left ↔ right symmetry is broken. In the case of the local two level quantum dot (see chapter 4.1) symmetry breaking occurred due to an asymmetric level coupling. For a non-local system like the DQD symmetry breaking can be achieved in two qualitative different ways: the symmetry of the electrode-dot couplings is broken, while the DQD is unchanged or the symmetry of the DQD-Hamiltonian is broken by detuning the dot level energies while the symmetry of the electrode-dot coupling is preserved. The two scenarios differ in so far as in the first case the energy spectrum of the DQD remains unchanged which means that the step positions of the current and noise characteristics are not influenced by the coupling asymmetry. In the latter case detuning the dot level energies changes the energy spectrum and eigenstates of the DQD. The DQD eigenfunctions become spatially non-uniform which breaks the parity symmetry of the effective coupling of the various eigenstates to the electrodes. Thus the current and noise step characteristics differ for different degrees of detuning.

Such asymmetries are easily detected in an experiment. Various groups [35, 97, 98, 99] use measurement setups on DQDs in which metallic finger gates allow for a controlled manipulation of the relevant parameters, e.g the electrostatic potential of the individual dots as well as the inter-dot and dot-electrode couplings.

4.2.1 Model and Hamiltonian

Here we consider two coupled quantum dots, each with a sufficiently large level spacing such that we can restrict ourselves to one spin-degenerate level per dot. Including electron hopping between the dots as well as intra-dot and inter-dot (nearest neighbor) Coulomb interactions we arrive at the central dot Hamiltonian

$$\hat{H}_{\mathrm{DQD}} = \sum_{i\sigma} \varepsilon_i n_{i\sigma} - t \sum_{\sigma} (c^{\dagger}_{1\sigma} c_{2\sigma} + h.c.) + U \sum_{i} n_{i\uparrow} n_{i\downarrow} + U_{nn} \sum_{\sigma\sigma'} n_{1\sigma} n_{2\sigma'}, \tag{4.3}$$

with on-site energy ε_i and inter-dot hopping t. $c^{\dagger}_{i\sigma}, c_{i\sigma}$ are Fermi operators for the molecular levels, and $n_{i\sigma} = c^{\dagger}_{i\sigma} c_{i\sigma}$ is the number operator. The strength of the intra-dot and inter-dot Coulomb repulsion is given by U and U_{nn} respectively. The parameters U and U_{nn} can be related to the charging energies of the dots and the various capacitances when comparing to experimental setups as described for instance in Ref. [19]. Other electron interaction terms could be considered by much more elaborate models, as done in Ref. [64] for computation of the $I-V$ characteristics. For the effects on the shot noise that we wish to study, the simpler model above suffices. Tunneling is described by H_T^R, H_T^L (see chapter 4.1) and is only possible between the reservoirs and the corresponding adjacent dot. The respective coupling strength is characterized by the intrinsic line width $\Gamma_r = 2\pi|t_r|^2\rho_e$, where t_r are the tunneling matrix elements. In the $N = 2$ dot system there exist $4^N = 16$ eigenstates χ of the form $\chi = \sum_s c_s|s\rangle$, where $|s\rangle$ denotes a basis state of the form $|n_{1\uparrow}n_{1\downarrow}n_{2\uparrow}n_{2\downarrow}\rangle$ and the c_s are the corresponding coefficients. The analytic form of the eigenstates and eigenvalues of our Hamiltonian can be found in Ref. [60].

In the following we discuss current and shot noise for systems described by a Hamiltonian of the type of Eq. 4.3 in first order perturbation theory in the tunnel couplings Γ_r. In the first part of the discussion special emphasis is put on examining the behavior of the Fano factor (noise) in the Coulomb blockade region. The second part will be devoted to the discussion of asymmetry effects induced to the double dot system by asymmetric coupling to the leads or detuned level energies, respectively. In the case of symmetric couplings we choose $\Gamma_\mathrm{L} = \Gamma_\mathrm{R} = 2.5\mu\mathrm{eV}$ defining a total line width of $\Gamma = \Gamma_\mathrm{L} + \Gamma_\mathrm{R} = 5\mu\mathrm{eV}$. We choose this explicit energy scale as we are varying a number of different energy parameters in the following. Our perturbation expansion is valid for temperatures much larger than the tunnel couplings. For the following discussion we choose $k_\mathrm{B}T = 10\Gamma$ which translates to $T = 50\mu\mathrm{eV} \sim 0.6\mathrm{K}$. The dot system is characterized by the level energies ε_i, the intra-dot 'Hubbard' repulsion U, and the nearest neighbor charge repulsion U_{nn}. If not stated otherwise the level energies are chosen to be resonant, $\varepsilon_1 = \varepsilon_2 = \varepsilon$.

A current is driven by an applied bias voltage $V_\mathrm{b} = \mu_\mathrm{L} - \mu_\mathrm{R}$. We assume the voltages to drop symmetrically and, since the dot-electrode coupling is weak compared to the dot-dot coupling, entirely at the electrode-dot tunnel junctions. This implies that the level energies of the dots are independent of the applied voltage. Effects such as level detuning due to asymmetric or incomplete voltage drops and or applied gate voltages could easily be included. We do not consider these effects here, as they add unnecessary complexity to the results presented below. We include only a single level per dot (plus interactions), assuming that the level spacing within each dot is larger than all other energy scales.

To proceed we diagonalize the dot Hamiltonian H_{DQD} including the interaction terms. The resulting eigenstates can be organized according to the two quantum numbers: total charge $-qe$ (with q an integer, $q \in 0, 1, 2, 3, 4$) and total spin (singlets, doublets and triplets for our DQD model) [60]. As the on-site energies ε_i are decreased to lower, negative values (experimentally achieved by a gate voltage applied to both dots) the ground state charge shifts from $q = 0$ to increasing values $q = 1$, $q = 2, \ldots$. While previous work [28, 61] has focused mostly on the zero charge ($q = 0$) ground state we study the more interesting case (see below) with a “half filled” ground state ($q = 2$), where the low-bias transport sensitively depends on the spatial and spin structure of the eigenstates.

For the sequential transport in quantum dot systems at low bias two energy scales are relevant: (1) The ”sequential energy gap” ε_{seq} denotes the energy difference between the ground state with charge $-qe$ and the first excited states with the charge $-(q+1)e$ (“anion ground state”) or with charge $-(q-1)e$ (“kation ground state”), depending on which one is smaller. The sequential tunneling threshold, i.e. the bias above which the current is no longer suppressed due to Coulomb blockade, is reached at $V = 2\varepsilon_{seq}/e$ for symmetric bias. (2) The energy gap between the ground state with charge $-qe$ and the first excited state with the same charge, denoted in the following by ε_{co}. The energy ε_{co} is also known as the ‘vertical’ gap, and is often related to the HOMO-LUMO gap in molecular systems. It would be the energy scale relevant for inelastic co-tunneling processes. Note, however, that co-tunneling processes, which are second order in Γ_r, are not included in our discussion. If one would start with a ground state of zero charge ($q = 0$) the energy scale ε_{co} would not exist within our model, due to the restriction to single level dots. As we consider the case of a half filled ground state we avoid such an artefact. Note that recent experiments on double quantum dot systems with applications for quantum computing [35, 39, 98] also work with ground states of non-zero charge.

4.2.2 Symmetrically coupled quantum dots

We begin with a system of two dots in series and energy parameters such that the DQD is half filled in the ground state (no bias applied). In the right panel of Fig. 4.6 part of the energy excitation spectrum resulting from the diagonalization of the Hamiltonian is displayed. The ground state G is a singlet state with total spin $S = 0$ and charge $-2e$ ($q = 2$). It is delocalized over the two dots (a combination of the four two electron singlet basis vectors $|s\rangle$) with an eigenvalue E_{G} dependent on all parameters of H_{DQD}, $E_{\mathrm{G}} = 2\varepsilon + 1/2(U + U_{nn} - \Delta)$, where $\Delta = \sqrt{16t^2 + (U - U_{nn})^2}$ [60]. The first excited state is the bonding state B with $q = 1$. It is a doublet with total spin 1/2, eigenvalue $\varepsilon - t$, and is also delocalized over both dots. Therefore, the energy scale ε_{seq} is given $\varepsilon_{seq} = E_{\mathrm{B}} - E_{\mathrm{G}}$. The second excited state is a triplet with total spin $S = 1$ with $q = 2$. In the triplet state one electron each is ”fixed” to one dot. Therefore, its eigenvalue is independent of the inter-dot hopping t and the on-site repulsion U. The energy scale ε_{co} is thus given by $\varepsilon_{co} = E_{\mathrm{T}} - E_{\mathrm{G}}$. The rest of the spectrum is not shown, since for the following discussion we will refer to a bias regime for which other states are not yet important. The higher excited states are responsible for the step features above $V_{\mathrm{b}} \sim 5mV$. Note that in the artificial limit $U \to \infty$ the energy scale ε_{co} vanishes. In this case, the triplet and singlet states would be degenerate and some of the effects described below would disappear.

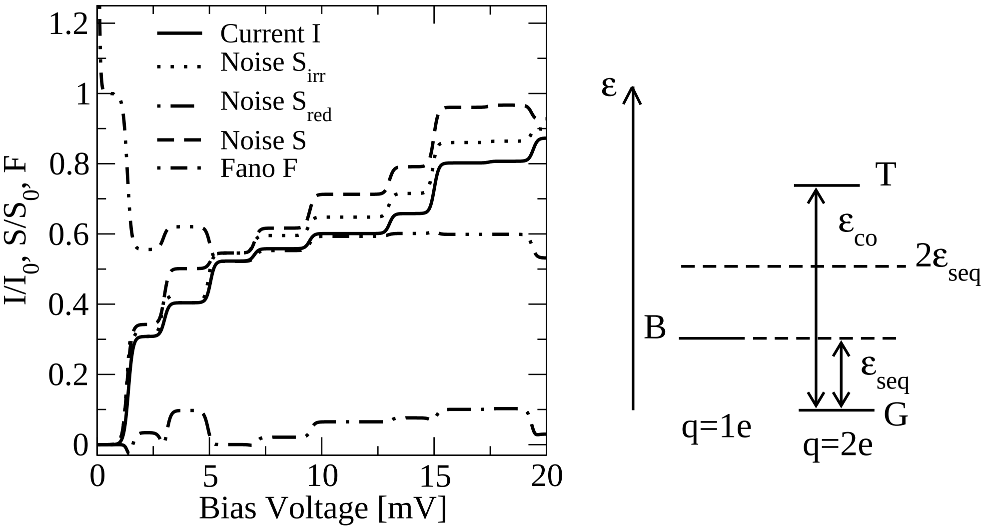

Figure 4.6: *left panel: Current I and shot noise S vs. bias voltage for a double dot system with $k_{\mathrm{B}}T = 0.05$, $t = 2$, $U = 10$, $U_{nn} = 5$ and $\varepsilon = -5.5$ resulting in a doubly occupied ground state ($q = 2e$), all units in meV. The noise S is sub-Poissonian for all bias voltages. This is always the case if the first vertical excitation energy is larger than twice the sequential tunneling threshold, $\varepsilon_{co} > 2\varepsilon_{seq}$, see the sketch in the right panel. Current and noise curves are normalized to $I_0 = (e/\hbar)2\Gamma$ and $S_0 = (e^2/\hbar)2\Gamma$, respectively. Right panel: sketch of the low energy spectrum. The nature of the states G,T and B is discussed in the text.*

Fig. 4.6 shows the typical behavior for a fully symmetric system with $\varepsilon_{co} > 2\varepsilon_{seq}$: both current and noise rise monotonically in steps, while the Fano factor will fall between values of 1 (Poissonian noise) and 1/2 (symmetric double barrier noise) for the large bias region, i.e. at bias voltages larger than all excitation energies. In general, the Fano factor will not fall with a monotonous dependence on the bias. This non-monotonicity is due to the second term in the noise expression Eq. 3.38, associated with the propagator **P**, which can give positive and negative contributions. In the Coulomb blockade current and noise are both (equally) exponentially suppressed resulting in a Fano factor of Poissonian value. At small bias, $eV_{\mathrm{b}} \ll k_B T$, the noise is dominated by thermal noise, described by the well known hyperbolic cotangent behavior which leads to a divergence of the Fano factor [38, 42].

If we now lower the on-site energy ε we energetically favor states with larger charge and thus increase the energy ε_{seq} as compared to the situation as shown in the right panel of Fig. 4.6, while preserving the energy ε_{co}. Thereby, we can realize a situation in which $\varepsilon_{seq} < \varepsilon_{co} < 2\varepsilon_{seq}$, see Fig. 4.7. Above the sequential threshold the current and noise curve look very similar to the situation in Fig. 4.6, with the expected small shifts in the step positions. However, in the Coulomb blockade region the Fano factor behaves differently to before. After the region of thermal noise accompanied with divergent Fano factor, a Poissonian value of $F = 1$ is reached. For higher bias and close to (but still below) the sequential tunneling threshold a peak like feature (actually a short plateau) appears in the Fano factor. This is caused by a relative enhancement of the noise, visible in Fig. 4.7 and Fig. 4.9 by the apparent shift of the noise curve to lower bias in the left panel. The increase of the Fano factor is due to the second term in the noise expression of Eq. 3.38 which we denote by S_{red}, whereas the first part is called S_{irr}. A comparison of the two noise contributions can be seen in Fig. 4.8 (note the semi-logarithmic scale). The first part of the noise S_{irr} provides the finite thermal noise around zero bias. It then grows with bias with the same exponential behavior as the current and contributes a Poissonian term $2eI$ to the shot noise. In contrast, the (now positive) second part S_{red} becomes only appreciable for a bias $V_{\mathrm{b}} > (\varepsilon_{co} - \varepsilon_{seq})/e$ and renders the shot noise super-Poissonian above this bias. This noise enhancement is due to the possible thermal occupation and subsequent sequential depletion of excited states that lead to small cascades of tunneling events interrupted by long (Coulomb) blockages. The alternation of these processes with different time scales results in a noisy current. Consequently, the Fano factor is larger than unity, indicating super-Poissonian noise. This effect was discussed in some detail by Belzig and co-workers [61, 94], for systems restricted to a singly occupied ground state. At a bias higher than the sequential threshold the noise recovers sub-Poissonian behavior.

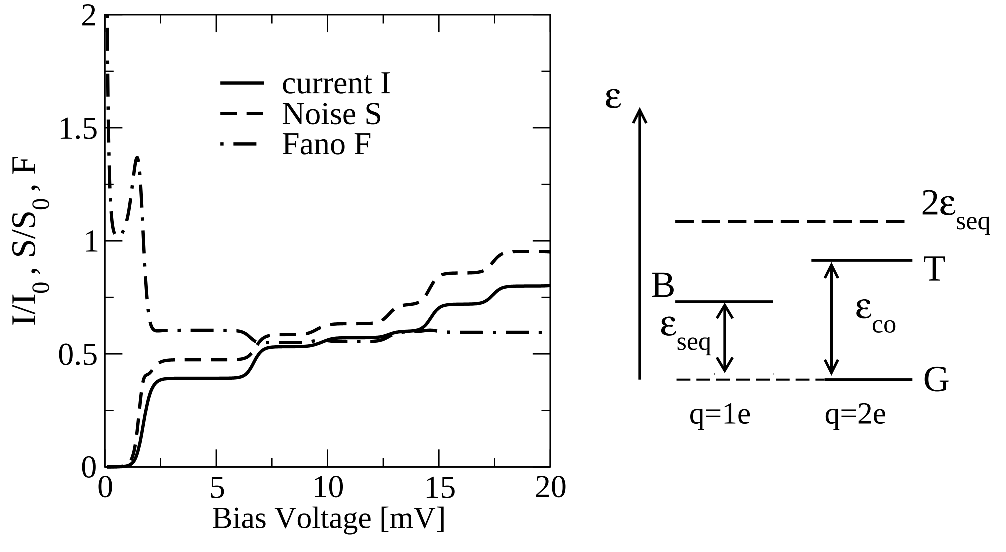

Figure 4.7: *Left panel: Current I and shot noise S vs. voltage for a double dot system with* $k_{\mathrm{B}}T = 0.05$, $t = 2$, $U = 12$, $U_{nn} = 4\mathrm{meV}$ *and* $\varepsilon = -5.3$. *Super-Poissonian noise (Fano factor* $F > 1$*) develops in the Coulomb blockade regime. Right panel: low energy spectrum, where now* $\varepsilon_{seq} < \varepsilon_{co} < 2\varepsilon_{seq}$.

For the same parameters as above but with further lowered on-site energy $\varepsilon = -6.3$

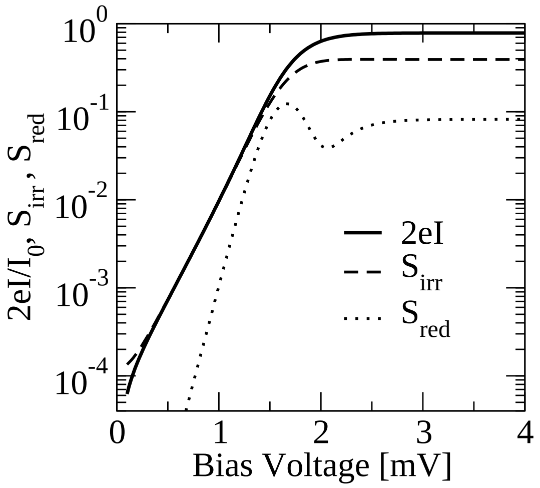

Figure 4.8: *Enlarged low bias region of Fig. 4.7.* $2eI, S_{red}$ *and* S_{irr} *are plotted semi-logarithmically. The first part of the noise* S_{irr} *grows with bias as the current, providing a Poissonian noise contribution. The second part of the noise* S_{red} *becomes appreciable for* $V > 2(\varepsilon_{co} - \varepsilon_{seq})/e$ *and causes the total noise enhancement.*

we obtain a situation where $\varepsilon_{co} < \varepsilon_{seq}$. The current, noise and Fano factor for such a situation are depicted in Fig. 4.9. For a bias larger than the sequential tunneling threshold the curves show again generic behavior as displayed in Fig. 4.6 and Fig. 4.7. However, in the Coulomb blockade regime and after divergent thermal noise behavior we directly obtain a super-Poissonian Fano factor $F \approx 2.8$ in form of a plateau and do not recover a Poissonian value in the entire Coulomb blockade regime at all. In this case, S_{red} gives a large contribution that behaves with the same exponential behavior as the current rather than dropping faster than the current at low bias (as depicted in Fig. 4.7). Thus the noise is enhanced in the entire Coulomb blockade regime. The term S_{irr} again provides the thermal noise at very low bias and a contribution of $2eI$ below the bias $V_\mathrm{b} > (\varepsilon_{seq} - \varepsilon_{co})/e$. Above this bias, there is a redistribution between S_{irr} (losing) and S_{red} (winning), however, the sum of the two terms grows exactly like the current, leading to a constant (super-Poissonian) Fano factor.

Summarizing the above discussion we can distinguish three possible situations in the Coulomb blockade region:
i) For $\varepsilon_{co} > 2\varepsilon_{seq}$ the sequential processes start at a bias before the excited states come into play, and the noise is Poissonian, i.e. $F = 1$ once the thermal noise becomes negligible. This is the case for Fig. 4.6, as sequential transport via the ground state G and the "bonding state" B takes place before the triplet state T can be reached from the bonding state B.
ii) For $\varepsilon_{seq} < \varepsilon_{co} < 2\varepsilon_{seq}$ there is super-Poissonian noise $F > 1$ in the bias range $2(\varepsilon_{co} - \varepsilon_{seq})/e < V_\mathrm{b} < 2\varepsilon_{seq}/e$, see Fig. 4.7. This is due to the transport scenario

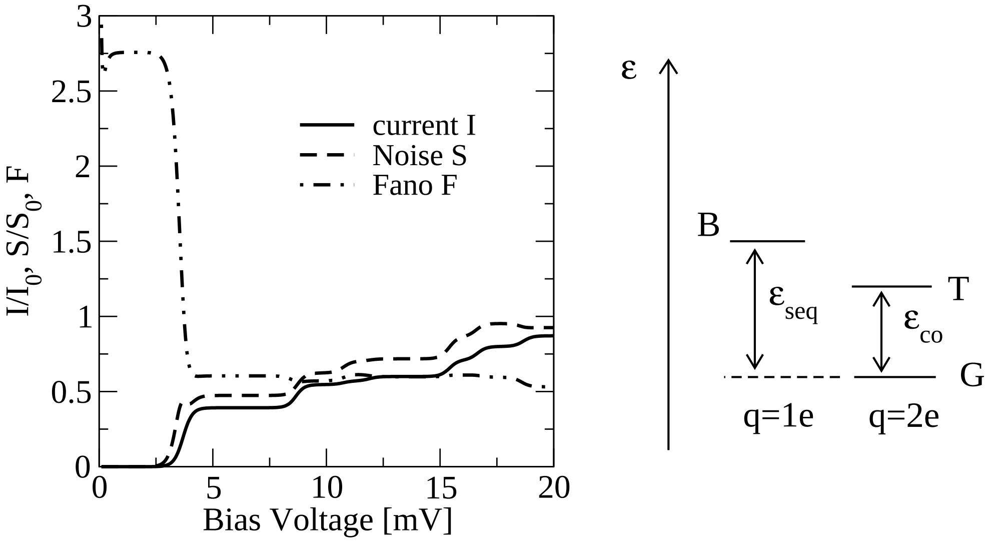

Figure 4.9: *Left panel: Current I and shot noise S versus voltage for a double dot system with $k_\mathrm{B}T = 0.05$, $t = 2$, $U = 12$, $U_{nn} = 4$ and $\varepsilon = -6.3$. Super-Poissonian noise develops in the entire Coulomb blockade region. Right panel: the corresponding low energy spectrum, where $\varepsilon_{co} < \varepsilon_{seq}$.*

discussed above, as for a bias in this range a thermally excited system can for a time do sequential transport through the excited states, before recovering to the ground state.

iii) For $\varepsilon_{co} < \varepsilon_{seq}$ we have $F > 1$ for the entire Coulomb blockade region. For a bias $2(\varepsilon_{seq} - \varepsilon_{co})/e < V_\mathrm{b} < 2\varepsilon_{seq}/e$ the situation is the same as in scenario ii). Below this bias range the physical picture due to Ref. [61] needs to be modified, as sequential transport is "blocked" (thermally activated) even out of the first excited state for $V_\mathrm{b} < 2(\varepsilon_{seq} - \varepsilon_{co})/e$. Nevertheless, the Fano factor actually remains constant as the bias drops below $2(\varepsilon_{seq} - \varepsilon_{co})/e$, see Fig. 4.9.

However, as was pointed out in Ref. [22], the super-Poissonian noise behavior due to sequential tunneling processes in the Coulomb blockade regime is very easily modified by co-tunneling processes as discussed later in chapter 5.

The experimental distinction of scenarios ii) and iii) can therefore be difficult: although the Fano factor looks different in pure sequential transport, if co-tunneling processes play a role, scenarios ii and iii) will display qualitatively similar Fano factor behavior.

4.2.3 Influence of asymmetries

We now turn to the discussion of transport above the sequential tunneling threshold, i.e. in the bias region where electrons can tunnel sequentially through the DQD because they have sufficient energy to overcome the Coulomb blockade. For the symmetric situations as discussed above, the current and the noise increase monotonically in steps, where the step positions are determined by the many-body excitations of the DQD. For our DQD system, the noise in a symmetric transport situation remains sub-Poissonian (Fano factor $F < 1$) at all bias above the sequential tunneling threshold.

Asymmetric coupling

In a situation where the couplings are asymmetric, e.g. when the coupling to the left electrode is suppressed relative to the coupling to the right electrode, $\Gamma_\mathrm{L}/\Gamma_\mathrm{R} < 1$ the noise can become super-Poissonian. Let us consider a case in which the energy parameters are chosen to be the same as in the situation displayed in Fig. 4.6. The ground state is again a two electron state with $\varepsilon_{co} > 2\varepsilon_{seq}$. Hence for the following discussion one should refer to the qualitative energy spectrum shown in the right panel of Fig. 4.6. In Fig. 4.10 the upper graph depicts the Fano factor and the lower graph the absolute value of the current for various asymmetry ratios $\Gamma_\mathrm{L}/\Gamma_\mathrm{R}$ (the current is negative for negative bias). In the symmetric case, represented by the solid line, the Fano factor as well as absolute current and the noise (that is not depicted here) show a fully symmetric behavior under the reverse of the bias voltage. The first plateau is reached when the transition from the doubly occupied ground state G ($q = 2e$) to the lowest single occupied state, the bonding state B, ($q = 1e$) becomes allowed at the sequential tunneling threshold ($V_\mathrm{b} = 2\varepsilon_{seq}/e$)). At these plateaus the current, noise and Fano factor are functions of the coupling constants Γ_r only. At negative bias on the first plateau, the Fano factor is given by

$$F = \frac{4\Gamma_\mathrm{L}^2 + \Gamma_\mathrm{R}^2}{(2\Gamma_\mathrm{L} + \Gamma_\mathrm{R})^2}\,. \tag{4.4}$$

This gives a value of $\frac{5}{9}$ at the first plateau for symmetric coupling. For positive bias voltage one needs to exchange Γ_L with Γ_R, respectively. This result can be related to the discussion in Refs. [26, 27].

For the curves with $\Gamma_\mathrm{L}/\Gamma_\mathrm{R} \neq 1$ there is a clear asymmetry in current and Fano factor. The first plateau value of the Fano factor is increased for positive bias and (for smaller asymmetry) decreased for negative bias according to the above expression for the Fano factor. Further suppression of the left coupling leads to a region of negative differential conductance (NDC) and eventually a super-Poissonian Fano factor on the second plateau at negative bias (see dash-dotted curve for $\Gamma_\mathrm{L}/\Gamma_\mathrm{R} = 0.1$). The reason for the current suppression and asymmetric behavior is the interplay of the asymmetric couplings and the internal electronic structure. The occupation of the states participating in transport at the plateaus is highly sensitive to the asymmetric couplings.

Let us consider the first plateaus (positive and negative bias) of the current in the case $\Gamma_\mathrm{L}/\Gamma_\mathrm{R} = 0.1$. For negative bias, in contrast to the symmetric case where the ground state G and the bonding state B are equally occupied, we have now a higher probability

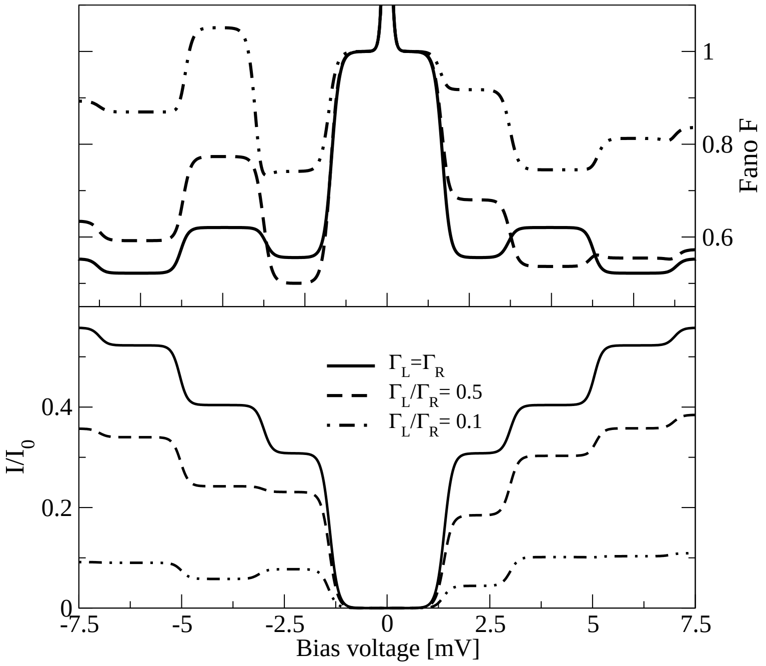

Figure 4.10: *Current I (absolute value) and Fano factor S vs. voltage for asymmetric coupling in a double dot system with $k_{\mathrm{B}}T = 0.05$, $t = 2$, $U = 10$ and $U_{nn} = 5$, $\varepsilon = -5.5$. For strong asymmetry negative differential conductance and super-Poissonian noise appear only for negative bias voltages. Note that due to the asymmetry the total line width $\Gamma = \Gamma_{\mathrm{L}} + \Gamma_{\mathrm{R}}$ and the current are reduced relative to the symmetric case.*

to be in the state G than in the state B. This is due to the fact that it is "easy" to populate the DQD from the right but "difficult" to depopulate the DQD in direction of the left electrode because of the suppressed coupling. As a consequence the system is occupied by two electrons most of the time. The reverse holds for positive bias, where the dot is most often occupied by one electron and consequently the probability to be in the state B on the first plateau is higher than to be in the ground state G.

To obtain the current I we need to consider the relevant current rates W^I in addition to the probabilities of the various states. On the first plateaus, the relevant current rates $W^I_{\mathrm{G}\to\mathrm{B}_\sigma}$ from ground state to bonding state(s) (with given spin σ) at negative bias are equal in magnitude to the reverse rates $W^I_{\mathrm{B}_\sigma\to\mathrm{G}}$ at positive bias (independent of the spin σ of B_σ). Solving the master equation, as a result of the coupling asymmetry the probability p_G to be in state G on the first plateau at negative bias is however larger (almost twice) than the occupation p_{B_σ} for states B_σ on the first plateau at positive bias. The combination of the same relevant current rate but different occupations leads to a higher (absolute) value of the current on the first plateau at negative bias than on the corresponding plateau at positive bias. To be concrete, if we consider the currents on the left interface of the DQD we have at negative bias a current with absolute value $|2\,W^{I}_{\mathrm{G}\to\mathrm{B}}\,p_{\mathrm{G}}|$ which is almost twice as large (for $\Gamma_{\mathrm{L}}/\Gamma_{\mathrm{R}} = 0.1$) than the current $W^{I}_{\mathrm{B}\to\mathrm{G}}\,2\,p_{\mathrm{B}_\sigma}$ going through the left interface at positive bias. Here, the factors of two originate from the spin summation over the bonding state doublet.

On the first plateau the Fano factor is monotonically increasing for positive bias with decreasing $\Gamma_{\mathrm{L}}/\Gamma_{\mathrm{R}}$ until it would reach the Poissonian value $F \to 1$ for very large asymmetry, resembling the noise of an effective single barrier. For negative bias on the first plateau, the Fano factor (given by Eq. 4.4) is not monotonic: it first decreases until it reaches $F = 1/2$ for $\Gamma_{\mathrm{L}}/\Gamma_{\mathrm{R}} = 0.5$, then it increases until it also would reach the Poissonian value for large asymmetry. This non-monotonic behavior reflects the interplay of asymmetry and different spin multiplicity of the relevant states G and B.

At the second plateau the transition from the bonding state B to the first excited triplet state T ($q = 2$) becomes possible and thus provides a second current channel. The stationary probabilities are redistributed in the following way: For negative bias, the states G and each of the three triplet states $\mathrm{T}_m, m \in \{-1, 0, 1\}$ have approximately equal occupation (within 10 percent). As a consequence of the threefold spin multiplicity of the triplet the probability of the ground state decreases to less than one third of its value on the first plateau. The bonding state B also loses some of its (already small) probability to the competing triplet states. The tunneling processes from the triplet state(s) T to the bonding state(s) B contribute an additional current via the current rates $W^{I}_{\mathrm{T}\to\mathrm{B}}$ (per triplet state and spin of B). However, even when summing over all the triplet contributions the resulting current is too small to compensate the loss from the processes involving the ground state. Therefore a region of negative differential conductance (NDC) appears as soon as the triplet states play a role in transport for negative bias (at the considered coupling asymmetry). The NDC is accompanied by a (relatively) enhanced noise because the competing processes involving the ground state and the triplets have sufficiently unequal rates $W^{I}_{\mathrm{G}\to\mathrm{B}}$ and $W^{I}_{\mathrm{T}\to\mathrm{B}}$ to form 'slow' and 'fast' transport channels. This competition leads to the super-Poissonian Fano factor as depicted in Fig. 4.10.

For positive bias on the second plateau the situation is quite different. Here, the DQD remains mostly in the bonding state B, i.e. there is no major loss of occupation for the bonding state (about 10 percent). Again the current leaving the dot consists of two additive contributions. In addition to the ground state contribution already present on the first plateau, the transitions between bonding to the triplet states add a large contribution and thus the current increases stepwise to a second, higher plateau.

The above illustrates that although for one bias direction (here positive) the current and shot noise show generic behavior (and the Fano factor is always sub-Poissonian), the situation can be quite different for the reverse bias. As such asymmetries are easily verified in an experiment, we can learn much about the underlying asymmetries of the couplings and the spin multiplicities of the states participating in transport. Note that

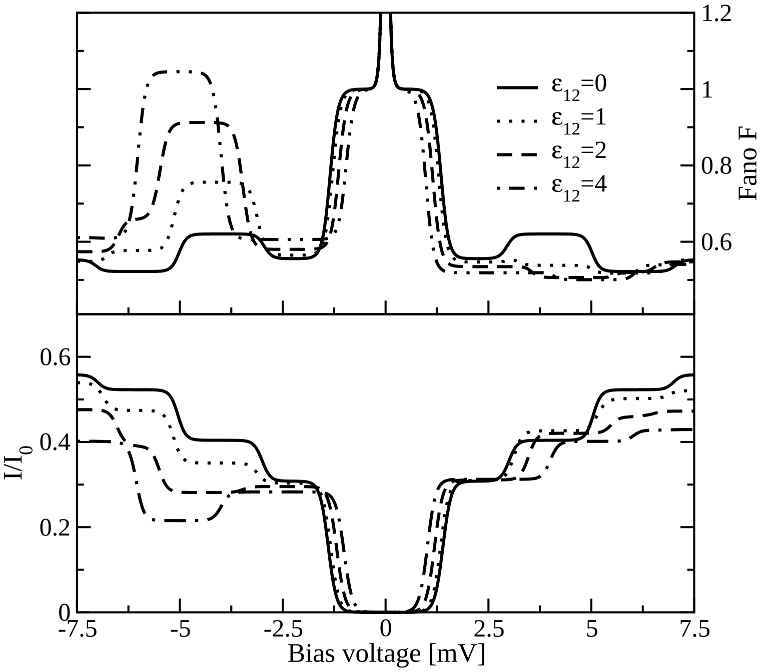

Figure 4.11: *Current I (absolute value) and Fano factor S vs. voltage for various values of level detuning ε_{12} but with symmetric couplings to the leads and other energy parameters equal to the situation depicted in Fig. 4.6. Stronger detuning ε_{12} leads to NDC and eventually super-Poissonian noise. In contrast to Fig. 4.10, the bias (energy) positions of current and noise features are changed due to the modified dot Hamiltonian.*

the NDC and super-Poissonian noise would completely disappear if we would take the on-site Coulomb repulsion $U \to \infty$. Due to a finite U the singlet ground state can benefit from 'local singlets', i.e. states with two electrons of opposite spin on the same dot, whereas there is no equivalent for triplet states. Therefore, the singlet ground state has a lower energy and different transitions rates as compared to the triplet states, both of which are necessary conditions for the NDC and super-Poissonian noise in the considered single-level model.

Detuned level energies

The discussion above serves as a basis to qualitatively understand transport in the more complicated situation when the symmetry of the DQD Hamiltonian itself is broken, rather than merely its coupling to the electrodes. In the following, we detune the level energies $\varepsilon_1 - \varepsilon_2 = \varepsilon_{12}$ and also vary the inter-dot hopping t while the other parameters of the dot system remain the same and the couplings remain symmetric, $\Gamma_{\mathrm{L}} = \Gamma_{\mathrm{R}}$. For an experiment, this implies a gate electrode for each dot that can be controlled separately. Similar to above in Fig. 4.10, if roughly $|\varepsilon_1 - \varepsilon_2| = |\varepsilon_{12}| > |t|$, NDC and super-Poissonian noise can be realized at some bias.

In Fig. 4.11 we show current and Fano factor for different level detuning ε_{12}. The black solid line corresponds to symmetric couplings and resonant levels $\varepsilon_1 = \varepsilon_2$. It is the same as depicted in Fig. 4.10. If we start detuning the levels, i.e. $\varepsilon_{12} \neq 0$ we change our excitation energies and the states become more localized on the dot with lower energy (here the right dot). Consequently, we find the current and Fano factor plateaus at different (energy) positions as before, with different length of the plateaus. Note that the current on the first plateau only weakly changed for all ε_{12} considered here. This is due to the fact that despite of the changed Hamiltonian, the tunneling rates from ground state to bonding state as well as the occupations of these states are almost the same. The occupations on the first plateau are also only weakly dependent on the sign of the bias, quite different to the situation with asymmetric couplings considered above. Only with an even stronger level detuning would the current be significantly changed on the first plateau. However, the considered detuning of levels still leads to NDC and eventually to a super-Poissonian Fano factor, e.g. for $\varepsilon_{12} = 4$ at negative bias. The effect of triplet states on the second plateau is qualitatively the same as in the scenario with asymmetric coupling discussed above. For positive bias the current remains monotonic and the Fano factor remains sub-Poissonian. In agreement with previous results [28] the maximum current at very large bias (not shown) decreases with increased detuning although the total coupling Γ remains unchanged.

Instead of further increasing the level detuning one can also achieve "localization" of states by decreasing the inter-dot hopping t. Let us consider again the symmetrically coupled system ($\Gamma_{\mathrm{L}} = \Gamma_{\mathrm{R}}$) at a fixed detuning of $\varepsilon_{12} = 2$ for various values of the inter-dot hopping t (see Fig. 4.12). The solid line corresponds again to the case, in which $\varepsilon_{12} = 2$ and $t = 2$, as was also depicted in Fig. 4.11(dashed line). As expected, the plateaus of the current are again asymmetric since we have detuned level energies. If we now decrease t, the bonding state and the ground state will be separated by only a very small energy (as $U_{nn} = 5$ and $(\varepsilon_1 + \varepsilon_2)/2 = 5.5$) and thus the Coulomb blockade almost disappears. For positive bias both current and Fano factor (noise) behave generically. The first plateau for negative bias is again due to tunneling processes involving the states B and G. At the second plateau the triplet T starts participating in the transport and is strongly occupied, resulting in NDC and super-Poissonian noise as discussed above. At even more negative bias there exists a second region of NDC (for the cases $t = 1$ and $t = 0.5$). This is where the anti-bonding state (not depicted in the spectrum in the right panel of Fig. 4.6) is also contributing to the transport. The maximum current at large bias (not shown) depends on the inter-dot hopping t if the dot levels are out of resonance [28].

From Fig. 4.11 and Fig. 4.12 one can conclude that a higher degree of localization of the states participating in transport, achieved either by a strong detuning of level energies or a decrease in the inter-dot hopping, favors transport features such as NDC and makes the current more and more noisy, leading eventually to super-Poissonian noise.

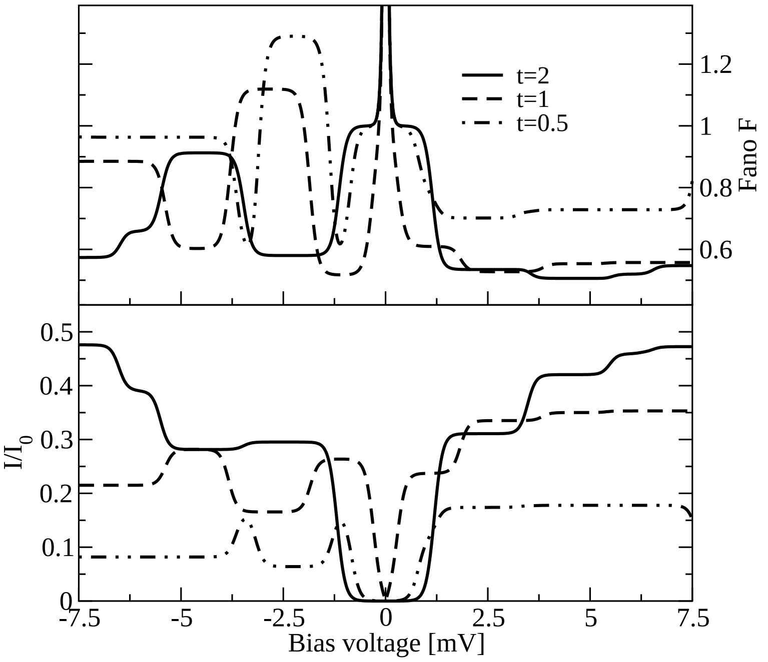

Figure 4.12: *Current I (absolute value) and Fano factor S vs. voltage for various "hopping" parameters t and a level detuning of* $\varepsilon_{12} = 0.2$*, symmetric coupling to the leads and otherwise same parameters as in the situation depicted in Fig. 4.6. Reduced hopping causes a smaller total current although super-Poissonian noise and NDC develop similarly as in Fig. 4.11.*

Reducing the hopping (at fixed detuning) therefore has a similar effect on transport as a larger detuning at fixed hopping. However, as the DQD spectrum differs non-linearly between different parameter sets with identical ratio ε_{12}/t the resulting transport curves can not be scaled, but depend explicitly on the value of each parameter.

For reference we show in Fig. 4.13 the current and Fano factor for a fully symmetric system, i.e. equal couplings to left and right and resonant level energies but for different values of the inter-dot hopping t. As expected all curves behave symmetric under the reverse of bias. Similar to Fig. 4.12, for smaller hopping t the sequential tunneling threshold, determined by the energy distance of the states G and B, becomes very small for the chosen parameters and thus the Coulomb blockade almost disappears. Since there is no asymmetry in the system, not in the couplings nor in the energy levels, we do not expect and do not find regions of NDC and/or super-Poissonian noise. This is specific to this DQD system, in which there are only interfacial dots and thus there is always a finite probability for the electrons to depopulate the dot structure. In contrast, in chains of three and more quantum dots, super-Poissonian noise is possible even for a fully symmetric system. We will discuss this effect in the following chapter for a triple quantum dot with strong non-local Coulomb interactions.

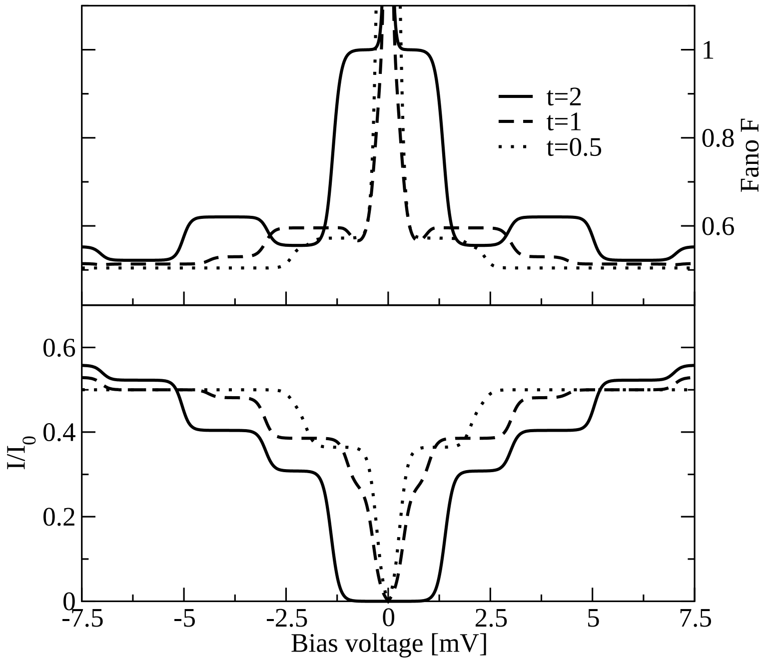

Figure 4.13: *Current I (absolute value) and Fano factor S vs. voltage for different values of "hopping" t without level detuning ($\varepsilon_{12} = 0$) for symmetric couplings and same parameters as in the situation depicted in Fig. 4.6. Note that current and Fano factor are both symmetric under the reverse of bias voltage, since there is no source of asymmetry.*

Note that although the current (Fano factor) does very much depend on the value of the hopping t for the low bias regime depicted in Fig. 4.13, the maximum current at very large bias (not shown) is actually independent of the hopping t. This is due to our neglect of off-diagonal matrix elements of the reduced density matrix. The effect of off-diagonal elements on transport are negligible for the weak coupling situation we consider, but become increasingly important, if the coupling Γ becomes comparable to the intrinsic energy scales of the dot system, such as the hopping energy t. Such off-diagonal elements have been included in recent works [88, 89].

4.3 Triple quantum dot

The main difference between a double quantum dot and longer chains of coupled quantum dots, such as a triple quantum dot is the existence of a middle dot that is only indirectly coupled to the reservoirs via the interfacial dots. The more complex electronic spectrum gives rise to interesting physical effects whose signatures can be found in the transport characteristics as we will see later in this chapter. All three dots are fully coherent among each other and weakly coupled to metallic electrodes via the dots at the interface, thus modeling a molecular wire. In the following we will discuss the current-voltage characteristics as well as the current noise which are evaluated up to first-order perturbation theory in the couplings to the electrodes.

4.3.1 Model and Hamiltonian

We consider a series of quantum dots, each with one spin-degenerate level. Including hopping between the dots as well as intra-dot and inter-dot (nearest neighbor) Coulomb interactions we arrive at the Hamiltonian

$$\hat{H}_{\text{dots}} = \sum_{i\sigma} \varepsilon_i n_{i\sigma} - t \sum_{i \neq j, \sigma} (c^\dagger_{i\sigma} c_{j\sigma} + h.c.) + U \sum_i n_{i\uparrow} n_{i\downarrow} + U_{nn} \sum_{i \neq j, \sigma, \sigma'} n_{i\sigma} n_{j\sigma'}, \qquad (4.5)$$

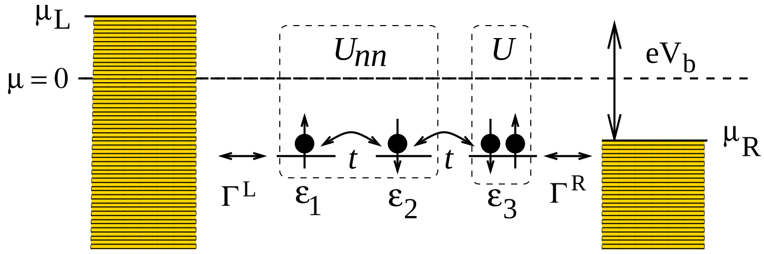

Figure 4.14: *The considered chains of dots and the relevant energies scales.*

The equilibrium chemical potential of the leads (Fermi energy) sets the zero of the energy scale. The "artificial molecule" term $\hat{H}_{\text{dots}}$ describes the series of dots with Fermi operators $c^\dagger_{i\sigma}$, $c_{i\sigma}$, on-site energies ε_i and nearest neighbor hopping t. U and U_{nn} are the strength of the intra-dot and nearest neighbor inter-dot Coulomb repulsion.

In the following we discuss current and shot noise for a model of type Eq. 4.5 with $N = 3$ dots and a half filled ground state (i.e. one electron per dot). We use equal couplings, $\Gamma^L_1 = \Gamma^R_3 = 2.5\,\mu$eV, so $\Gamma = \Gamma^L_1 + \Gamma^R_3 = 5\,\mu$eV. Our perturbation expansion is valid for temperatures much larger than the tunnel couplings. We choose $k_B T = 5\,\Gamma = 0.025\,$meV which corresponds to $T \approx 0.25$K. The dot system is characterized by the level energy ε, the intra-dot 'Hubbard' repulsion U and the nearest neighbor charge repulsion U_{nn}, which we present in units of meV. Transport is achieved by applying a bias voltage V_b, which is dropped symmetrically and entirely at the electrode-dot tunnel junctions, meaning that the energies of the dot states are independent of the applied voltage. We do not consider here the effects of asymmetric or incomplete voltage drops that are straightforward to anticipate.

We point out that the three dot system is the simplest system that is not pure interface and therefore is the minimal model for a truly non-local "artificial molecule". After diagonalizing the central Hamiltonian we obtain the eigenstates that split into singlets, doublets, triplets, etc.. The obtained electronic wavefunctions are much more complex than in the discussed case of the double quantum dot. As a consequence states which are mainly "localized" at the interfacial dots are competing in transport with states that have their main weight at the middle dot (even though the Hamiltonian remains fully left ↔ right symmetric). This competition can have dramatic effects in the noise characteristics that have no equivalent for smaller systems.

4.3.2 Influence of strong non-local Coulomb interactions

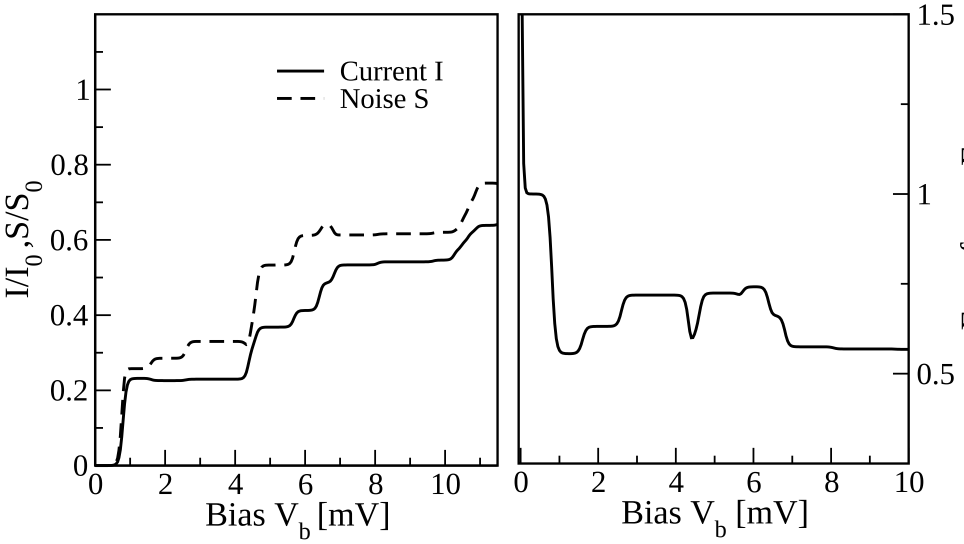

Figure 4.15: *Left panel: current I, shot noise S vs. bias voltage for a three-dot chain with $k_\mathrm{B}T = 0.025$, $\varepsilon = -10$, $t = 2$, $U = 12$ and $U_{nn} = 0.2$ (all energies in units of* meV*). Right panel: Fano factor is sub-Poissonian ($F < 1$) for all bias larger than the sequential tunneling threshold. All current and noise curves are normalized to $I_0 = (e/2\hbar)\Gamma \sim 60\,\mathrm{pA}$ and $S_0 = (e^2/2\hbar)\Gamma \sim 10^{-29}\mathrm{A}^2/\mathrm{Hz}$, respectively.*

We first consider a situation where the non-local interaction U_{nn} is small ($U_{nn} = t/10$) and obtain the typical behavior for a fully symmetric system, see left panel of Fig. 4.15. The current rises (mostly) monotonically in steps, the noise also shows steps, but must not increase monotonically. Thermally broadened peaks around the steps are also possible. The Fano factor $F = S/2eI$ will fall between values of 1 (Poissonian noise) and 1/2 for biases larger than all excitation energies (symmetric double barrier noise), though in general it will not fall with a monotonous dependence on bias. At small bias, $eV_b \ll k_BT$, the noise is dominated by thermal noise, leading to a divergence [38] of the Fano factor.

If now the non-local Coulomb repulsion U_{nn} is increased so that $U_{nn} > t$ the situation

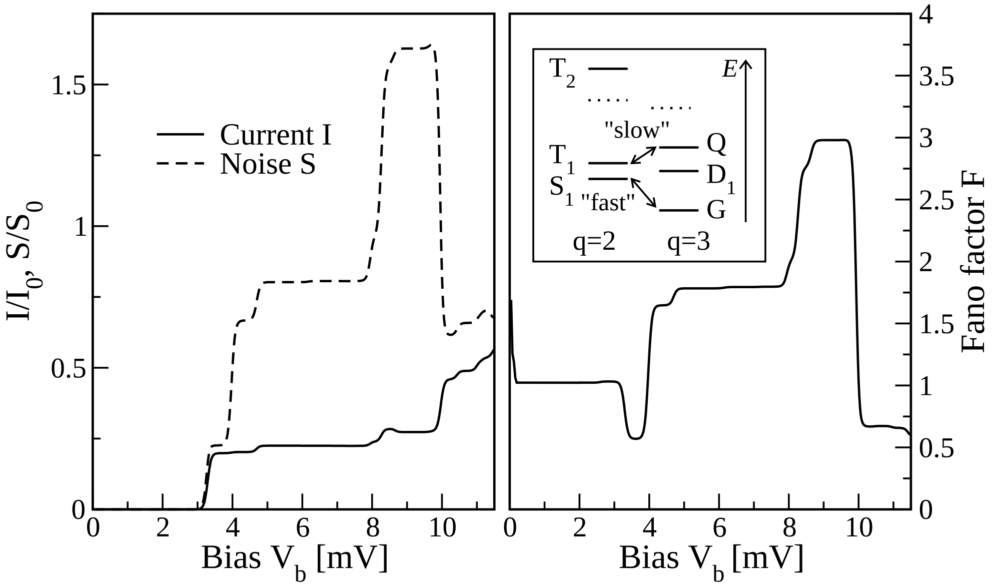

Figure 4.16: *Current* I *and shot noise* S *vs. voltage for three dots* $k_\mathrm{B}T = 0.025$, $t = 2$, $\varepsilon = -10$, $U = 12$, $U_{nn} = 5$. *The noise is strongly enhanced in absolute magnitude above* $V_b \sim 4\,\mathrm{mV}$, *while the current only slightly increases, leading to a Fano factor* $F > 1$. *This is due to a competition of "fast" and "slow" transport channels. Above* $V_b \sim 10\,\mathrm{mV}$ *"normal" behavior resumes, as the "slow" channel of transport is "cut short" (see text). The noise scales like* $(U_{nn}/t)^2$ *in this regime, while the current saturates as* t *is lowered.*

is quite different. In Fig. 4.16 we show current, noise and Fano factor for the same parameters as for Fig. 4.15 except for a different $\varepsilon = -10$. The current shows generic behavior, i.e. stepwise increase and only a tiny NDC around $V_b = 8.5$mV. The noise, however, is tremendously enhanced, with the Fano factor $F > 1$ indicating its super-Poissonian nature. While $F > 1$ in itself is not uncommon in the sequential tunneling regime as we have seen in the previous chapter for the case of the double dot and also in other works [26, 60, 100], often $F > 1$ is achieved by a suppression of transport in which the current is more suppressed than the noise. Here, the current is not suppressed, but the noise itself is enhanced in absolute magnitude over a large bias range, before recovering "normal" behavior beyond a bias of $V_b = 10\,\mathrm{mV}$.

For such a noise behavior strong electron interactions ($U, U_{nn} \gg T$) are needed to have the various states compete in transport. The outcome of this competition is determined by the wave functions of the competing states that effectively generate state dependent tunneling transition rates. Finally, the total spin of the states in question can differ by more than the electron spin 1/2 , so some energetically and spatially possible transition rates vanish due to spin selection rules. In the present case, the dominance of the non-local interaction U_{nn} over the hopping t, leads to a strong modification in the spatial distribution of the relevant many-body wave functions as compared to the $U_{nn} \ll t$

case.

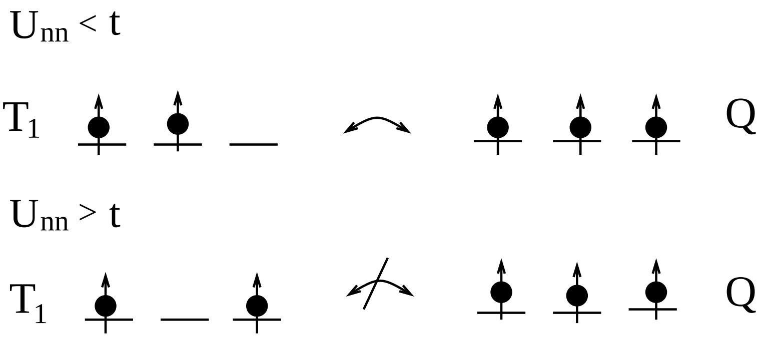

Figure 4.17: *Electronic tunnel processes change between the triplet state T_1 with charge $q = 2$ and the excited quadruplet state Q with charge $q = 3$ for the case of weak ($U_{nn} < t$) and strong non-local Coulomb ($U_{nn} > t$) interactions. The triplet wavefunction has two electrons on two different dots. In the case of strong non-local Coulomb interactions the dominant contribution of the triplet wavefunction consists of two electrons on the outer interfacial dots. Due to this change in the nature of the wavefunction tunneling processes leading into the quadruplet state are suppressed (as indicated in the figure).*

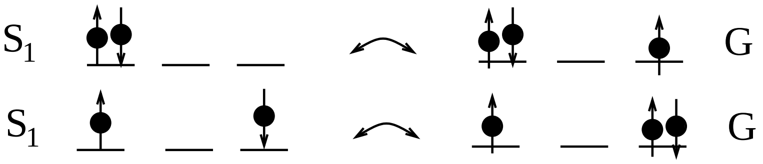

Figure 4.18: *Electronic transitions between the singlet S_1 and the doublet ground state G. Transitions involving local singlets (upper state in the figure) as well as some of the non-local singlet transitions (lower one in this figure) are unaffected by the ratio U_{nn}/t.*

Let us consider the nine states with total spin 1 in the $q = 2$ charge sector that split into three triplets (only T_1,T_2 shown in the insert of Fig. 4.16). If $U_{nn} << t$, the lowest triplet (T_1) will have equal electron occupation on any of the three dots, thereby maximizing the kinetic energy. On the other hand, if $U_{nn} > t$ it prefers to have one electron each on the leftmost and the rightmost dot, thus minimizing both intra-dot and inter-dot Coulomb repulsion. This change in the nature of the lowest triplet wave function is crucial for the "noisy" transport and is qualitatively depicted in Fig. 4.17. An equally fundamental role plays the total spin 3/2 quadruplet, the second excited state in the $q = 3$ charge sector that has one electron on each dot. Due to spin selection rules these quadruplet states can only have tunneling transitions to the triplet states of the $q = 2$ (or $q = 4$) charge sectors. The transitions involving the triplet state T_1 are depicted for the case of weak and strong non-local Coulomb interactions in Fig. 4.17.

The transition from the triplet state T_1 to the quadruplet Q requires an extra electron on the middle dot. However, since tunneling can only occur at the interface dots, this is suppressed by a factor $\sim (t/U_{nn})^2$, thus forming a "slow" channel of transport. In contrast, transitions from the q=3 doublet states G, D_1 to the $q = 2$ singlet S_1 can occur via "intermediate" local singlets on the dots that exist for finite U, independent of the ratio t/U_{nn}. These transitions are depicted in the upper part of Fig. 4.18. They remain "faster" than the ones involving the triplet and quadruplet states as shown in Fig. 4.17. Hence the current effectively alternates between fast and slow tunneling sequences which leads to enhanced noise in the corresponding bias regime [94, 101]. If we take the on-site repulsion U to infinity, local singlets are eliminated. Then, the S_1 singlet transitions are also suppressed by $(t/U_{nn})^2$ and the noise will turn (sub)-Poissonian.

In Fig. 4.16, on the first plateau for $3.3\,\mathrm{mV} < V_b < 4\,\mathrm{mV}$ with sub-Poissonian noise, transport is mainly achieved by tunneling events in which the dot system alternates between the ground state G with charge $q = 3$, and the lowest singlet S_1 with charge $q = 2$. The states S_1 and the lowest triplet T_1 ($q = 2$) are only split by the small "exchange energy" of size $J \sim t^2/U \sim 0.33\,\mathrm{meV}$ and the first excited doublet D_1 ($q = 2$) falls energetically in between S_1 and T_1, see the inset in the right panel of Fig. 4.16. Therefore, as soon as the sequential tunneling threshold $V_{\mathrm{seq}} = 2(E_{S_1} - E_G)/e \sim 3.3\mathrm{mV}$ is overcome, the states T_1 and D_1 also participate in transport, but their occupation turns out to be small (less than 1 percent). Since $V_{\mathrm{seq}} > 2(E_Q - E_{T_1})/e$ even the quadruplet Q is occupied, though with the same low probability as the triplet T_1. However, above $V_b = 2(E_{T_1} - E_G)/e = 4\mathrm{mV}$ the transport becomes noisy, with a Fano factor of $F > 1$. However, the current itself still increases by about 2 percent (not visible in the figure). When direct transitions between the ground state G and lowest triplet T_1 become possible, the occupation in T_1, D_1 and Q increases at the cost of G and S_1, until each state has equal probability. Due to their larger spin multiplicity this means that the triplet and the quadruplet states compose about 7/12 of the total probability.

For even larger bias, states in the $q = 4$ charge sector come into play, which lead to several smaller features, until at about $V_b = 8\mathrm{mV}$ the quadruplet becomes even more occupied via the lowest triplet in the $q = 4$ charge sector and the noise and the Fano factor reach their maximum. The maximum value of noise (and Fano factor) behaves as $(U_{nn}/t)^2$, meaning that huge Fano factors can be achieved. The current value at the corresponding plateau saturates as the hopping t is decreased. This is due to the homogeneity of our Hamiltonian. "Detuned" dot levels ε will lead to a decrease in current with decreasing t [28]. The size of t, however, is constraint by $t \gg \Gamma^r$, as otherwise the division of the total system into a coherent dot system with perturbative coupling to electrodes makes no sense.

At $V_b = 10\,\mathrm{mV}$ transitions between the quadruplet and the second triplet (T_2) with

$q = 2$ become possible. In contrast to the lowest triplet T_1, the states of T_2 (as well as the quadruplet states) do not benefit from the hopping t, therefore the structure of their wave functions is independent of both the interactions U, U_{nn} and the hopping t, only the actual energy varies ($E_{T_2} = 2\varepsilon + U_{nn}$, $E_Q = 3\varepsilon + 2U_{nn}$). T_2 is spread uniformly over the three dots, so its transition rate with the quadruplet is not suppressed with t/U_{nn}. Therefore, the slow channel between the T_1 triplet and the quadruplet is "cut short", the transport becomes more homogeneous and the Fano factor drops below unity.

As the above effect relies on spin quantum numbers it should be robust to standard relaxation processes involving phonon and photon emission. A strong magnetic field will modify the details, but not the generic behavior of the transport. Also co-tunneling does not modify the effect. We have calculated the described systems in a full second order description and found the same strongly enhanced noise behavior. Deviations are seen at the step positions for current and noise due to the additional broadening in second order, which is proportional to the coupling constant Γ and the temperature T. We will elaborate more on these features in the following chapter 5 where co-tunneling processes will be discussed.

While we considered parameters such that the $q = 3$ and $q = 2$ charge sectors participate in transport at the first plateaus we could achieve the same effect by applying a gate voltage such that the charge sectors with $q = 3$ and $q = 4$ are involved. Although the details of how each state exactly contributes to the transport at a given bias are changed, the main mechanism (the slow triplet-quadruplet channel) to the enhanced noise stays the same. In the case of weak Coulomb interactions, i.e. $U_{nn} \ll t$, a similar spatial distribution of the lowest triplet wave function can be achieved by raising the level position ε_2 of the middle dot more than the inter-dot hopping t above the onsite energy ε of the interfacial dots. However, such a level detuning will strongly reduce both current and shot noise, similar to the "local" models of Refs. [26, 60]. In the Coulomb blockade region and close to the sequential tunneling threshold we often find super-Poissonian noise. This enhancement is due to the thermal occupation and following sequential depletion of excited states that lead to small cascades of tunneling events interrupted by long (Coulomb) blockages, resulting in a noisy current. The effect has been discussed in the previous section where we have analyzed the transport characteristics of a double quantum dot in the Coulomb blockade.

4.4 Summary

Let us summarize the main findings as discussed in this chapter in the following. We have discussed sequential transport in non-local, coupled quantum dots with a strong inter-dot coupling and weak coupling to the leads. We account for the non-local electronic wavefunction of the electrons and discuss two systems, firstly a double quantum dot and secondly a triple quantum dot. In the case of the double quantum dot we discussed transport within the Coulomb blockade as well as for the high bias regime where excited states are involved in transport. We found that the behavior of the shot noise in the Coulomb blockade is directly related to the underlying low energy spectrum of the DQD system. The spectrum is characterized by two intrinsic energy scales, the sequential tunneling energy ε_{seq} and the first vertical excitation energy out of the ground state, ε_{co}. For a symmetric system in the Coulomb blockade we distinguished between three scenarios: i) For a first vertical excitation energy that is smaller than twice the sequential tunneling energy $\varepsilon_{co} > 2\varepsilon_{seq}$ the Fano factor (noise) is always sub-Poissonian, i.e. $F < 1$, as sequential processes start before excited states come into play, ii) if $\varepsilon_{seq} < \varepsilon_{co} < 2\varepsilon_{seq}$ thermally activated sequential transport leads to super-Poissonian Fano factors in the bias range $2(\varepsilon_{co} - \varepsilon_{seq})/e < V < 2\varepsilon_{seq}/e$, iii) for the case $\varepsilon_{co} < \varepsilon_{seq}$ the Fano factor remains super-Poissonian in the entire Coulomb blockade regime. Our findings are valid for arbitrary ground state charges and also apply to larger systems with more than two coupled dots, as they depend only on the above mentioned generic energy scales of the interacting dot system.

For a bias above the sequential tunneling threshold we discussed different types of asymmetries in the system realized by either asymmetric couplings to the electrodes or by detuning the quantum dot levels out of resonance with each other. For asymmetric dot-electrode couplings we obtained asymmetric current-voltage characteristics as has been observed in experiments before. For very strong asymmetry negative differential conductance and super-Poissonian noise with Fano factors $F > 1$ can develop. These features develop at the same energy positions, i.e. at the same bias voltage for any asymmetry ratio Γ_L/Γ_R since the DQD spectrum remains unchanged. In contrast detuning the dot levels out of resonance also leads to NDC and super-Poissonian noise for sufficiently strong asymmetry, but now at voltages that depend on the strength of the asymmetry as the DQD spectrum is changed. These features only appear for one bias direction, $V < 0$ or $V > 0$, depending on which coupling Γ_r (with $r = R, L$) is suppressed or which quantum dot has a lower level energy. Furthermore, we found that at a fixed detuning ε_{12} the current is reduced with decreasing inter-dot hopping t. The latter results in a stronger localization of states on individual dots similar to the case of strongly detuned quantum dots. Therefore a weaker inter-dot hopping and a stronger detuning at fixed inter-dot hopping may cause similar transport characteristics.

In the case of longer chains of quantum dots we discussed a triple quantum dot with symmetric couplings. If the non-local Coulomb interactions dominate over the inter-dot hopping the shot noise is greatly enhanced *in absolute magnitude* over a wide range of parameters above the sequential tunneling threshold. As there is no simultaneous enhancement of the tunneling current, the shot noise becomes super-Poissonian. In contrast to earlier work this is achieved even in a fully symmetric system. The origin of this novel behavior lies in a competition of ”slow” and ”fast” transport channels that are formed due to the differing non-local wave functions and total spin of the states participating in transport. An enhancement factor of ~ 100 can be easily achieved. This should be of special importance to experimentalists since usually a major challenge is the detection of the real shot noise over the background 1/f-noise (as explained in chapter 2) caused by fluctuations in the physical environment and measurement equipment. Therefore the strong enhancement may allow direct experimental detection of shot noise in a chain of lateral quantum dots.

Chapter 5

Co-tunneling transport

We have seen in the previous chapter that transport in a weak coupling regime is well described in a sequential tunneling picture. However, if we want to move to stronger coupling situations, where the coupling is of the order of temperature (i.e. $\Gamma \approx k_B T$) we have to account for higher order processes such as co-tunneling involving the simultaneous tunneling of two electrons at a time. Electron co-tunneling has been the subject of a considerable large number of experimental [29, 69, 102] and theoretical works [58, 91, 103]. It is known to be the dominant transport process within the Coulomb blockade but also effects transport above the sequential transport threshold in particular at the resonances where an additional current channel opens. In general higher order processes modify the electronic transport in comparison to the sequential transport picture in two ways: First an additional broadening of the current and noise steps which is comprised by the sum of the temperature $k_B T$ (as present in first order calculations) and by the coupling strength Γ is introduced [33]. Second it provides a current and noise contribution in the Coulomb blockade that is not exponentially suppressed. Both quantities, current and shot noise, depend very sensitively on the low energy spectrum of the quantum dot or molecular system in that regime and thus allow for a spectroscopic study, particular in the Coulomb blockade.

In the following chapter we will discuss co-tunneling effects in transport. We introduce the two types of co-tunneling processes, elastic and inelastic co-tunneling in section 5.1. Next in section 5.2 we will discuss the Anderson model with an emphasis on transport in the Coulomb blockade. We show how details of the energy spectrum can be extracted from the current and noise behavior. Finally, we focus in section 5.3 on transport through a two level quantum dot which can not be exactly mapped on the spin split single level Anderson model. We account for an additional gate electrode and study the conductance as well as the Fano factor vs. the applied bias and gate voltage. Specifically, we discuss the characteristic width and height of the observed co-tunneling features. Furthermore, we concentrate on the interesting regime of co-tunneling assisted sequential tunneling and finally close with short summary and outlook on co-tunneling transport in larger mesoscopic systems.

5.1 Elastic and inelastic co-tunneling processes

In the Coulomb blockade where sequential transport is exponentially suppressed co-tunneling processes are possible via the occupation of virtual intermediate states. Depending on whether or not the process requires some energy (in form of the applied bias) one speaks of elastic or inelastic co-tunneling. Fig. 5.1 shows an elastic co-tunneling process. An electron tunnels from the left lead into a virtual dot state (the term "virtual" indicates that for a short timescale energy conservation is violated) and then into the right lead. Elastic co-tunneling processes are present at arbitrary bias (also at equilibrium) since no energy is required. In contrast, if a finite bias is applied an electron can tunnel into a virtual dot state and subsequently another electron that

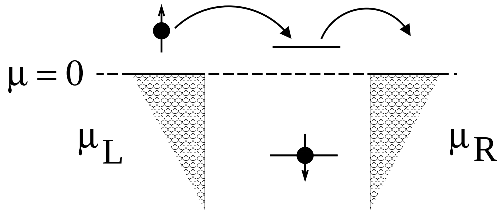

Figure 5.1: *Sketch of an elastic co-tunneling process through a two level quantum dot without any bias applied. The intermediate, virtual state in the depicted process is the doubly occupied state.*

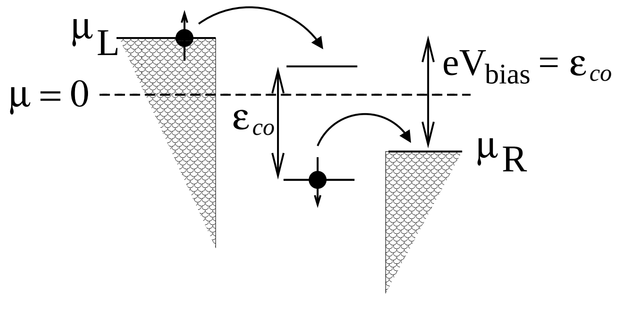

Figure 5.2: *Sketch of an inelastic co-tunneling process through a two level quantum dot. The bias applied is not sufficient for a sequential tunneling process but allows for inelastic co-tunneling. When the dot is left in an excited state after such a process, an inelastic co-tunneling process might be followed by a sequential process (see also co-tunneling assisted sequential tunneling in chapter 5.3.4.)*

initially occupied a lower dot energy level tunnels out of the dot. The energy required for such a process must hence be equal to the energy splitting of the two dot levels involved in the inelastic process. Fig. 5.2 depicts the described inelastic co-tunneling process in which the dot is left in an excited state. Depending on the applied bias and dot's low energy spectrum an inelastic co-tunneling process can be followed by a sequential tunneling process. This scenario is referred to as the co-tunneling assisted sequential tunneling regime which we will discuss in some detail in chapter 5.3.2.

5.2 Single level Anderson model

5.2.1 Hamiltonian

For the single-level Anderson impurity model our dot Hamiltonian reads

$$H_{\mathrm{D}} = \sum_{\sigma} \varepsilon_\sigma c_\sigma^\dagger c_\sigma + U n_\uparrow n_\downarrow \tag{5.1}$$

where we have used the compact notation $(c_{i\sigma} = c_\sigma, \varepsilon_{i\sigma} = \varepsilon_\sigma, n_{i\sigma} n_{i\sigma'} = n_\uparrow n_\downarrow)$ for a single level $i = 1$. The above Hamiltonian describes a single spin-dependent energy level with a Zeeman splitting Δ due to an external magnetic field yielding level energies of $\varepsilon_\downarrow = \varepsilon - \frac{\Delta}{2}$ and $\varepsilon_\uparrow = \varepsilon + \frac{\Delta}{2}$. Interaction effects are included by the second term, where U is the Coulomb interaction on the island with $n_\uparrow, n_\downarrow$ being the number operator for electrons with corresponding spin. Bosonic effects are excluded for the moment. For the coupling parameters we drop the spin dependence and write $\Gamma_r^{i\sigma} = \Gamma_r$ with $r = R, L$.

5.2.2 Coulomb blockade spectroscopy

In the following we will discuss four different transport regimes that are defined according to the dot's individual low energy spectrum. A summary of these four regimes

Regime	Condition
I	$\varepsilon_{co} > 2\ \varepsilon_{seq}$
II	$2\ \varepsilon_{seq} > \varepsilon_{co} > \varepsilon_{seq}$
III	$\varepsilon_{seq} > \varepsilon_{co} > \frac{2\varepsilon_{seq}}{3}$
IV	$\frac{2\varepsilon_{seq}}{3} > \varepsilon_{co}$

Table 5.1: *Four different transport regimes defined by their individual relations of the sequential tunneling energy threshold ε_{seq} to the inelastic co-tunneling excitation energy ε_{co} for the case of a symmetrically applied bias voltage.*

can be found in table 5.1. In the following discussion the bias is always dropped symmetrically, i.e. $\mu_L = -\mu_R = eV_b/2$. We start with a system in regime I corresponding to parameters $\varepsilon = 1, U = 8, \Delta = 6$ and $k_BT = 2\Gamma = 0.02$ (all units in meV). The choice of our parameters results in a singly occupied ground state (with spin down), an inelastic co-tunneling excitation energy of $\varepsilon_{co} = \Delta = 6$ and a sequential tunneling energy of $\varepsilon_{seq} = 2$. Regime I corresponds to a spectrum in which $\varepsilon_{co} > 2\varepsilon_{seq}$ and has

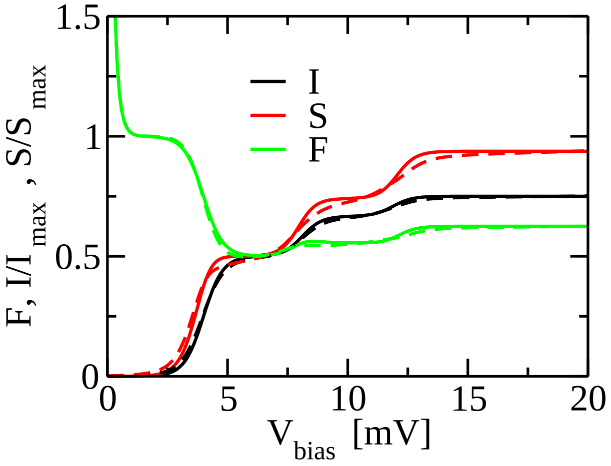

Figure 5.3: *Current, shot noise and Fano factor (parameters see text) in regime I where* $\varepsilon_{co} > 2\varepsilon_{seq}$. *Normalization factors are* $I_{max} = e\Gamma/2\hbar$ *and* $S_{max} = e^2\Gamma(2\hbar)$. *The solid lines correspond to first order results whereas the dashed lines show the second order calculation. The Fano factor is Poissonian in the Coulomb blockade and drops to sub-Poissonian values for biases above the sequential tunneling threshold.*

been encountered previously when first order (sequential) transport was discussed in a double quantum dot (see chapter 4.2.). Fig. 5.3 depicts the current, shot noise and Fano factor vs. bias for regime I in a first and second order transport picture. The current and noise rise in a step wise manner defined by the single particle excitation energies of the dot. In first order the steps are only broadened by temperature whereas in second order the temperature as well as the coupling Γ define the step width. Since the sequential tunneling threshold is reached before inelastic co-tunneling processes set in, no characteristic energy scale is introduced in the Coulomb blockade region. After a divergent behavior for very low biases (corresponding to the thermal noise limit) the Fano factor becomes Poissonian for biases below the sequential tunneling threshold indicating that the current is mainly due to one single type of process, namely elastic co-tunneling. For large bias sub-Poissonian Fano factors are resumed. Next we discuss regime II which is characterized by the parameters $\varepsilon = -1, U = 8, \Delta = 4$ and $k_BT = 2\Gamma = 0.02$ (all units in meV). Again this choice results in a singly occupied ground state, an inelastic co-tunneling excitation energy of $\varepsilon_{co} = \Delta = 4$ and a sequential tunneling energy of $\varepsilon_{seq} = 3$. Hence regime II has a low energy spectrum with

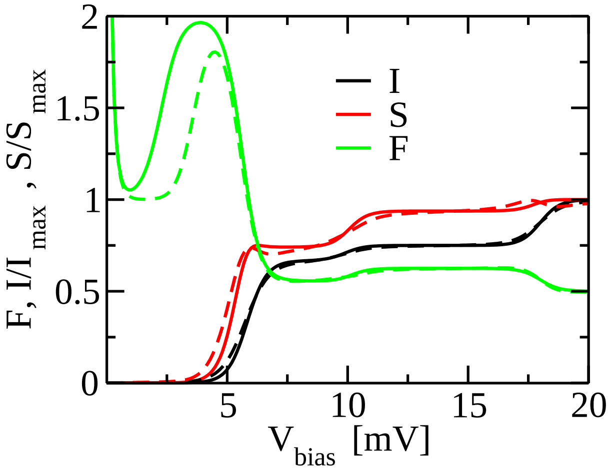

Figure 5.4: *Current, shot noise and Fano factor (parameters see text) in regime II where* $2\varepsilon_{seq} > \varepsilon_{co} > \varepsilon_{seq}$ *. The solid lines correspond to first order results whereas the dashed lines show the second order calculation. In first order the Fano factor becomes super Poissonian* ($F > 1$) *in the Coulomb blockade at an energy scale* $V_b = 2 \mid \varepsilon_{seq} - \varepsilon_{co} \mid$ *whereas in second order this happens at an energy scale* $V_b = \varepsilon_{co}$. *For biases above the sequential tunneling threshold the Fano factor drops to sub-Poissonian values in both cases.*

$2\varepsilon_{seq} > \varepsilon_{co} > \varepsilon_{seq}$.
For very low bias ($eV_B << k_B T$) and deep in the Coulomb blockade the Fano factor shows first divergent behavior due to thermal noise until it reaches a Poissonian value of $F = 1$ when elastic co-tunneling processes dominate (see Fig. 5.4). However, even in the first order calculation the Fano factor becomes super-Poissonian at a bias $V_b = 2 \mid \varepsilon_{seq} - \varepsilon_{co} \mid$. The mechanism behind is the same as discussed earlier in chapter 4.2. in the case of the double quantum dot. Rare thermal processes lead to a finite probability to occupy the excited state with one electron and upside spin although the bias does not suffice to do the same via a sequential tunneling process. Once the state with one single electron with spin up is occupied the dot can be depopulated by a subsequent fast sequential process leading into the empty state. The co-existence of these two processes on different time scales, a thermal occupation and a sequential depletion of an excited dot level leads to the enhanced super Poissonian noise feature in first order.

In second order the rare thermal processes become negligible since elastic and at higher bias also inelastic co-tunneling events dominate the transport picture. After the thermal regime the Fano factor is Poissonian due to elastic co-tunneling and becomes super-Poissonian when in addition inelastic co-tunneling processes become possible at a bias $V_b = \varepsilon_{co}$ which can be clearly seen in Fig. 5.4. A further decrease in the on-site energy levels such that $\varepsilon = -2.5, U = 8, \Delta = 6$ (all units in meV) leads us to regime III.

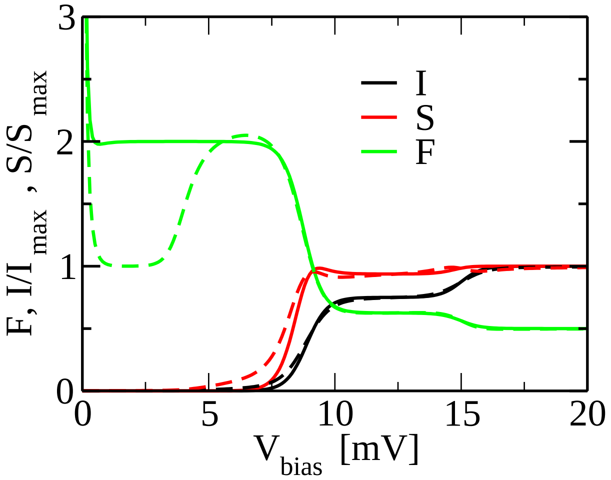

Figure 5.5: *Current, shot noise and Fano factor (parameters see text) in regime III where* $\varepsilon_{seq} > \varepsilon_{co} > \frac{2\varepsilon_{seq}}{3}$. *In first order the Fano factor remains super- Poissonian* ($F > 1$) *in the entire Coulomb blockade regime. However in second order elastic co-tunneling processes lead to a Poissonian Fano factor for biases below the inelastic co-tunneling excitation energy* ε_{co} *at which the Fano factor becomes super-Poissonian.*

Still our ground state is singly occupied. We obtain an inelastic co-tunneling excitation energy of $\varepsilon_{co} = \Delta = 4$ and a sequential tunneling energy of $\varepsilon_{seq} = 4.5$. This results in a low energy spectrum with $2\varepsilon_{seq} > \varepsilon_{co} > \frac{2\varepsilon_{seq}}{3}$. Fig. 5.4 shows that in second order the behavior in the Coulomb blockade is the same as in regime II. However, in first order the Fano factor now remains super-Poissonian in the entire Coulomb blockade. This behavior has been observed in [34, 61]. Note that in both regimes II and III an inelastic co-tunneling process can immediately be followed by a sequential depletion of the dot at the same bias $V_b = \varepsilon_{co}$. The combination of this second order (co-tunneling) and first order (sequential) process is referred to as co-tunneling assisted sequential tunneling. It follows that here the two processes can not be energetically separated and thus only one characteristic energy scale, namely ε_{co} is introduced in the Coulomb blockade. We now change to the last regime IV which is qualitatively different in comparison to the three regimes I-III discussed until here. Using the parameter set $\varepsilon = -6, U = 12, \Delta = 2$ (all units in meV) regime IV fulfills the relation $\varepsilon_{co} < \frac{2\varepsilon_{seq}}{3}$. This ensures that inelastic co-tunneling is clearly separated from co-tunneling assisted sequential tunneling. Hence two energy scales marking the onset of the two different transport processes should be observable. As mentioned earlier in the discussion of different perturbation schemes (see chapter 3.5.2) the standard perturbation scheme is not appropriate in all transport situations. Particularly it may break down deep in the Coulomb blockade. For regime IV the standard scheme indeed produces negative and thus unphysical probabilities. Therefore we use the *crossover* scheme which is valid from very low biases (nearly zero)

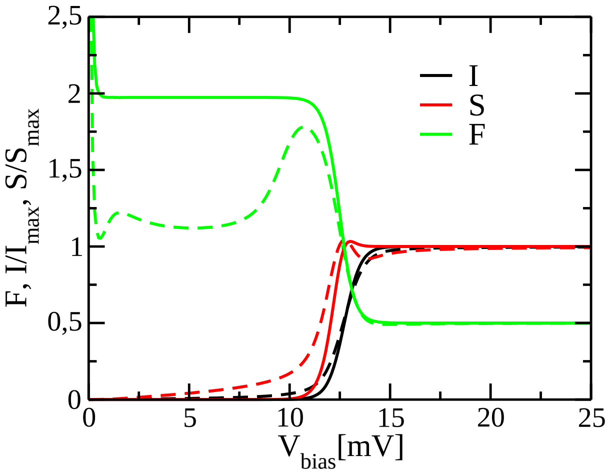

Figure 5.6: *Current, shot noise and Fano factor (parameters see text) in regime IV where* $\varepsilon_{co} < \frac{2\varepsilon_{seq}}{3}$*. In first order the behavior of the Fano factor is the same as in regime III. In second order a first energy scale is introduced when inelastic co-tunneling processes set in at* $\varepsilon_{co} = 1$ *and cause a super-Poissonian Fano factor. In addition the noise enhancement becomes even stronger with even higher Fano factors when co-tunneling assisted sequential tunneling processes become possible at a bias* $V_b = 2|\varepsilon_{co} - \varepsilon_{seq}|$.

up to the large bias regime where all excitation energies have entered into the applied bias window. In a first order calculation regime IV displays the expected behavior of a constant super-Poissonian plateau in the Fano factor (see Fig. 5.6). Second order transport gives a totally different picture. The Fano factor becomes super-Poissonian for the first time when the inelastic co-tunneling energy is reached. When co-tunneling assisted sequential tunneling processes become applicable at the corresponding bias the noise (Fano factor) is increased further to even higher values. The noise's (Fano factor's) maximum is reached at a bias $V_b = 2|\varepsilon_{co} - \varepsilon_{seq}|$. Note that the two energy scales can not be seen by looking at the current or conductance (not shown here) alone. While in the inelastic co-tunneling regime a small increase in form of a shoulder can be observed in the conductance the co-tunneling assisted sequential tunneling regime is not visible for the parameters specified for Fig. 5.6.

The discussion above suggests that only by studying the current in combination with the shot noise one is able to extract useful information about the nanostructure's low energy spectrum. The most interesting regimes for that purpose are regimes II, III and IV which we will study in the next section in the case of a two level quantum dot.

5.3 Two level quantum dot

In this chapter we focus again on our model of a two level quantum dot (Fig. 4.1). Studying the system in second order shows a much richer physical behavior. Note that the two level quantum dot which includes the spin of the electrons can not be exactly mapped onto the single level spin split Anderson model discussed in the previous chapter 5.2 since the states with two electrons now split into singlet (S=0) and triplet states (S=1).

5.3.1 Hamiltonian

The central Hamiltonian reads

$$H_{\mathrm{D}} = \sum_{i\sigma} \varepsilon_{i\sigma} c^{\dagger}_{i\sigma} c_{i\sigma} + U \sum_{i} n_{i\uparrow} n_{i\downarrow} + U_{nn} \sum_{i\neq j,\sigma,\sigma'} n_{i\sigma'} n_{j\sigma} \tag{5.2}$$

with $i = 1, 2$ denoting the quantum dot levels. For an explanation of the various terms we refer the reader to chapter 4.1.1. Here we have written the dot Hamiltonian in a slightly different way. The term containing the charging energy E_C is replaced by an explicit inter-orbital Coulomb interaction U_{nn}. Furthermore we account for a gate voltage that affects the electrostatic potential of the dot levels in the form $\varepsilon_\chi \to \varepsilon_\chi + V_G \cdot N_\chi$ where ε_χ denotes the energy and N_χ the total number of electrons in the state $|\chi\rangle$.

5.3.2 Conductance and noise in the Coulomb blockade

In an intermediate coupling situation where the coupling is of the order of temperature ($\Gamma \approx k_B T$) features of higher order transport become important. Throughout the following discussion we choose $k_B T = 2\Gamma$ which is still in the “weak” coupling limit in the sense that a perturbative expansion in the coupling constant Γ is appropriate. On the other hand the coupling strength is strong enough such that second order processes significantly influence the transport characteristics. We begin with parameters $U = 20, U_{nn} = 4, \varepsilon_1 = -4, \varepsilon_2 = -2, k_B T = 2\Gamma = 0.04$ (all units in meV) which corresponds to regime II as described in chapter 5.2. Thereby we obtain an energy spectrum with a singly occupied ground state. In Fig. 5.7 we depict the differential conductance ($\partial I/\partial V$) vs. the applied bias and the gate voltage. The color-scale translates low conductance values with dark blue and high conductance values with red. The Coulomb diamond as well as two excitation lines outside the diamond structure

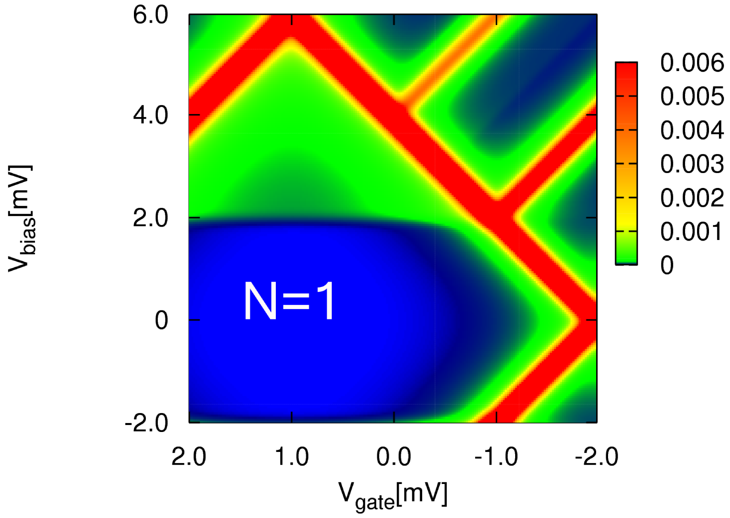

Figure 5.7: *Color-scale plot of the differential conductance (in units* $10 \cdot \pi e^2 \Gamma / h$*) vs. gate voltage (*$V_{gate}$*) and bias voltage (*$V_{bias}$*). The Coulomb diamond edges mark the onset of sequential tunneling. Lines outside the Coulomb diamond correspond to transport via excited states whereas the horizontal step inside the diamond is due to inelastic co-tunneling.*

are clearly visible. Inside the Coulomb diamond sequential transport is exponentially suppressed due to Coulomb blockade. Since elastic co-tunneling processes which are possible for arbitrary bias and gate voltage they do not introduce an energy scale inside the Coulomb diamond. When the bias is equal to the inelastic co-tunneling excitation energy inelastic co-tunneling processes become possible. The corresponding energy scale ε_{co} can be observed in the figure by the horizontal, gate voltage independent step at $V_{bias} = 2\,\text{meV}$. Below that step only elastic co-tunneling events provide a significant contribution to the current. For biases above the threshold ε_{co} both types of co-tunneling, elastic and inelastic exist. Note that also at the edge and outside the Coulomb diamond second order processes play an important role. For instance Fig. 5.7 would contain much more narrow excitation (red) lines if only first order transport was considered.

Next we want to discuss the noise properties of our system. Fig. 5.8 shows the Fano factor in the same voltage region as the conductance plot Fig. 5.7. At the Coulomb diamond edge and for biases above the sequential tunneling threshold the Fano factor drops to sub-Poissonian values $(0.5 < F < 1)$ as it would also be the case in a first order sequential transport description. Inside the Coulomb blockade we find two features. The first which is trivial is the horizontal gate voltage independent line at zero bias. Here the Fano factor is divergent corresponding to the thermal noise limit. For $V_{bias} >> k_B T$ the Fano factor becomes Poissonian again since there is only one transport process,

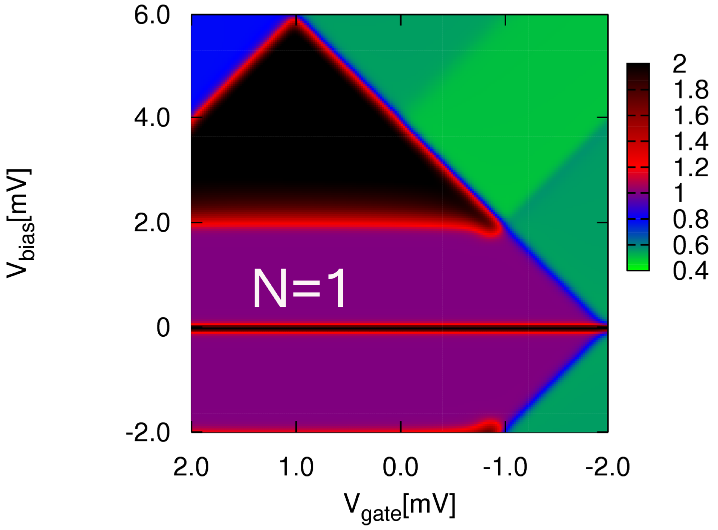

Figure 5.8: *Color-scale plot of the Fano factor vs. gate voltage (V_{gate}) and bias voltage (V_{bias}). Around zero bias voltage the Fano factor diverges according to the thermal noise behavior. It is then reduced to a Poissonian value of $F = 1$ indicating that elastic processes dominate for low bias. At the inelastic co-tunneling excitation energy it becomes super-Poissonian. The Fano factor is finally reduced to sub-Poissonian values when the Coulomb diamond edge is reached and sequential transport sets in.*

namely elastic co-tunneling present. Increasing the bias further allows for inelastic co-tunneling at $V_{bias} \geq 2\,\mathrm{meV}$. Now two types of co-tunneling processes with different tunneling rates coexist which leads to a noisier current with super-Poissonian Fano factors. Note that a vertical cut corresponding to a fixed gate voltage in Fig. 5.8 would yield a very similar transport picture as Fig. 5.4 in chapter 5.2 when we discussed parameter regime II of the Anderson model.

5.3.3 Scaling of the co-tunneling contributions

We are interested in the influence of the coupling strength and temperature of the observed co-tunneling features. Therefore we study the differential conductance of our system. The right panel of Fig. 5.9 displays a co-tunneling "shoulder" of the differential conductance at the inelastic co-tunneling excitation energy. An analysis of the shoulder height for different coupling strengths shows a linear dependence on the coupling Γ. Since we have normalized the current and hence also the diffential conductance by a factor Γ this means that the co-tunneling shoulder height scales with $\sim \Gamma^2$. The second derivative of the current as depicted in the left panel of the figure further proves this fact. The red solid curve multiplied by a factor $\frac{\Gamma_{black}}{\Gamma_{red}} = 2$ lies on top of the black solid curve resulting in the black, red dotted curve. We note that the height of the co-tunneling shoulder is further influenced by the value of the inelastic co-tunneling excitation energy ε_{co} itself. However, no general valid scaling behavior can be formulated for its dependence since the inelastic co-tunneling excitation energy can only be varied by changing internal parameters of our dot Hamiltonian $(U, U_{nn}, t, \varepsilon_i)$ and thereby the total spectrum.

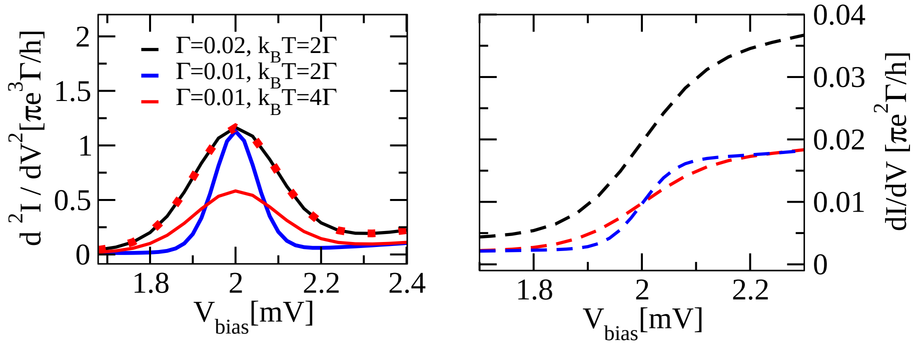

Figure 5.9: *Right panel: Differential conductance $\partial I/\partial V$ vs. bias voltage (V_{bias}) for the same parameter set as used in Fig. 5.7 and with a fixed gate voltage of $V_{gate} = 0\,\mathrm{meV}$. The coupling strength Γ and the temperature k_BT are varied. Left panel: Second derivative of the current $\partial^2 I/\partial V^2$ vs. bias voltage for different coupling strengths and temperatures.*

Next we want to consider the width of the shoulder. A comparison of the blue dashed curve with the red dashed curve in the right panel of Fig. 5.9, where both curves correspond to the same total coupling strength, shows a larger broadening for higher temperatures. Considering the second derivative of the current, the width of the blue curve with the lower temperature of $k_BT = 2\Gamma$ is only half of the width of the red curve corresponding to a temperature twice as much as the the one of the red curve. The reduction of the width of the inelastic co-tunneling shoulder to the thermal limit has also been observed in experiments [29].

5.3.4 Co-tunneling assisted sequential tunneling

If we change our parameter set to $U = 25, U_{nn} = 5$, $\varepsilon_1 = -4$, $\varepsilon_2 = -3.5$, $k_BT = 2\Gamma = 0.04$ (all units in meV) the dot spectrum is such that $\varepsilon_{co} < \frac{2\varepsilon_{seq}}{3}$. In this regime two energy scales are visible in the Coulomb blockade. One is the inelastic co-tunneling excitation energy which separates the regime of elastic from inelastic co-tunneling. The other corresponds to an energy scale associated with processes in which an inelastic co-tunneling event is followed by a sequential tunneling process of the excited dot electron. The latter is in principle a sequential energy scale and thus we expect it to be gate voltage dependent. Fig. 5.10 shows a conductance plot in the described regime showing part of the Coulomb diamond. As above, inelastic co-tunneling displays itself

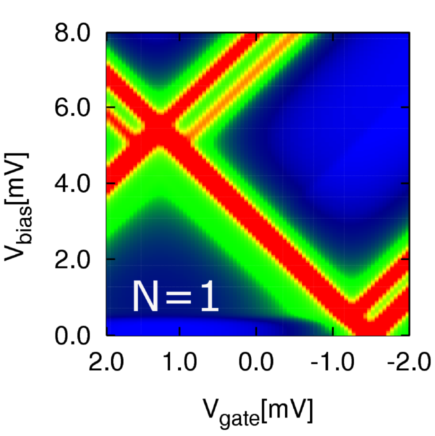

Figure 5.10: *Color-scale plot of the differential conductance $\partial I/\partial V$ in the regime where $\varepsilon_{co} < \frac{2\varepsilon_{seq}}{3}$. The horizontal step inside the Coulomb diamond corresponds to inelastic co-tunneling whereas the green inner triangle structure marks the co-tunneling assisted sequential tunneling regime.*

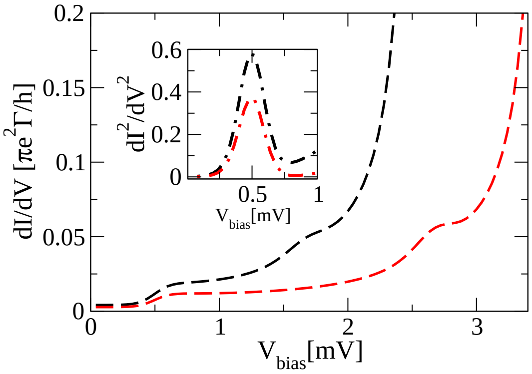

Figure 5.11: *First and second derivative of the current vs. bias voltage at two different gate voltages $V_g = 0\,\text{meV}$ and $V_g = 0.5\,\text{meV}$. The position of the second shoulder corresponding to co-tunneling assisted sequential tunneling is gate voltage dependent.*

in form of a horizontal line at a bias $V_{bias} = 0.5\text{meV}$ where transitions from the singly occupied ground state (which is the two-fold doublet state) to the first excited state (also a two-fold degenerate doublet state) in the same charge sector $N = 1$ become possible. The threshold for co-tunneling assisted sequential tunneling corresponds to the edge of the green triangle inside the Coulomb diamond. Theses processes occur via co-tunneling from the ground state to the first excited state with charge $N = 1$ followed by sequential tunneling processes from the excited state to the energetically lowest state in the neighboring charge sector which is $N = 2$ for negative gate voltage and $N = 1$ for positive gate voltage. In our system the lowest state with charge $N = 2$ is four-fold degenerate, consisting of three triplet states and one singlet state. The slope of the inner triangle is parallel to the Coulomb diamond edge since the gate voltage dependence of the co-tunneling assisted sequential tunneling energy scale is the same as for the sequential tunneling threshold $\varepsilon_{seq} = \varepsilon_{seq}(V_g)$.

For two fixed gate voltages the conductance traces are displayed in Fig. 5.11. The black (red) dashed curve is a vertical cut of Fig. 5.10 at zero (non-zero) gate voltage $V_g = 0\,\text{meV}$ ($V_g = 0.5\,\text{meV}$) respectively. A first co-tunneling shoulder is always found at the inelastic co-tunneling excitation energy ε_{co} whereas a second shoulder appearing approximately at $V_b = 2|\varepsilon_{co} - \varepsilon_{seq}|$ is gate voltage dependent. The second shoulder is shifted to higher bias voltages for positive gate voltages due to $\varepsilon_{seq}(V_g)$ as explained above.

Another effect of the gate voltage sweep is the variation of the differential conductance at the inelastic co-tunneling excitation energy ε_{co}. By applying a positive gate voltage the energies of the ground state and the first excited state are both equally lifted such that their splitting which is the inelastic co-tunneling excitation energy stays constant. However, the elastic co-tunneling processes enhance the conductance even at zero bias. This can be seen also in Fig. 5.11 where the black curve corresponds to a slightly higher differential conductance as the red curve at bias smaller than the inelastic co-tunneling excitation energy. Also the probability to occupy the lowest excited states via inelastic co-tunneling increases and thus leads to a higher differential conductance at ε_{co}.

The transport mechanism of co-tunneling assisted sequential tunneling has been demonstrated by experiment [6]. Here a lateral multilevel quantum dot was measured and triangles in the differential conductance inside the Coulomb blockade were frequently found. The authors applied a similar theoretical model based on a diagrammatic approach including second order diagrams and found qualitative agreement between the measured and calculated triangle inside the Coulomb blockade. However, only for one particular gate voltage the authors did theoretically show the existence of the two energy scales in the differential conductance. Furthermore the experimental curves showed triangle lines that joined lines outside the Coulomb diamond associated with transport through excited states. This feature was not shown theoretically in that work but can be clearly seen in Fig. 5.10.

As we know from the discussion of the Anderson model in section 5.1 some second order transport features might not be visible when one studies the conductance alone. We therefore study the noise and Fano factor behavior of our system in the considered regime. Fig. 5.12 shows the Fano factor of our two level quantum dot for the same bias and gate voltage window as displayed in Fig. 5.10. The inelastic co-tunneling excitation energy scale at $V_g = 0.5\,\mathrm{meV}$ as well as the triangle inside the Coulomb diamond are clearly seen. For transport outside the Coulomb blockade the Fano factor is reduced to sub-Poissonian values. Fig. 5.13 shows the Fano factor for two different gate voltages, $V_{gate} = 0\,\mathrm{meV}$ and $V_{gate} = 0.5\,\mathrm{meV}$. After the thermal noise limit the Fano factor is reduced due to elastic co-tunneling processes to a Poissonian value of $F = 1$. At the inelastic co-tunneling excitation energy the Fano factor first becomes super-Poissonian. It then shows a plateau whose length depends on the threshold energy of the co-tunneling assisted sequential tunneling regime at which the Fano factor increases a second time to even higher super-Poissonian values. The maximum noise (Fano factor) is reached at the bias $V_b = 2|\varepsilon_{co} - \varepsilon_{seq}|$.

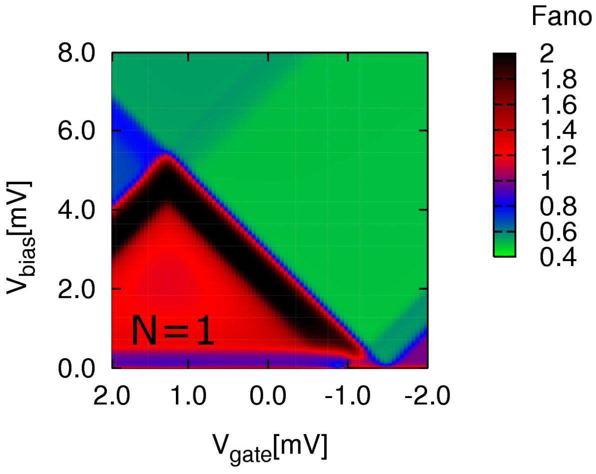

Figure 5.12: *Color-scale plot of the Fano factor vs. bias and gate voltage for the same regime as Fig. 5.10. It becomes super-Poissonian at the inelastic co-tunneling excitation energy scale and increases to even higher super-Poissonian values when co-tunneling assisted sequential tunneling processes set in (visible in form of the black inner triangle).*

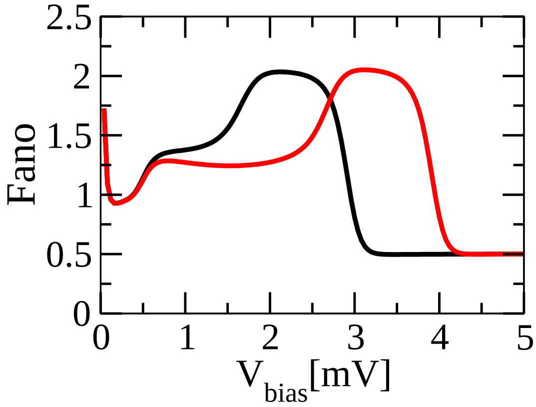

Figure 5.13: *Fano factor vs. bias voltage for two different gate voltages corresponding to vertical cuts at $V_g = 0\,\mathrm{meV}$ and $V_g = 0.5\,\mathrm{meV}$ in Fig. 5.12. The Fano factor becomes super-Poissonian at ε_{co} and increases to even higher values at the onset of co-tunneling assisted sequential tunneling.*

5.4 Summary and Outlook

We have seen in the present chapter that co-tunneling significantly influences the electronic transport through quantum dot systems. In the Coulomb blockade regime elastic as well as inelastic co-tunneling processes contribute to the current. Elastic co-tunneling takes place at arbitrary bias and is thus contributing to the current even below the inelastic co-tunneling energy. Studying the single level Anderson model we identified four regimes with characteristic features of the Fano factor. The features reflected intrinsic energy scales of the dot's low energy spectrum such as the inelastic co-tunneling excitation energy.

The inelastic co-tunneling excitation energy scale shows up as a gate voltage independent step inside the Coulomb diamond of a color scale plot of the differential conductance vs. the bias and gate voltage. Studying the differential conductance vs. the applied bias we found that the width of the inelastic co-tunneling shoulder scales with the temperature ($k_B T$) whereas the height is proportional to the coupling parameter squared (Γ^2). Still below the sequential tunneling threshold but for bias above inelastic co-tunneling excitation energy we find the regime of co-tunneling assisted sequential tunneling. This regime is only accessible if the low energy spectrum of the dot system fulfills the condition $\varepsilon_{co} < \frac{2\varepsilon_{seq}}{3}$ which is valid in the case of a symmetric bias application. At biases above the sequential tunneling threshold the steps in the current and shot noise are broadened by the temperature and the coupling parameter ($\sim k_B T + \Gamma$).

Our theoretical model described in chapter 3 allows us in principle to account for an arbitrary complex electronic structure of the studied system. We have calculated more complex systems such as the double quantum dot and the triple quantum dot from chapter 4 also within a second order description. In the Coulomb blockade they do not show qualitative new behavior compared to the two level local quantum dot discussed in this chapter. However, due to their more complex and also dense spectrum they have several low lying excitation energies that produce features similar to the inelastic co-tunneling excitation energy scale inside the Coulomb blockade. For instance the triple quantum dot shows a large and broad super-Poissonian Fano factor after the thermal divergent behavior at low bias. The Fano factor is reduced to sub-Poissonian values as soon as the sequential tunneling threshold is reached. For larger bias the current, noise and Fano factor have in principle the same shape as in the first order calculations (as displayed in chapter 4, Fig. 4.16) except for the additional broadening at the step positions which is due to the stronger coupling parameter Γ. This supports the fact, that the discussed phenomena in (sequential) first order transport are robust and thus not restricted to a weak coupling situation but would also be possible in an intermediate coupling situation in experiment.

There are several useful extension to our computational implementation. Collaborating groups from Aachen are currently including phonons vibrations into the co-tunneling implementation. This would offer the possibility to study the interplay of co-tunneling and vibrational transitions. Another extension to our model consists of the implementation of two additional leads for the system of a double quantum dot. Within this approach interesting cross-correlations can be studied. This is work in progress in our group.

Chapter 6

Conclusions

In this thesis we have presented a theoretical description of electronic transport through single and coupled quantum dot systems. Their transport properties are of fundamental interest since they display interesting quantum mechanical effects that might become important in the course of the miniaturization of electric components. Furthermore the transport properties of coupled quantum dot systems resemble strongly those of single molecules which have promising technological applications.

In nanoscale systems electronic transport is mainly governed by the interplay of electron interaction effects as well as their quantum mechanical nature. We have given an overview of characteristic transport properties which can be probed in transport measurements. Coulomb blockade behavior as well as features in the current, conductance and the shot noise have been discussed. In order to achieve a better comparison between experimental and theoretical findings our aim was to incorporate the most relevant parameters in quantum dot systems such as the electron spin, the Coulomb interaction as well as the delocalization of the electronic wavefunction into our theoretical description.

One of the main results of this thesis is the formulation of a general numerical approach that is applicable to real systems with a complex electronic structure as present in quantum dot systems and molecules. Our implementation is based on a diagrammatic real time transport theory that allows for a perturbative expansion of the current and shot noise in orders of the coupling constant Γ. We are thus able to account for a weak coupling situation of the dot system to the leads (first order in Γ) as well as an intermediate coupling regime (second order in Γ) where the coupling constant can take values up to the order of temperature. All transport properties of interest can be calculated from the transition rates between different quantum dot eigenstates. We explicitly showed how to calculate these rates up to a second order perturbative expansion for, in principle, arbitrary complex systems.

Firstly, we have studied sequential transport within a first order picture in coupled quantum dots with a strong inter-dot coupling and weak coupling to the leads. Motivated by recent experimental setups of lateral quantum dots we have investigated the transport properties of a double quantum dot system in the presence of various types of asymmetries realized by either asymmetric couplings to the leads or by detuning the quantum dot levels out of resonance with each other. We found that in a situation of a symmetric central dot system with two resonant dot levels, asymmetric coupling parameters lead to asymmetric current-voltage curves (I-V's) for positive and negative bias, respectively. This behavior has been encountered in experiments before. For strong asymmetry ratios of the left and right coupling to the leads we have observed the occurrence of negative differential conductance (NDC) which grows stronger for higher asymmetry ratios. Additionally the strong NDC is accompanied by super-Poissonian noise (with Fano factors $F > 1$) which we explain to be due to the competition of well and badly coupled, delocalized quantum dot states. The observed features always develop at the same bias positions since the spectrum of the double quantum dot remains unaffected by asymmetric contacts.

For detuned dot levels and varying inter-dot hopping we found similar transport properties resulting in features like NDC and super-Poissonian noise. In contrast to the situation of asymmetric contacts, the asymmetry is now an intrinsic property of the system and therefore features are observed at varying bias. In our discussion we could clearly distinguish between the different origins of similar characteristic transport features that might occur in an experiment all at the same time. We pointed out that the discussed effects would not be present in a simplified transport picture that neglects the non-locality of the electronic wavefunctions as well as a finite on-site Coulomb interaction.

Secondly, as a truly molecular system we have studied a chain of three coupled quantum dots. This is the simplest system in which one dot, namely the middle dot, is not directly coupled via a tunnel junction to the leads but only indirectly couples via the interfacial dots. For a totally symmetric triple quantum dot we have analyzed the current, shot noise and Fano factor for various strength of nearest neighbor Coulomb interactions. We found that the nature of the non-local electronic wavefunctions is strongly effected by the ratio of the non-local Coulomb interactions and the inter-dot hopping strength. On this basis we have predicted a strong enhancement of the shot noise over large bias regions above the sequential tunneling threshold with Fano factors that can easily reach a factor of 100. This strong enhancement is found for the case of strong Coulomb interactions that dominate over the inter-dot hopping. Calculations including second order processes have shown that the effect is robust to co-tunneling. The strong enhancement of the shot noise is of high relevance to experimentalists since it should allow an easier detection of the shot noise over the disturbing background 1/f-noise.

Thirdly, in an intermediate coupling situation of quantum dot systems to the leads co-tunneling processes become important. We have studied the effects of co-tunneling transport in the Coulomb blockade for a single level Anderson model with finite spin splitting within a second order picture. We have identified various transport regimes, according to the intrinsic energy scales of the low excitation spectrum of the quantum dot system, in which characteristic behavior of the Fano factor is observed. We found that in a pure first order description super-Poissonian Fano factors occurred as a consequence of the thermal population of excited states. In a combined first and second order picture thermal occupation did not lead to super-Poissonian Fano factors since elastic co-tunneling processes reduce the Fano factor to its uncorrelated, Poissonian value. However, at finite bias inelastic co-tunneling events cause a super-Poissonian Fano factor at the inelastic co-tunneling energy. Our findings are not restricted to the studied Anderson model but are also valid for arbitrary complex systems such as the afore-discussed coupled quantum dots. Furthermore our results are in agreement with other theoretical as well as experimental work.

Finally, we have investigated a two level quantum dot in the Coulomb blockade regime. As in typical experimental setups we have included the effect of an additional gate electrode in our discussion. We have studied the differential conductance of the system and observed typical transport features such as the Coulomb blockade diamonds as well as highly conducting lines outside the diamond corresponding to transport through excited states. Inelastic co-tunneling was seen in form of a gate voltage independent line in the conductance. We discovered that for a fixed gate voltage the width of the differential conductance peak at the inelastic co-tunneling energy scales with the temperature, while the height of the peak is proportional to the strength of the coupling constant squared. In addition we have investigated the corresponding behavior of the Fano factor in the regime that further indicates the onset of inelastic co-tunneling.

An interesting transport situation arises when an inelastic co-tunneling process can be followed by a sequential tunneling event. We have explored this regime of co-tunneling assisted sequential tunneling in detail and found an additional peak in the differential conductance still inside the Coulomb blockade. A further investigation of the gate voltage dependence of the relevant energy scale showed that these processes are gate voltage dependent similar to the sequential tunneling energy. While this transport regime has been encountered also experimentally we have additionally analyzed the Fano factor reflecting the energy scale of co-tunneling assisted sequential tunneling with a greater sensitivity than the conductance. Our recent studies propose that in the presence of relaxation processes due to photons the effect is washed out in the conductance but can still be observed in the Fano factor.

One of the most interesting challenges for the future is to use our computational model for the calculation of larger systems such as a six site benzene ring. Our approach clearly applies in this system but the computational cost at the moment is still too high. Clever schemes that reduce the number of molecular states which are relevant for transport need to be developed.

Appendix A

Appendix: Diagrammatic Rules

The transition rates $\mathbf{W}, \mathbf{W}^I, \mathbf{W}^{II}$ are obtained by applying the diagrammatic rules that have been formulated in Ref. [30] in time and energy space. They are related to the original formulation in terms of self energies Σ via $\mathbf{\Sigma}_{\chi\chi'} = i\mathbf{W}_{\chi'\chi}$. In the following we present the rules only in energy space representation since this is the representation we use also for the current and noise. Note that we also include bosonic degrees of freedom.

A.1 Energy space

Diagrams corresponding to the transition rates $\mathbf{W}$ are calculated according to the following rules:

1) For a given order k draw all topologically different diagrams with $2k$ vertices connected by k electron tunneling lines. Assign the energies E_χ to the propagators and the energy ω_l ($l = 1, ..., k$) to each tunneling line.

2) For each of the $(2k-1)$ segments enclosed by two adjacent vertices there is a resolvent $1/(\Delta E_m + i0^+)$ with $m = 1, ..., 2k-1$, where ΔE_m is the difference of the left-going minus the right-going energies.

3) Each vertex containing dot operators B (e.g. $B = c^\dagger_{i\sigma}$ in Eq. 3.47) contributes a matrix element $\langle\chi'|B|\chi\rangle$, where χ (χ') is the dot state entering (leaving) the vertex with respect to the Keldysh contour.

4) Each tunneling line of reservoir r gives rise to a factor $\gamma^\pm_{ri\sigma}(\omega_l) = \Gamma^{i\sigma}_r/2\pi\ f^\pm(\omega_l - \mu_r)$, where the plus-sign has to be taken if the line is going backward with respect to the closed time path, and the minus-sign if it is going forward. Here $f(x) = f^+(x) = 1 - f^-(x) = 1/(\exp(x/k_\mathrm{B}T) + 1)$ corresponds to the Fermi function. Similarly the

contribution of a boson line is given by $b(x) = sign(x)\alpha_{\text{ph}}(x)n_{\text{b}}(x)$, with the Bose function $n_{\text{b}}(x) = 1/(\exp{(x/k_{\text{B}}T)} - 1)$.

5) There is an overall pre-factor $(-i)(-1)^c$, where c is the total number of vertices on the backward propagator plus the number of crossings of tunneling lines (no bosonic lines).

6) Integrate over the energies ω_i of the tunneling and sum over all reservoir, spin and orbital degrees of freedom.

For diagrams containing external vertices such as the current vertex we have to formulate additional rules. The only difference is that for the current and shot noise rates $\mathbf{W}^I$ ($\mathbf{W}^{II}$) one (two) internal vertices are replaced by external ones representing $\hat{I}\hbar/e$. Hence we have to multiply an overall pre-factor, which arises due to the symmetric definition of the current operator and the changed number of internal vertices on the backward propagator. The additional rules therfore read:

7) Assign a factor +1/2 for each external vertex on the upper (lower) branch of the Keldysh contour which describes tunneling of an electron into the right (left) or out of the left (right) lead, and −1/2 in the other four cases.

8) Sum up all the factors for each possibility to replace one (two) internal vertices by external ones.

An example for a diagram describing the coupling to the electronic reservoirs is shown in Fig. A.1. A bosonic contribution is shown in Fig.A.2. In second order we encounter diagrams containing two tunneling lines as depicted in chapter 3.5.3..

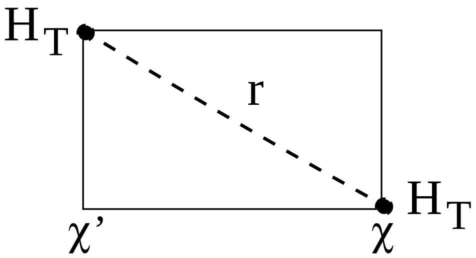

Figure A.1: *An example of a first order diagram with two internal vertices H_T and one electron tunneling line.*

The coupling to a bosonic bath is illustrated by a diagram containing a wiggly line (Fig A.2).

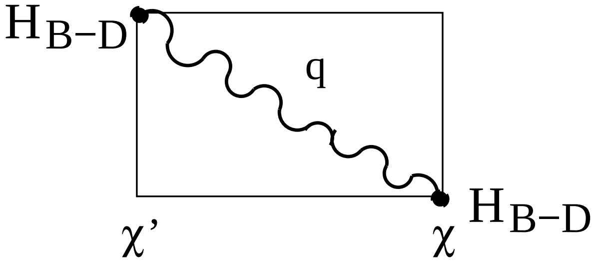

Figure A.2: *An example of a first order diagram describing the coupling to a bosonic bath.*

Appendix B

Appendix: Sequential tunneling rates

The first order transition rates $\mathbf{W}^{(1)}$, $\mathbf{W}^{(1)I}$ and $\mathbf{W}^{(1)II}$ have been calculated in [33] using the diagrammatic rules (as stated in appendix A). Following this approach we summarize their findings below.

B.1 Transition rates W

The total transition rates $W^{(1)}_{\chi,\chi'}$ (in the absence of relaxation) are the sum of transition rates associated with electron tunneling through either the left or the right barrier, $W^{(1)}_{\chi,\chi'} = W^{(1)\mathrm{R}}_{\chi,\chi'} + W^{(1)\mathrm{L}}_{\chi,\chi'}$. For the inclusion of bosonic degrees of freedom, e.g. to describe relaxation processes, we have to consider additional rates $W^{(1)\mathrm{ph}}_{\chi,\chi'}$. Assuming weak coupling to the bosonic bath (in addition to weak tunneling), we only keep contributions to either first order in α_{ph} or to first order in Γ. The total transition rates are, thus, given by $W^{(1)}_{\chi,\chi'} = W^{(1)\mathrm{L}}_{\chi,\chi'} + W^{(1)\mathrm{R}}_{\chi,\chi'} + W^{(1)\mathrm{ph}}_{\chi,\chi'}$, where $W^{(1)\mathrm{ph}}_{\chi,\chi'}$ describe pure relaxation while $W^{(1)\mathrm{L}}_{\chi,\chi'}$ and $W^{(1)\mathrm{R}}_{\chi,\chi'}$ models pure tunneling. The additivity of pure tunneling or boson rates is given only in lowest order, where only single lines are present in diagrams. Together with $\Gamma^{i\sigma}_r = 2\pi|t^r_{i\sigma}|^2\rho_e$ we find

$$W^{(1)r}_{\chi',\chi} = 2\pi\rho_e \sum_\sigma \left[f^+_r(E_{\chi',\chi}) \left| \sum_i t^r_{i\sigma} \langle\chi'|c^\dagger_{i\sigma}|\chi\rangle \right|^2 + f^-_r(-E_{\chi',\chi}) \left| \sum_i t^r_{i\sigma} \langle\chi'|c_{i\sigma}|\chi\rangle \right|^2 \right] \tag{B.1}$$

for $\chi' \neq \chi$, together with $W^{(1)r}_{\chi,\chi} = -\sum_{\chi'\neq\chi} W^{(1)r}_{\chi',\chi}$ (sum rule). $E_{\chi',\chi} = E_{\chi'} - E_\chi$ is the energy difference between the many-body states χ and χ'. Here, $f(x) =$

$1/(\exp(x/k_{\mathrm{B}}T)+1)$ is the Fermi function, $f^{+}(x)=f(x)$ and $f^{-}(x)=1-f(x)$, and $f_r^{\pm}(x)=f^{\pm}(x-\mu_r)$. The bosonic rates are

$$W^{(1)\mathrm{ph}}_{\chi',\chi}=\sum_{\sigma} b(E_{\chi',\chi})\left|\sum_{i\neq j}\langle\chi'|c^{\dagger}_{i\sigma}c_{\bar{j}\sigma}|\chi\rangle\right|^{2} \tag{B.2}$$

for $\chi'\neq\chi$, and $W^{(1)\mathrm{ph}}_{\chi,\chi}=-\sum_{\chi'\neq\chi}W^{(1)\mathrm{ph}}_{\chi',\chi}$, where $b(x)=sign(x)\;\alpha_{\mathrm{ph}}(x)\;n_{\mathrm{b}}(x)$, with the Bose function $n_{\mathrm{b}}(x)=1/(\exp(x/k_{\mathrm{B}}T)-1)$. This allows to build the matrix blocks $\mathbf{W}^{(1)}$ to calculate the objects $\mathbf{p}^{(0)\mathrm{st}}$ and $\mathbf{P}^{(-1)}$. The presence of relaxation therefore leads to a modification of the probabilities and propagators $\mathbf{P}^{(-1)}$, whereas the matrices $\mathbf{W}^{(1)I}$ and $\mathbf{W}^{(1)II}$ are not affected (due to only one tunneling line). The results obtained here could be calculated within a golden rule approximation as well.

B.2 Current rates $\mathbf{W}^{I}$

The matrix elements of $\mathbf{W}^{(1)I}$ are given by

$$W^{(1)I}_{\chi',\chi}=(W^{(1)\mathrm{R}}_{\chi',\chi}-W^{(1)\mathrm{L}}_{\chi',\chi})(\Theta(N_{\chi'}-N_{\chi})-\Theta(N_{\chi}-N_{\chi'})) \tag{B.3}$$

with the Heaviside Θ-function, where N_χ is the total number of electrons on the dot within the state χ. This permits the computation of the first order current $I^{(1)}$. An example of a corresponding diagram including one tunneling line is shown in Fig. B.1.

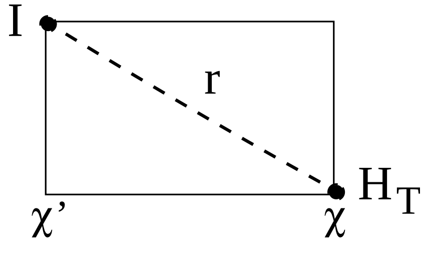

Figure B.1: *An example of a first order diagram contributing to the current.*

B.3 Shot noise rates $\mathbf{W}^{II}$

Correspondingly we find for the matrix elements of $\mathbf{W}^{(1)II}$

$$W^{(1)II}_{\chi',\chi}=\frac{1}{4}(W^{(1)\mathrm{R}}_{\chi',\chi}+W^{(1)\mathrm{L}}_{\chi',\chi})(1-2\;\delta_{\chi'\chi}) \tag{B.4}$$

with the Kronecker δ. This is the last missing object to compute the shot noise in first order $S^{(1)}$. In first order there is only one possibility to place the two current vertices, as shown in Fig. B.2.

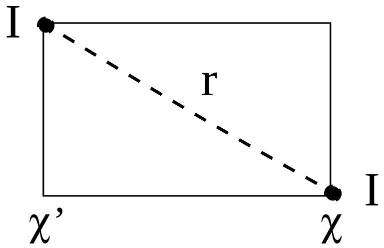

Figure B.2: *An example of a first order diagram contributing to the shot noise.*

Appendix C

Appendix: Co-tunneling rates

In order to determine the co-tunneling contributions to current and noise we have to calculate in addition to the first order terms the second order matrices $\partial\mathbf{W}^{(1)}$, $\partial\mathbf{W}^{(1)I}$, $\mathbf{W}^{(2)}$, $\mathbf{W}^{(2)I}$ and $\mathbf{W}^{(2)II}$. Once they are known one can easily compute $\mathbf{p}^{(1)\mathrm{st}}, \mathbf{P}^{(0)}, I^{(2)}, S^{(2)}$ and thus $I = I^{(1)} + I^{(2)}$ and $S = S^{(1)} + S^{(2)}$. To obtain the second order transition rates $W^{(2)}$ we have to solve two double integrals as mentioned earlier in chapter 3.5.3 (see also Eq. 3.49). By using prefactors as stated in the diagrammatic rules for diagrams with external current vertices we can then determine $\mathbf{W}^{(2)I}$ and $\mathbf{W}^{(2)II}$. The objects $\partial\mathbf{W}^{(1)}$, $\partial\mathbf{W}^{(1)I}$ are calculated in appendix C.2.

C.1 Calculation of the double integral $\tilde{D}^{A,B}_{I,II}$

In the following we sketch the mathematical solution of the double integrals $\tilde{D}^{A,B}_{I,II}$. For the diagrams of type I (see Fig.3.4) we have to solve

$$\tilde{D}_I = \int_{-\infty}^{\infty}\int_{-\infty}^{\infty} d\omega_1 d\omega_2 2i\mathrm{Im}\frac{\gamma^{p_1}_{r_1,l_1,\sigma_1}(\tau_1\omega_1)\gamma^{p_2}_{r_2,l_2,\sigma_2}(\tau_2\omega_2)}{(\omega_1+\Delta_1+i\eta)(\omega_1+\omega_2+\Delta_{12}+i\eta)(\omega_2+\Delta_2+i\eta)} \tag{C.1}$$

and for diagrams of type II

$$\tilde{D}_{II} = \int_{-\infty}^{\infty}\int_{-\infty}^{\infty} d\omega_1 d\omega_2 2i\mathrm{Im}\frac{\gamma^{p_1}_{r_1,l_1,\sigma_1}(\tau_1\omega_1)\gamma^{p_2}_{r_2,l_2,\sigma_2}(\tau_2\omega_2)}{(\omega_2+\Delta_2'+i\eta)(\omega_1+\omega_2+\Delta_{12}+i\eta)(\omega_2+\Delta_2+i\eta)} \tag{C.2}$$

Here the function $\gamma^{\pm}_{r_i l_i \sigma_i}(\omega)$ is related to the Fermi function $f(x)$ as defined in appendix A where the indices correspond to $r_i = \mathrm{R}, \mathrm{L}$, $l_i = 1, .., N$ (with N being the total number of orbitals) and $\sigma_i = \uparrow, \downarrow$ respectively. The energies $\Delta_1, \Delta_{12}, \Delta_2, \Delta_2'$ are composed of the energies E_χ in general and η denotes a convergence factor which is taken in the limit

$\eta = 0^+$. The factors $\tau_1, \tau_2, p_1, p_2 = \pm 1$ account for signs that arise when following the diagrammatic rules (appendix A). When solving Eqs. C.1 and C.2 one integration can always be performed making use of the delta function. The delta function appears when the resolvent is manipulated using a partial fraction decomposition amongst others and the relations

$$\mathrm{Im}\frac{1}{x + i\eta} = -\pi\delta(x)$$

$$\mathrm{Im}\frac{1}{(x + i\eta)^2} = \pi\delta'(x),$$

where $x, y \in \mathbb{R}$ correspond to energies in our case. Having performed the first integration leads to expressions of the form

$$F^{\pm}_{ri\sigma}(\varepsilon) = \int\limits_{-\infty}^{\infty} d\omega \frac{\gamma^{\pm}_{ri\sigma}(\omega)}{(\varepsilon - \omega + i\eta)}. \tag{C.3}$$

The solution of Eq. C.3 can be found in Ref. [33] and is related to the digamma function $\Psi(z)$. We can now write explicitly for the type I diagrams

$$\tilde{D}_I = \begin{cases} \tilde{D}_I^A & \text{if } \Delta_1 + \Delta_2 = \Delta_{12} \\ \tilde{D}_I^B & \text{if } \Delta_1 + \Delta_2 \neq \Delta_{12} \end{cases} \tag{C.4}$$

with

$$\tilde{D}_I^A = \frac{i}{2\pi}\Gamma^{l_1,\sigma_1}_{r_1}\Gamma^{l_2,\sigma_2}_{r_2}\partial_\rho \left[F(\Delta_1, \rho) + C_1(\Delta_1, \rho) + C_2(\Delta_2, \rho)\right]|_{\rho=0} \tag{C.5}$$

$$\begin{aligned} \tilde{D}_I^B = \frac{i}{2\pi}\Gamma^{l_1,\sigma_1}_{r_1}\Gamma^{l_2,\sigma_2}_{r_2}\frac{1}{\Delta_1 + \Delta_2 - \Delta_12}\{F(\Delta_{12} - \Delta_2, \rho) - F(\Delta_1, \rho) \\ +C_1(\Delta_{12} - \Delta_2, \rho) - C_1(\Delta_1, \rho) + C_2(\Delta_{12} - \Delta_1, \rho) - C_2(\Delta_2, \rho)\}|_{\rho=0}, \end{aligned} \tag{C.6}$$

where ρ is an energy variable that is set to zero in the end. In the above equations C.5 and C.6 the following helper functions have been used:

$$\begin{aligned} F(\alpha, \rho) &= (-\delta_{\tau_1,p_2,\tau_2,p_2}\tau_1 p_1 + \tau_2 p_2)H(-\tau_1\mu_{r_1}, \alpha - \rho) \\ &+ \begin{cases} \frac{\tau_1\tau_2 p_1 p_2}{\beta}\frac{\partial}{\partial\rho}H(-\tau_1\mu_{r_1}, \alpha - \rho) & \text{if } \sum_i(\tau_i\mu_{r_i}) + \Delta_{12} = 0 \\ \tau_2 p_2 b(-p_1\mu_{r_1} - \tau_1 p_1\Delta_{12} - \tau_1\tau_2 p_1\mu_{r2})\cdot & \\ \left[H(-\tau_1\mu_{r_1}, \alpha - \rho) - H(\tau_2\mu_{r_2} + \Delta_{12}, \alpha - \rho)\right] & \text{else} \end{cases} \end{aligned} \tag{C.7}$$

$$C_1(\alpha, \rho) = \tau_1 p_1 f(-\tau_2 p_2\Delta_2 - p_2\mu_{r_2}) \cdot H(-\tau_1\mu_{r_1}, \alpha - \rho) \tag{C.8}$$

$$C_2(\alpha, \rho) = \tau_2 p_2 f(-\tau_1 p_1\Delta_1 - p_1\mu_{r_1}) \cdot H(-\tau_2\mu_{r_2}, \alpha - \rho) \tag{C.9}$$

where $b(x), f(x)$ denote the Bose- and Fermi-functions respectively and H is related to the digamma function ψ via

$$H(x,y) = \left[\ln\left(\frac{\beta E_C}{2\pi}\right) - \mathrm{Re}\psi\left(\frac{1}{2} + \frac{i\beta}{2\pi}(x-y)\right)\right]. \tag{C.10}$$

In the above set of equations the arguments are all real numbers $\alpha, \rho, x, y \in \mathbb{R}$, $\beta = 1/(k_B T)$ denotes the inverse temperature and E_C corresponds to a "cutoff" energy that should be chosen much larger than all other energy scales. However, one can see imediately from the mathematical structure of Eqs. (C.5 and C.7) that the diagrammatic contributions are actually independent of that cutoff parameter, since only differences or derivatives of the digamma function appear. For the type II diagrams (see Fig. 3.5) we obtain similarly

$$\tilde{D}_{II} = \begin{cases} \tilde{D}_I^A & \text{if } \Delta_2 = \Delta_2' \\ \tilde{D}_{II}^B & \text{if } \Delta_2 \neq \Delta_2' \end{cases} \tag{C.11}$$

with

$$\tilde{D}_{II}^A = \frac{i}{2\pi}\Gamma_{r_1}^{l_1,\sigma_1}\Gamma_{r_2}^{l_2,\sigma_2}\partial_\rho\left[-F(\Delta_{12}-\Delta_2,\rho) - G_1(\Delta_{12}-\Delta_2,\rho)\right]|_{\rho=0} \tag{C.12}$$

$$\begin{aligned}\tilde{D}_{II}^B = \frac{i}{2\pi}\Gamma_{r_1}^{l_1,\sigma_1}\Gamma_{r_2}^{l_2,\sigma_2}\frac{1}{(\Delta_2'-\Delta_2)}&\{F(\Delta_{12}-\Delta_2,\rho) - F(\Delta_{12}-\Delta_2',\rho) \\ &+C_1(\Delta_{12}-\Delta_2,\rho) - C_1'(\Delta_{12}-\Delta_2',\rho)\}|_{\rho=0},\end{aligned} \tag{C.13}$$

where we have defined two new helper functions G_1 and C_1'

$$G_1(\alpha,\rho) = \tau_1 p_1 f(-\tau_2 p_2 \Delta_2 - p_2\mu_{r_2} - p_2\tau_2\rho)\cdot H(-\tau_1\mu_{r_1}, \alpha-\rho) \tag{C.14}$$

$$C_1'(\alpha,\rho) = \tau_1 p_1 f(-\tau_2 p_2 \Delta_2' - p_2\mu_{r_2})\cdot H(-\tau_1\mu_{r_1}, \alpha-\rho). \tag{C.15}$$

Note that the latter does not correspond to a derivative but is very similar to the helper function C_1 but with an energy argument Δ_2' instead of Δ_2 in the fermi function.

C.2 Calculation of $\partial W^{(1)}$ and $\partial W^{I(1)}$

The derivatives of first order rates $\partial\mathbf{W}, \partial\mathbf{W}^I$ have a very similar structure as the second order transition rates. They correspond to non-Markovian memory effects [33] and only appear when transport up to second order in Γ is taken into account. We specifiy in the following how these rates can be obtained. The derivative of the first order transition rate in reservoir r is given by the expression

$$\partial W^{r(1)}_{\chi'\chi} = \sum_{l,\sigma} \frac{\Gamma^r_{l,\sigma}}{\pi} \Big\{ -\partial_\rho H(\varepsilon+\rho,\mu_r)|_{\varepsilon=\varepsilon_{\chi'}-\varepsilon_\chi} \, |\langle\chi'|c^\dagger_{l,\sigma,r_1}|\chi\rangle|^2 + \tag{C.16}$$

$$\partial_\rho H(\varepsilon+\rho,\mu_r)|_{\varepsilon=\varepsilon_\chi-\varepsilon_{\chi'}} |\langle\chi'|c_{l,\sigma,r}|\chi'\rangle|^2 \Big\} \tag{C.17}$$

where

$$-\partial_\varepsilon H(\varepsilon,\mu_r) = -\partial_\rho H(\varepsilon+\rho,\mu_r)|_{\rho=0} = \psi'_r(\varepsilon) \tag{C.18}$$

and the function H is defined as above (Eq. C.10). The total derivative rates are thus obtained by summing over the reservoir degrees of freedom

$$\partial W^{(1)}_{\chi'\chi} = \sum_r \partial W^{r(1)}_{\chi'\chi} \qquad \text{for states } \chi' \neq \chi \tag{C.19}$$

with the diagonal rates

$$\partial W^{r(1)}_{\chi\chi} = -\sum_{\chi'\chi} \partial W^{r(1)}_{\chi'\chi}. \tag{C.20}$$

Similarly to the first order current rates $W^{I(1)}_{\chi'\chi}$ the derivative of the current rates is defined by the expression

$$\partial W^{(1)I}_{\chi'\chi} = \left(\partial W^{R(1)}_{\chi'\chi} - \partial W^{L(1)}_{\chi'\chi}\right)\left(\Theta(N_{\chi'}-N_\chi) - \Theta(N_\chi - N_{\chi'})\right) \tag{C.21}$$

C.3 Calculation of the second order current rates $W^{I(2)}$ and shot noise rates $W^{II(2)}$

In first order the current and shot noise rates $W^{I(1)}, W^{II(1)}$ could be constructed out of the total first order transition rates and additional global signs and prefactors (see appendix B) that arise due to the definition of the diagrammatic rules in energy space. For the second order current and shot noise transition rates no global prefactors can be formulated. Instead each second order diagram D_X as defined in Fig. 3.4 is multiplied by a prefactor F^I and F^{II} respectively. The total second order current and shot noise rates are then obtained using Eq. 3.47 formulated for the transition rates $W^{(2)}$ with diagrams $D_X^{I,II} = D_X F^{I,II}$. The prefactors consist of two contributions. First the creation (annihilation) of an electron at a vertex gives rise to a sign $j_i = +(-)$. This rule corresponds a tunneling line that is either going in or out of a vertex. Second an external vertex causes a factor $+1/2$ $(-1/2)$ if the reservoirs $r_i = R(L)$ is involved in the current flow from the left to the right. We define

$$r_i = \begin{cases} 1 & \text{if } r_i = R \\ 2 & \text{if } r_i = L \end{cases} \tag{C.22}$$

and $R_i = \frac{1}{2}(-1)^{r_i}$. The following tables summarize all prefactors:

Prefactor	D_{3aI}	D_{3aII}	D_{3bI}	D_{3bII}	D_{3cI}	D_{3cII}	D_{3dI}	D_{3dII}
F^I	$-2j_2R_2$	$-2j_2R_2$	$-2j_1R_1$	$-2j_1R_1$	$2j_2R_2$	$2j_1R_1$	$2j_1R_1$	$2j_2R_2$
F^{II}	0	0	0	0	0	0	0	0

Table C.1: *Prefactors F^I and F^{II} for the diagrams of Fig. 3.4 according to the diagrammatic rules defined in appendix A. j_i denotes a sign due to a tunneling line going in or out of a vertex and R_i corresponds to an external (current) vertex connected to the right or left reservoir.*

Prefactor	D_{4I}	D_{4II}	D_{2aI}	D_{2aII}
F^I	0	0	$-2(j_1R_1 + j_2R_2)$	$-2(j_1R_1 + j_2R_2)$
F^{II}	-0.5	-0.5	$4j_1j_2R_1R_2 + 0.5$	$4j_1j_2R_1R_2 + 0.5$

Prefactor	D_{2bI}	D_{2bII}	D_{2cI}	D_{2cII}
F^I	0	$2j_1R_1 - 2j_2R_2$	$2j_1R_1 - 2j_2R_2$	0
F^{II}	-0.5	$-4j_1j_2R_1R_2 + 0.5$	$-4j_1j_2R_1R_2 + 0.5$	-0.5

Table C.2: *Prefactors F^I and F^{II} for the diagrams of Fig. 3.5 according to the diagrammatic rules defined in appendix A. j_i denotes a sign due to a tunneling line going in or out of a vertex and R_i corresponds to an external (current) vertex connected to the right or left reservoir.*

Bibliography

[1] P. J. van Wees, H. van Houton, C. W. J. Beenakker, J. G. Williamson, L. P. Kouwenhoven, D. van der Marel, and C. T. Foxon, Phys. Rev. Lett. **60**, 848 (1988).

[2] S. Bandyopadhyay and H. S. Nalwa, *Quantum Dots and Nanowires*, American Scientific Publishers (ASP), (2003).

[3] H. Park, J. Park, A. K. L. Lim, E. H. Anderson, A. P. Alivisatos, and P. L. McEuen, Nature **407**, 57 (2000).

[4] M. Elbing, R. Ochs, M. Koentopp, C. Fischer, von Hänisch, F. Weigend, F. Evers, H. B. Weber, and M. Mayor, Proc. Nat. Acad. Sci. **102**, 8815–8820 (2005).

[5] E. Onac, F. Balestro, B. Trauzettel, C. Lodewijk, and L. P. Kouwenhoven, Phys. Rev. Lett. **96**, 026803 (2006).

[6] R. Schleser, T. Ihn, E. Ruh, K. Ensslin, M. Tews, D. Pfannkuche, D. C. Driscoll, and A. C. Gossard, Phys. Rev. Lett. **94**, 206805 (2005).

[7] J. Reichert, *Leitfähigkeitsmessungen an einzelnen organischen Molekülen*, Wissenschaftliche Berichte, FZKA-6851, Ph.D Thesis, Universität Karlsruhe, Germany (2003).

[8] P. Jarillo-Herrero, S. Sapmaz, C. Dekker, L. P. Kouwenhoven, and H. S. J. van der Zant, Nature **429**, 389 (2004).

[9] J. Nygard, D. H. Cobden, and P. E. Lindelof, Nature **408**, 342 (2000).

[10] M. Büttiker, in *Quantum Noise in Mesoscopic Physics*, ed. Yu. V. Nazarov, NATO Science Series II: Mathematics, Physics and Chemistry **97**, 3 (2003).

[11] G. Schön, in *Quantum Transport and Dissipation, chapter 3*, eds. T. Dittrich, P. Hänggi, G.- L. Ingold, B. Kramer, G. Schön, and W. Zwerger, Wiley-VCH Verlag (1998).

[12] J. Park, A. N. Pasupathy, J. I. Goldsmith, C. Chang, Y. Yaish, J. R. Petta, M. Rinkoski, J. P. Sethna, H. D. Abruna, P. L. McEuen, and D. C. Ralph, Nature **417**, 722 (2002).

[13] D. Goldhaber-Gordon, H. Shtrikman, D. Mahalu, D. Abusch-Magder, U. Meirav, and M. A. Kastner, Nature (London) **391**, 156 (1998).

[14] D. Goldhaber-Gordon, J. Göres, M. A. Kastner, H. Shtrikman, D. Mahalu, and U. Meirav, Phys. Rev. Lett. **81**, 5225 (1998).

[15] S. Tarucha, D. Austing, T. Honda, R. J. van der Hage, and L. P. Kouwenhoven, Phys. Rev. Lett. **77**, 3613 (1996).

[16] J. Reichert, H. B. Weber, M. Mayor, and H. v. Löhneysen, Appl. Phys. Lett. **82**, 4137 (2003).

[17] G. Schön, in *Mesoscopic Electron Transport*, eds. L. L. Sohn, L. P. Kouwenhoven, and G. Schön, NATO ASI Series E, Kluwer, Dordrecht **345**, 1 (1997).

[18] S. Datta, *Electronic Transport in Mesoscopic Systems*, Cambridge University Press, (1995).

[19] W. G. van der Wiel, S. De Franceschi, J. M. Elzerman, T. Fujisawa, S. Tarucha, and L. P. Kouwenhoven, Phys. Rev. Lett. **86**, 878 (2001).

[20] M. R. Wegewijs, M. H. Hettler, K. Nowack, C. Romeike, A. Thielmann, and J. König, in *Introducing Molecular Electronics*, Lecture Notes in Physics **680**, 145–164 (2005).

[21] G. Kiesslich, A. Wacker, and E. Schoell, Phys. Rev. B **68**, 125320 (2003).

[22] A. Thielmann, M. H. Hettler, J. König, and G. Schön, Phys. Rev. Lett. **95**, 146806 (2005).

[23] J. Aghassi, A. Thielmann, M. H. Hettler, and G. Schön, Appl. Phys. Lett. **89**, 052101 (2006).

[24] A. Nauen, *Rauschmessungen an mikroskopischen Tunnelsystemen*, Ph.D Thesis, Hannover, Germany (2003).

[25] A. Nauen, F. Hohls, N. Maire, K. Pierz, and R. J. Haug, Phys. Rev. B **70**, 033305(R) (2004).

[26] A. Thielmann, M. H. Hettler, J. König, and G. Schön, Phys. Rev. B **68**, 115105 (2003).

[27] A. Thielmann, M. H. Hettler, J. König, and G. Schön, Phys. Rev. B **71**, 045341 (2005).

[28] B. Elattari and S. A. Gurvitz, Phys. Rev. Lett. **292**, 289 (2002).

[29] S. De Franceschi, S. Sasaki, J. M. Elzerman, W. G. van der Wiel, S. Tarucha, and L. P. Kouwenhoven, Phys. Rev. Lett. **86**, 878 (2001).

[30] J. König, H. Schoeller, and G. Schön, Phys. Rev. Lett. **76**, 1715 (1996).

[31] J. König, J. Schmid, H. Schoeller, and G. Schön, Phys. Rev. B **54**, 16820 (1996).

[32] H. Schoeller, in *Mesoscopic Electron Transport*, eds. L. L. Sohn, L. P. Kouwenhoven, and G. Schön, NATO ASI Series E, Kluwer, Dordrecht **345**, 291 (1997).

[33] A. Thielmann, *Co-tunneling current and shot noise in molecules and quantum dots*, Wissenschaftliche Berichte, FZKA 7167, Forschungszentrum Karlsruhe (2005).

[34] J. Aghassi, A. Thielmann, M. H. Hettler, and G. Schön, Phys. Rev. B **73**, 195323 (2006).

[35] T. Hatano, M. Stopa, T. Yamaguchi, T. Ota, K. Yamada, and S. Tarucha, Phys. Rev. Lett. **93**, 066806 (2004).

[36] D. Boese, *Quantum Transport through Nanostructures: Quantum Dots, Molecules, and Quantum Wires*, Shaker, Aachen (2002).

[37] J. König, *Quantum Fluctuations in the Single-Electron Transistor*, Shaker Verlag, Aachen (1999).

[38] H.-A. Engel and D. Loss, Science **309**, 586 (2005).

[39] J. R. Petta, A. Johnson, J. Taylor, E. A. Laird, A. Yacoby, M. Lukin, C. M. Marcus, M. P. Hanson, and A. C. Gossard, Science **309**, 2180 (2005).

[40] M. Büttiker, Y. Imry, R. Landauer, and S. Pinhas, Phys. Rev. B **31**, 6207 (1985).

[41] M. Büttiker, Phys. Rev. Lett. **57**, 1761 (1986).

[42] Y. M. Blanter and M. Büttiker, Phys. Rep. **336**, 1 (2000).

[43] Y. Imry, *Introduction to mesoscopic physics, chapter 8*, Oxford University Press (2002).

[44] S. Kogan, *Electronic Noise and Fluctuations in Solids*, Cambridge University Press (1996).

[45] M. Henny, S. Oberholzer, C. Strunk, and C. Schönenberger, Phys. Rev. B **59**, 2871 (1999).

[46] S. S. Safonov, A. K. Savchenko, D. A. Bagrets, O. N. Jouravlev, Y. V. Nazarov, E. H. Linfield, and D. A. Ritchie, Phys. Rev. Lett. **91**, 136801 (2003).

[47] M. Reznikov, M. Heiblum, H. Shtrikman, and D. Mahalu, Phys. Rev. Lett. **75**, 3340 (1995).

[48] A. Kumar, L. Saminadayar, D. C. Glattli, Y. Jin, and B. Etienne, Phys. Rev. Lett. **76**, 2778 (1996).

[49] S. W. Jung, T. Fujisawa, Y. Hirayama, and Y. H. Jeong, Appl. Phys. Lett. **85**, 768 (2004).

[50] J. H. Davies, P. Hyldgaard, S. Hershfield, and J. W. Wilkins, Phys. Rev. B **46**, 9620 (1992).

[51] A. Nauen, F. Hohls, J. Könemann, and R. J. Haug, Phys. Rev. B **69**, 113316 (2004).

[52] A. Nauen, I. Hapke-Wurst, F. Hohls, U. Zeitler, R. J. Haug, and K. Pierz, Phys. Rev. B **66**, 161303 (2002).

[53] W. Schottky, Ann. Phys. (Leipzig) **57**, 541 (1918).

[54] M. Büttiker, Phys. Rev. B **46**, 12485 (1992).

[55] Y. Meir and N. S. Wingreen, Phys. Rev. Lett. **68**, 2512 (1992).

[56] V. A. Khlus, Zh. Eksp. Teor. Fiz. **93**, 2179 [Sov. Phys. JETP **66**, 1243] (1987).

[57] H. Birk, M. J. M. de Jong, and C. Schönenberger, Phys. Rev. Lett. **75**, 1610 (1995).

[58] E. V. Sukhorukov, G. Burkard, and D. Loss, Phys. Rev. B **63**, 125315 (2001).

[59] G. Kiesslich, A. Wacker, E. Schoell, A. Nauen, F. Hohls, and R. J. Haug, Phys. Stat. Sol. C **0**, 1293 (2003).

[60] G. Michalek and B. R. Bulka, Eur. Phys. J. B **28**, 121 (2002).

[61] W. Belzig, Phys. Rev. B **71**, 161301 (2005).

[62] M. H. Hettler, H. Schoeller, and W. Wenzel, in *Nano-Physics and Bio-Electronics: A New Odyssey, chapter 11*, eds. T. Chakraborty, F. Peeters, and U. Sivan, Elsevier (2002).

[63] M. H. Hettler, H. Schoeller, and W. Wenzel, Europhys. Lett. **57**, 571 (2002).

[64] M. H. Hettler, W. Wenzel, M. R. Wegewijs, and H. Schoeller, Phys. Rev. Lett. **90**, 076805 (2003).

[65] *Molecular Electronics II*, eds. A. Aviram, M. Ratner, and V. Mujica, Ann. N.Y. Acad. Sci. **960** (2002).

[66] *Molecular Electronics: Science and Technology*, eds. A. Aviram and M. Ratner, Ann. N.Y. Acad. Sci. **852** (1998).

[67] D. Djukic and J. M. van Ruitenbeek, Nano Lett. **6**, 789–793 (2006).

[68] J. Weis, R. J. Haug, K. v. Klitzing, and K. Ploog, Phys. Rev. Lett. **71**, 4019 (1993).

[69] D. M. Zumbühl, C. M. Marcus, M. P. Hanson, and A. C. Gossard, Phys. Rev. Lett. **93**, 256801 (2004).

[70] V. N. Golovach and D. Loss, Phys. Rev. B **69**(245327) (2004).

[71] M. Mayor and H. Weber, Chimia **56**, 494 (2002).

[72] J. Reichert, R. Ochs, D. Beckmann, H. B. Weber, M. Mayor, and H. v. Löhneysen, Phys. Rev. Lett. **88**, 176804 (2002).

[73] M. A. Reed, C. Zhou, C. J. Muller, T. P. Burgin, and J. M. Tour, Science **278**, 252 (1997).

[74] M. Mayor, C. v. Hänisch, H. B. Weber, J. Reichert, and D. Beckmann, Angew. Chem. **114**, 1228 (2002).

[75] C. Kergueris, J. P. Bourgoin, S. Palacin, D. Esteve, C. Urbina, M. Magoga, and C. Joachim, Phys. Rev. B **59**, 12505 (1999).

[76] J. Chen, M. A. Reed, A. M. Rawlett, and J. M. Tour, Science **286**, 1550 (1999).

[77] H. Heersche, Z. de Groot, J. A. Folk, H. S. J. van der Zant, C. Romeike, M. R. Wegewijs, L. Zobbi, D. Barreca, E. Tondello, and A. Cornia, Phys. Rev. Lett. **96**, 206801 (2006).

[78] G. Mahan, *Many Particle Physics*, Plenum Publishing Corporation, (2000).

[79] U. Meirav and E. B. Foxman, Semicond. Sci. Technol. **11**, 255 (1996).

[80] M. Di Ventra, S. Pantelides, and N. Lang, Phys. Rev. Lett. **84**, 979 (2000).

[81] J. Heurich, J. Cuevas, W. Wenzel, and G. Schön, Phys. Rev. Lett. **88**, 256803 (2002).

[82] F. Evers, F. Weigend, and M. Koentopp, Physica E **18**, 255 (2003).

[83] R. Landauer, IBM J. Res. Dev. **1**, 233 (1957).

[84] J. Rammer and H. Smith, Rev. Mod. Phys. **58**, 323 (1986).

[85] A. N. Korotkov, Phys. Rev. B **49**, 10381 (1993).

[86] S. Hershfield, J. H. Davies, P. Hyldgaard, C. J. Stanton, and J. W. Wilkins, Phys. Rev. B **47**, 1967 (1993).

[87] S. Hershfield, J. H. Davies, and J. W. Wilkins, Phys. Rev. Lett. **67**, 3720 (1991).

[88] B. Wunsch, M. Braun, J. König, and D. Pfannekuche, Phys. Rev. B **72**, 205319 (2005).

[89] J. N. Pedersen, B. Lassen, A. Wacker, and M. H. Hettler, cond-mat/0703116, (2007).

[90] B. R. Bulka and T. Kostyrko, Phys. Rev. B **70**, 205333 (2004).

[91] I. Weymann, J. König, J. Martinek, J. Barnas, and G. Schön, Phys. Rev. B **72**, 115334 (2005).

[92] A. Thielmann, M. H. Hettler, J. König, and G. Schön, in preparation (2007).

[93] A. Tewes, *Electronic structure and transport properties of quantum dots*, PHD Thesis, University Hamburg (2003).

[94] A. Cottet and W. Belzig, Europhys. Lett. **66**, 405 (2004).

[95] A. N. Jordan and E. V. Sukhorokov, Phys. Rev. Lett. **93**, 260604 (2004).

[96] J. Koch and F. von Oppen, Phys. Rev. Lett. **94**, 206804 (2005).

[97] A. K. Huttel, S. Ludwig, K. Eberl, and J. P. Kotthaus, Phys. Rev. B **72**, 081310(R) (2005).

[98] L. DiCarlo, H. J. Lynch, A. C. Johnson, K. Childress, K. Crockett, C. M. Marcus, M. P. Hanson, and A. C. Gossard, Phys. Rev. Lett. **92**, 226801 (2004).

[99] M. Sigrist, T. Ihn, K. Ensslin, D. Loss, M. Reinwald, and W. Wegschneider, Phys. Rev. Lett. **96**, 036804 (2006).

[100] B. R. Bulka, Phys. Rev. B **62**, 1186 (2000).

[101] C. Flindt, T. Novotny, and A.-P. Jauho, AIP Conf. Proc. **780**, 442 (2005).

[102] S. Sapmaz, P. Jarillo-Herrero, J. Kong, C. Dekker, L. P. Kouwenhoven, and H. S. J. van der Zant, Phys. Rev. B **71**, 153402 (2005).

[103] M. R. Wegewijs, *Electronic Transport in Quantum Dots*, Ph.D Thesis, Delft, Netherlands (2001).

List of Publications

Parts of this thesis have been previously published and presented on conferences as well as in invited talks. In particular the results of chapter 4.2 have been published in article #3 and chapter 4.3 in article #4. Results shown in chapter 5.3 are going to be published in the forthcoming article #5.

Articles:

1) A.-K. Klehe, V. Lauhkin, P. A. Goddard, J. A. Symington, J. Aghassi, J. Singleton, E. Coronado, J. R. Galan-Mascaros, C.J. Gomez-Garcia, C. Gimeney-Saiz, *Magnetorestistance studies of the ferromagnetic molecular metal* $(BEDT-TTF)_3$ $[MnCr(C_2O_4)_3]$ *under pressure*, Synthetic Metals **133**, 549, (2003)

2) *Stochastische Heizung in Particle in Cell Simulationen von Plasmagasentladungen* J. Aghassi, Diplomarbeit, RWTH Aachen, (2003).

3) J. Aghassi, A. Thielmann, M. H. Hettler, and G. Schön, *Strongly enhanced shot noise in chains of quantum dots*, Appl. Phys. Lett. **89**, 052101 (2006).

4) J. Aghassi, A. Thielmann, M. H. Hettler, and G. Schön, *Shot noise in transport through two coherent strongly coupled quantum dots*, Phys. Rev. B **73**, 195323 (2006).

5) J. Aghassi, M. H. Hettler, and G. Schön, *Tunneling transport in the co-tunneling assisted sequential tunneling regime*, in preparation (2007).

6) S. Haupt, J. Aghassi, M. H. Hettler, and G. Schön, *Cross-correlations in a double quantum dot in the co-tunneling regime*, in preparation (2007).

Conference Contributions:

J. Aghassi, A. Thielmann, M. H. Hettler, G. Schön, Sequential transport in molecules and quantum dots, WE-Heraeus Seminar on Molecules: Building Blocks for Future Nanoelectronics, Wittenberg, August 2004

J. Aghassi, A. Thielmann, M. H. Hettler, G. Schön, Shot noise in molecular nanostructures, RTN International workshop on Fundamentals of Nanoelectronics, Hamburg, September, 2004
Marie Curie Poster prize (2nd prize) for “best research presentation”

J. Aghassi, A. Thielmann, M. H. Hettler, G. Schön, Shot noise in tunneling transport through molecules and coupled quantum dots, DPG Frühjahrstagung Berlin, March 2005

J. Aghassi, A. Thielmann, M. H. Hettler, G. Schön, Tunneling transport through molecules and coupled quantum dots , ESONN 05, European School on Nanosciences and Nanotechnologies, Grenoble, France, August/September 2005

J. Aghassi, A. Thielmann, M. H. Hettler, G. Schön, Current and shot noise in chains of quantum dots, Marie Curie Conference on Spintronics, Poznan, Poland, September/October 2005

J. Aghassi, A. Thielmann, M. H. Hettler, G. Schön, Shot noise in tunneling transport through molecules and quantum dots, NTT-BRL School on Noise and Decoherence in Quantum Systems, Atsugi City, Japan, October/November 2005

J. Aghassi, M. H. Hettler, G. Schön, Non-local effects on transport in coupled quantum dots, DPG Frühjahrstagung Dresden, March 2006

J, Aghassi, M. H. Hettler, G. Schön, Tunneling transport in coupled quantum dot systems, WE-Heraeus Seminar on Quantum transport at the molecular scale, Bad Honnef, May 2006

J. Aghassi, M. H. Hettler, G. Schön, Tunneling transport through molecules and coupled quantum dots, IEEE EDS Workshop on Advanced Electron Devices, Essen/Duisburg, June 2006

J. Aghassi, M. H. Hettler, G. Schön, Co-tunneling effects in transport through interacting quantum dots, WE-Heraeus Seminar on Non-equilibrium Transport of Strongly Correlated Systems: Towards Simulation of Novel Devices, Bad Honnef, January/February 2007

Invited talks:

1) *Co-tunneling effects in transport through quantum dot systems*, Institut für Theoretische Physik A, RWTH Aachen, 19. November, 2006

2) *Noise in Nanostructures*, Lehrstuhl für Angewandte Physik, Universität Erlangen, 7. Mai, 2007